Technical Memorandum 104816

Evaluation of Two Computational Techniques of Calculating Multipath Using Global Positioning System Carrier Phase Measurements

Susan F. Gomez
Laura Hood
Robert J. Panneton
Penny E. Saunders
Antha Adkins
Dr. Shian U. Hwu
Ba P. Lu

April 1996

Technical Memorandum 104816

Evaluation of Two Computational Techniques of Calculating Multipath Using Global Positioning System Carrier Phase Measurements

Susan F. Gomez, Laura Hood, Robert J. Panneton, Penny E. Saunders
NASA/Lyndon B. Johnson Space Center

Antha Adkins, Dr. Shian U. Hwu, Ba P. Lu
Lockheed Martin Engineering & Science Services

March 1996

This publication is available from the NASA Center for AeroSpace Information,
800 Elkridge Landing Road, Linthicum Heights, MD 21090-2934, (301) 621-0390.

CONTENTS

CONTENTS
(continued)

TABLES

FIGURES

FIGURES
(continued)

FIGURES
(continued)

FIGURES
(concluded)

ACRONYMS

AMU	antenna measurement unit
CEM	computational electromagnetics
DECAT	dynamic environment communications analysis testbed
EIRP	effective isotropic radiated power
GANE	GPS attitude and navigation experiment
GPS	Global Positioning System
GTD	Geometrical Theory of Diffraction
ISS	International Space Station
JD	Julian Day
LHCP	left-hand circular polarized
RDP	radiation distribution pattern
RHCP	right-hand circular polarized
SNR	signal-to-noise ratio
SV	space vehicle
TANS	Trimble Advanced Navigation System
UT	Universal Time

1 Abstract

Two computational techniques are used to calculate differential phase errors on Global Positioning System (GPS) carrier wave phase measurements due to certain multipath producing objects: a rigorous computational electromagnetics technique called geometrical theory of diffraction (GTD) and a simple ray tracing method. The GTD technique has been successfully used to predict microwave propagation characteristics by taking into account the dominant multipath components due to reflections and diffractions from scattering structures. The ray tracing technique only solves for reflected signals. The results from the two techniques are compared to GPS differential carrier phase measurements taken on the ground using a GPS receiver in the presence of typical International Space Station (ISS) interference structures.

The calculations produced using the GTD code compared to the measured results better than the ray tracing technique. The agreement was good, demonstrating that the phase errors due to multipath can be modeled and characterized using the GTD technique and characterized to a lesser fidelity using the DECAT technique. However, some discrepancies were observed. Most of the discrepancies occurred at lower elevations and were either due to phase center deviations of the antenna, the background multipath environment, or the receiver itself. Selected measured and predicted differential carrier phase error results are presented and compared. Results indicate that reflections and diffractions caused by the multipath producers, located near the GPS antennas, can produce phase shifts of greater than 10 mm, and as high as 95 mm. It should be noted that the field test configuration was meant to simulate typical ISS structures, but the two environments are not identical. The GTD and DECAT techniques have been used to calculate phase errors due to multipath on the ISS configuration to quantify the expected attitude determination errors.

2 Background

The ISS is planning to use a GPS receiver to provide position, velocity, time reference, and to determine attitude. The ISS is composed of many microwave energy reflecting structures (e.g., various solar panels, thermal radiators, Russian science power platform [SPP] tower, communications antennas, video cameras, and many attached payloads). These large reflective objects create multipath, which is the major error source for attitude determination on the ISS. Two computational techniques have been used to calculate the phase errors on the ISS to quantify the expected attitude determination errors. The ISS phase error data produced using the two techniques are then used in analysis to quantify the attitude determination performance of the GPS receiver and the ISS's attitude determination filter. The ISS's attitude determination filter combines the attitude determination information output from the GPS receiver with the ring laser gyro information available from the Honeywell Rate Gyro Assembly. The phase error calculations produced using the two techniques must match in magnitude and frequency the actual ISS multipath environment to adequately analyze the performance of the GPS receiver and the ISS's attitude determination filter.

To evaluate the computational techniques used to model the ISS GPS multipath environment, a series of GPS multipath field tests that simulated the ISS's GPS multipath environment were performed using the NASA/Johnson Space Center (JSC) GPS and Antenna Laboratory test facilities. The purpose of these tests was to compare the differential phase error characterizations produced using the two computational codes—a GTD code and a dynamic environment communications analysis testbed (DECAT) code—to differential phase error data taken with a GPS receiver on the ground. The GTD is a rigorous computational electromagnetics technique that has been successfully used to predict microwave propagation characteristics by taking into account the dominant multipath components due to reflections and diffractions from scattering structures. The DECAT code has been used for visibility analyses and was modified to include a simple reflective technique for solving for differential phase errors due to multipath.

3 Field Test Data Collection

3.1 Test Setup

The data were collected on the Building 14 antenna range at NASA/JSC from Julian Day (JD) 045 to JD082 (February 14 - March 23, 1995) using two GPS receivers and two sets of 4 antennas. The test site was selected to be as far away as possible from unintentional multipath producers. For the data collected from JD045 to JD068, both a Trimble Advanced Navigation System (TANS) Vector and TANS Quadrex were used to collect data. For the data collected from JD072 to JD082, only the TANS Quadrex was used. The TANS Vector was pulled from the test to begin modifications for use on the GPS attitude and navigation experiment (GANE). For the test days when both receivers were used, the signal from the antennas was split and sent to both receivers. The only difference between the receivers is that the Vector has the software to compute an attitude, whereas the Quadrex outputs the measurements necessary to compute attitude, but does not compute an attitude internally. The TANS Vector is the predecessor of the Loral Tensor proposed for use on the ISS. The antennas were mounted to an optical table in a 2-foot-square planar configuration. The optical table used during this test is flat to within 3 millimeters over its 4-ft by 8-ft surface and had been leveled to within 30 arc seconds using a bubble level. The antennas were mounted directly to the table on 3.5-inch-tall aluminum mounts that screwed into the optical table. A 12-ft by 12-ft ground plane rested on the optical table and was flush with the antennas. The ground plane was constructed out of standard wood 2 by 4's with 3 sheets of aluminum sheeting screwed into the 2 by 4's. Holes were cut into the ground plane to accommodate the antennas. Each receiver was connected to a laptop computer that recorded the data from that receiver. Figure 3.1.1 shows the test setup.

Data were collected in approximately 24-hour periods, with no intentional multipath producer and with each of 5 intentional multipath producers introduced individually. The 5 multipath producers are listed in the following table.

Tables 3.1.2 and 3.1.3 describe the test setup for each day of testing. Figures 3.1.1 - 3.1.7 show what the test setup looked like for various days, and Appendix A contains drawings of the locations of the multipath producing object with respect to the antennas for each day of testing.

For JD045 to JD066, Trimble patch antennas were used. For JD067 to JD082, MicroPulse choke ring antennas were used. Choke ring antennas are baselined for ISS. Figure 3.1.6 shows what the patch antennas look like and Figure 3.1.7 shows the choke ring antennas.

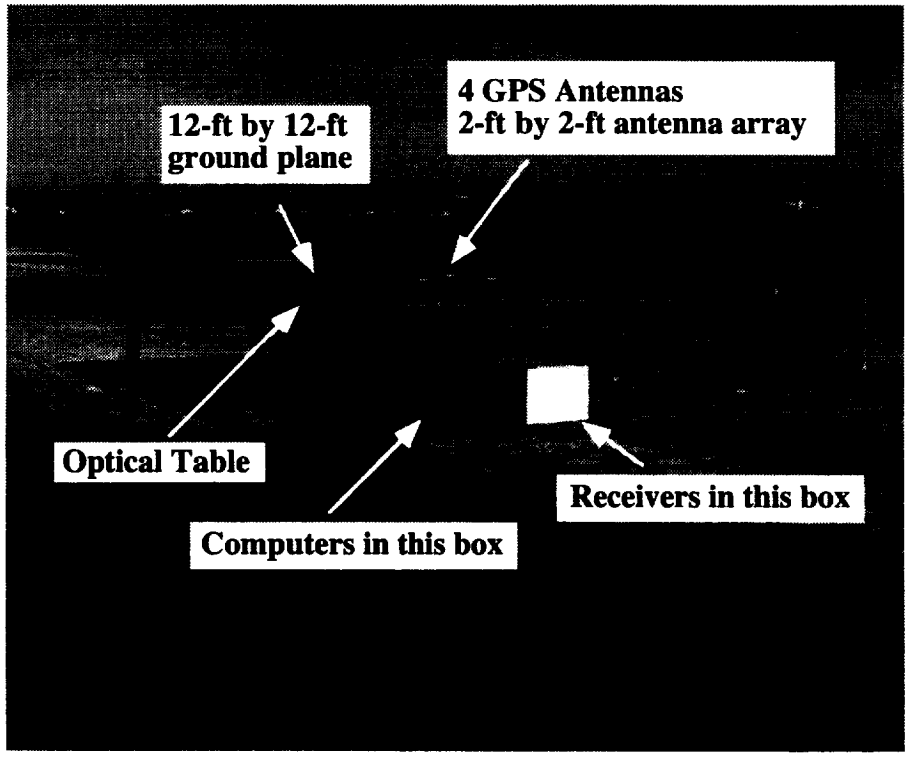

Figure 3.1.1 - Test setup with no multipath objects.

Table 3.1.1 - The 5 Multipath Producers

Name of Multipath Producer	Description of Multipath Producer
Aluminum Sheet	4-ft by 12-ft aluminum sheet at a 45° angle
3-ft diameter cylinder	3-ft diameter, 4 ft tall, polystyrene cylinder covered by aluminum foil
9-in. diameter cylinder	9-in. diameter, 4 ft tall, polystyrene cylinder covered by aluminum foil at a 45° angle
2.5-in. diameter cylinder	2.5-in. diameter, 5 in. tall, polystyrene cylinder covered by aluminum foil
box	28-in. by 15-in. by 40-in. polystyrene box covered by aluminum foil

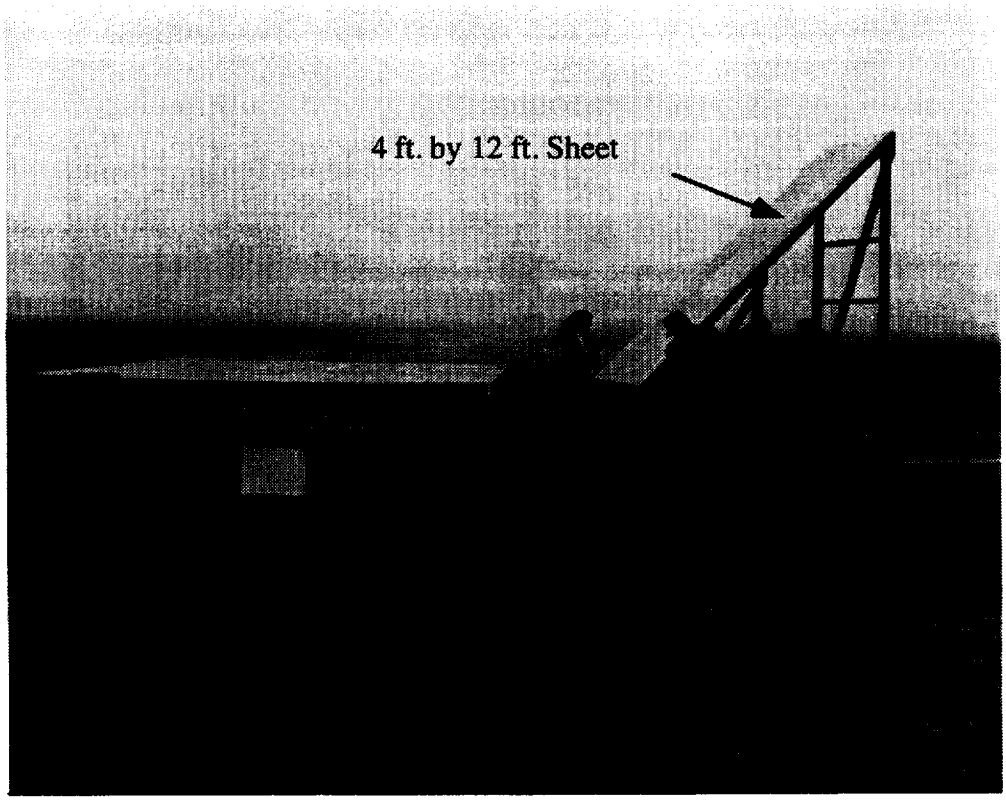

Figure 3.1.2 - Test setup with 4-ft by 12-ft aluminum sheet.

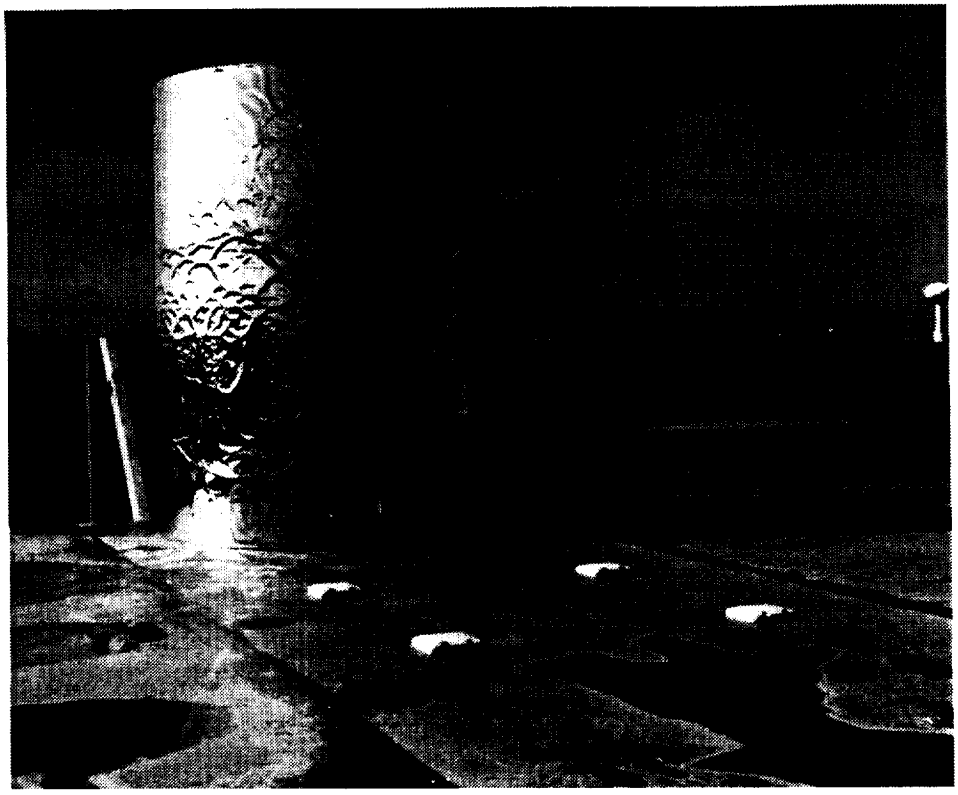

Figure 3.1.3 - Test setup with 3-ft-diameter cylinder.

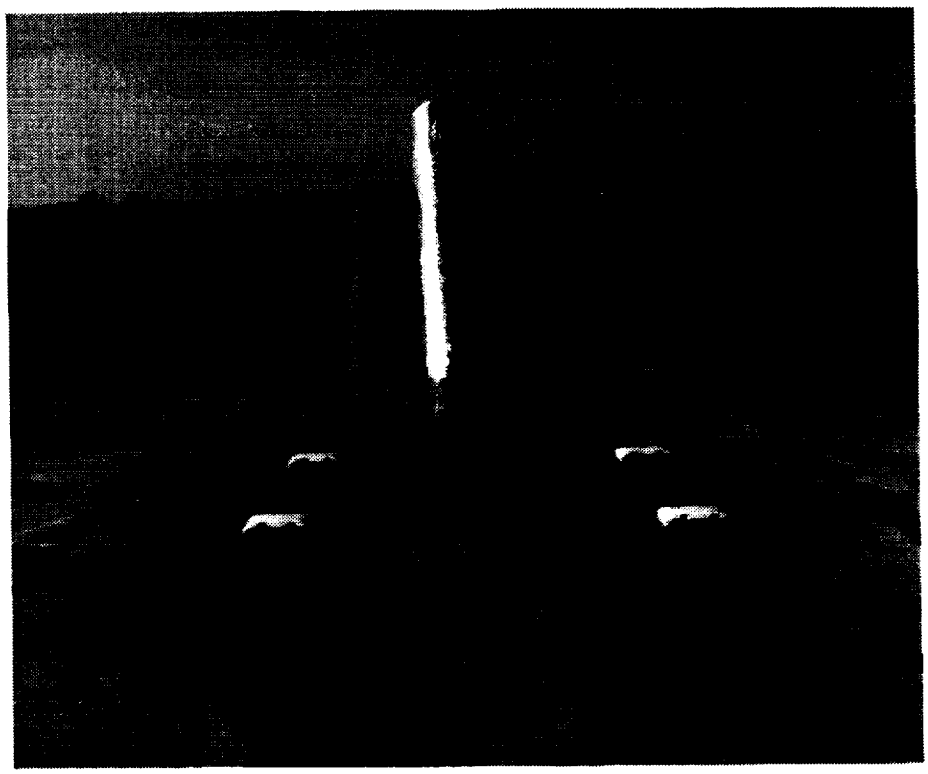

Figure 3.1.4 - Test setup with 9-in.-diameter cylinder.

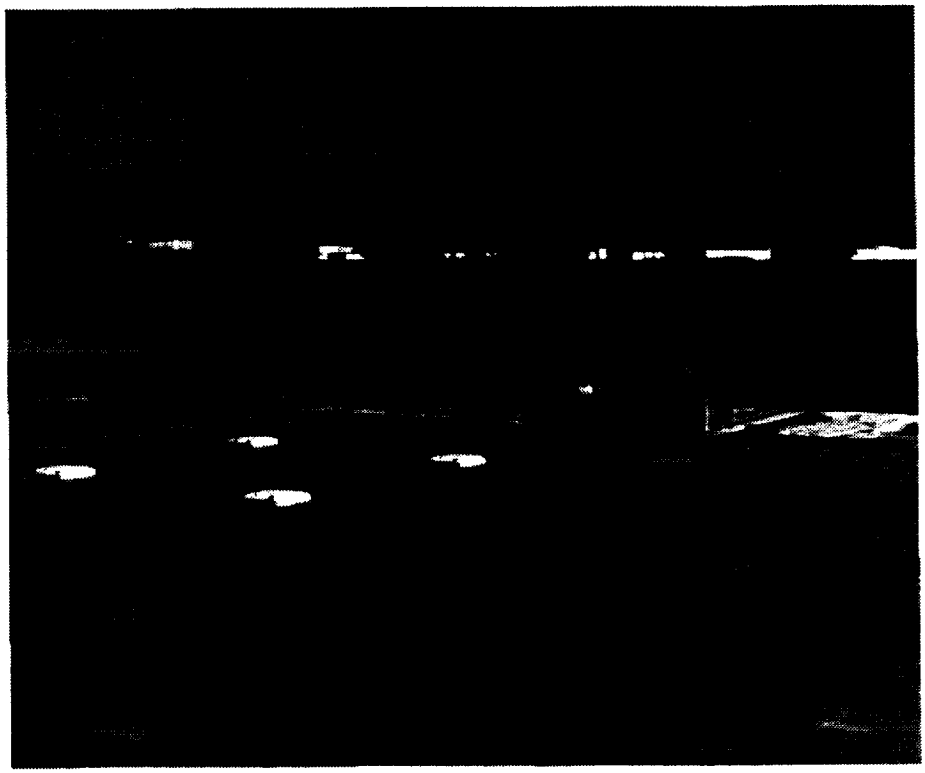

Figure 3.1.5 - Test setup with box.

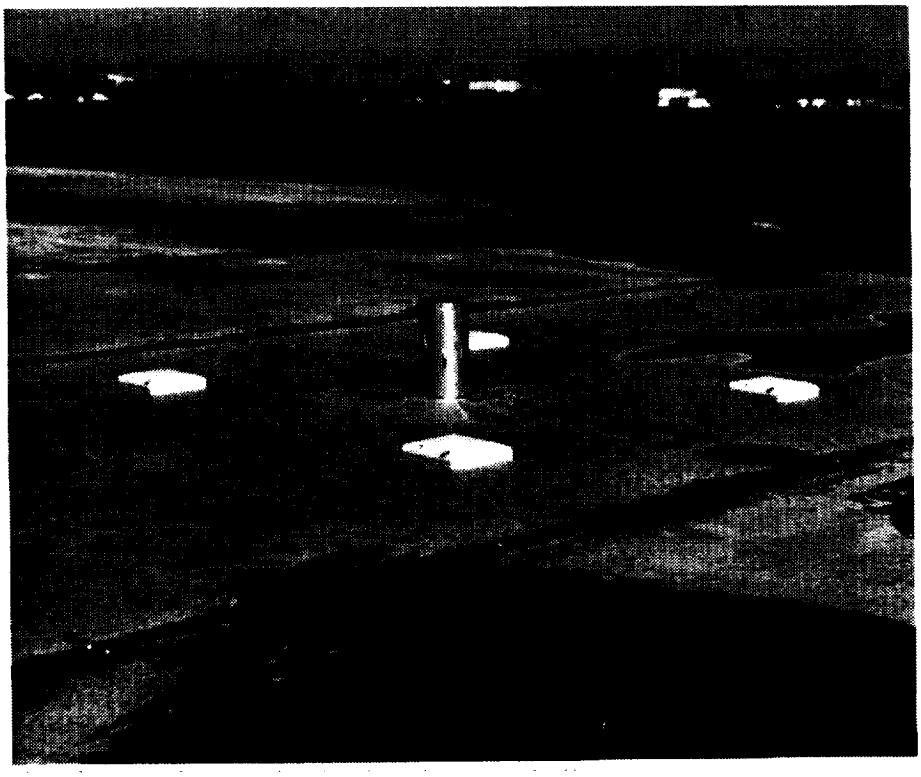

Figure 3.1.6 - Test setup with 2.5-in.-diameter cylinder.

Figure 3.1.7 - Test setup with MicroPulse choke ring antennas.

Table 3.1.2 - Data Collected Using Trimble Patch Antennas

Julian Day	Test Setup
JD045	4-ft by 12-ft Aluminum Sheet
JD046	no multipath producer
JD047	no multipath producer
JD048	no multipath producer
JD052	3 ft. diameter cylinder
JD053	9 in. diameter cylinder
JD054	box
JD058	box
JD059	4 ft. by 12 ft. Aluminum Sheet
JD060	3 ft. diameter cylinder
JD061	9 in. diameter cylinder
JD065	2.5 in diameter cylinder
JD066	no multipath producer

Table 3.1.3 - Data Collected Using MicroPulse Choke Ring Antennas

Julian Day	Test Setup
JD067	no multipath producer
JD068	no multipath producer
JD072	2 hours with no multipath producer (only TANS Quadrex running for rest of testing)
JD073	no multipath producer
JD074	3 ft. diameter cylinder
JD075	box
JD079	9 in. diameter cylinder
JD080	4-ft by 12-ft Aluminum Sheet
JD081	2.5 in diameter cylinder
JD082	no multipath producer

The weather and status of the GPS constellation were recorded each day of the test and given in Appendix C. The 2.5-in. cylinder did not contribute any differential phase errors that could be seen in the measured data.

3.2 Reference Attitude

The reference attitude was used to compute the theoretical differential phase, which was compared to the differential phase measured by the receivers. This section describes the method of calculating the reference attitude.

Since the antennas were mounted directly to the optical table using precisely manufactured mounts, the attitude of the table was the same as the attitude of the antennas. Therefore, the roll and pitch of the reference attitude was 0±30 arc seconds since the table had been leveled using a 30-arc-second-accurate bubble level. The yaw of the table was determined by sighting the North Star using a theodolite that had been collimated off an optical mirror mounted to the optical table. The mirror was mounted to the optical table along the Y axis of the table. Collimation occurs when a theodolite is perpendicular to the reflective surface. The theodolite has a white light in it, and when the light reflects off the mirror and the returning light interferes with the outgoing light, the phase of the light changes and the theodolite indicates that it is collimated by a green cross hair in the viewfinder. Therefore, with the theodolite collimated off the optical mirror, the azimuth and elevation of the North Star were measured in the table coordinate frame. The sightings to the North Star were reduced according to the method outlined in the following paragraphs to yield the reference attitude. The theodolite readings are listed in Appendix B. The reference attitude was calculated to be roll and pitch = 0± 30 arc seconds, yaw = -20.52° ± 40 arc seconds.

The method behind calculating the reference attitude is to determine three vectors in two coordinate systems, and therefore be able to calculate the transformation matrix from one coordinate system to the other, as in the following:

$$\begin{bmatrix} V_{1i}V_{2i}V_{3i} \\ V_{1j}V_{2j}V_{3j} \\ V_{1k}V_{2k}V_{3k} \end{bmatrix}_{WGS84} = M_{Table}^{WGS84} \begin{bmatrix} V_{1i}V_{2i}V_{3i} \\ V_{1j}V_{2j}V_{3j} \\ V_{1k}V_{2k}V_{3k} \end{bmatrix}_{Table}$$

M_{Table}^{WGS84} is the reference attitude. The table coordinate system is X up toward the zenith, Z from the master antenna toward antenna 3 in the plane defined by roll and pitch equal to zero, and Y completes the right-handed system. WGS84 is the World Geodetic System of 1984 in which the Z axis is the true celestial pole, the X axis is through the equator at the Greenwich meridian, and the Y axis is through the equator to form a right-hand coordinate system.

Three vectors need to be measured in the two coordinate frames. Two vectors, the zenith and a vector to a star, were calculated, and the cross product of the two calculated vectors is the third vector. The zenith vector in the table coordinate system was the X axis. The table X axis is

known to be perpendicular to the table Y and Z axes since the table was leveled. The zenith in WGS84 coordinates is calculated as:

$$zenith_X = \cos(latitude)*\cos(longitude)$$
$$zenith_Y = \cos(latitude)*\sin(longitude)$$
$$zenith_Z = \sin(latitude)$$

The longitude and latitude of the test location were surveyed previously and are given in Appendix B. The vector to the North Star was measured several times using a theodolite to measure the azimuth and elevation of the star in table coordinates. The theodolite was leveled using its internal leveling and auto-collimated off an optical mirror fixed along the table Z axis. Auto-collimation ensured that the theodolite was perpendicular to the reference bar. Azimuth and elevation readings were taken for different stars and the Universal Time (UT) recorded. To determine the vector to the star in WGS84 coordinates, the coordinates of the star in J2000 coordinates were obtained from a star catalog and transformed to WGS84 coordinates. The transformation matrix from J2000 to WGS84 was calculated using a standard subroutine (Ref. 1) and compensating for polar motion (Ref. 2). Six reference attitudes were calculated based on the five different star sightings. The greatest error between any two reference attitudes was 80 arc seconds.

3.3 Differential Phase Measurement Error Calculations

The differential phase error is the measured differential phase subtracted from the ideal differential phase. The measured differential phase is the differential phase measured by the receiver. The ideal differential phase was computed using the measured baselines and the reference or true attitude of the table as shown in the following:

$$\Delta\Phi_{ij_{ideal}} = u_j^T M_{B_{true}}^{WGS84} b_i^B$$

where:

u_j^T is the transpose of the unit vector from the receiver to satellite j

$M_{B_{true}}^{WGS84}$ is the matrix that transforms from the body frame to WGS84

b_i^B is the baseline vector in the body frame.

The line bias, β, equals the mean difference between the measured differential phase and the ideal differential phase:

$$\beta = \frac{1}{k}\sum_{t=1}^{k}(\Delta\Phi(t)_{ij_{measured}} - \Delta\Phi(t)_{ij_{ideal}})$$

where t is the measurement number and k is the total number of measurements.

The differential phase error contains errors due to noise and multipath and was computed as follows:

$$\Delta\Phi_{ij_{error}} = \Delta\Phi_{ij_{measured}} - \Delta\Phi_{ij_{ideal}} - \beta_j$$

3.4 Baseline Calculations

The baselines were computed by the Vector receiver during its "self survey" and were also computed mechanically. The baselines computed mechanically were computed from the center of each antenna using the following technique. Since the optical table contains mounting holes every 1 in. ± 0.001 in. over its entire surface, and the antennas were placed on mounts manufactured to within a tolerance of 0.001 in. so that the center of the antenna was directly over the center of the mounting screw that screwed into the optical table, the locations of the mechanical center of the antennas were determined by measuring the mounting holes on the table. The actual distance between each antenna would more accurately be measured from the phase centers of each antenna. The phase center of the antenna is the average position where the signal is received. The phase center moves around slightly depending on the azimuth and elevation of the incoming signal, but multipath can make the phase center appear to move more. Reference 3 describes a method of measuring the phase centers of antennas and has a measurement of the phase center of a Trimble patch antenna showing that the phase center is within 2 mm of the mechanical center of the antenna. NASA/JSC is also conducting tests to measure phase centers of the antennas being used on GANE and proposed for ISS. For the results in this paper, the mechanical locations of the center of the antennas are used to determine the baselines.

The Vector receiver outputs its calculations of the baselines in East, North, Up (ENU) coordinates. The mechanical locations of the baselines were measured in body, or table, coordinates and transformed to ENU coordinates using the reference attitude. Tables 3.4.1 and 3.4.2 compare the mechanically measured baselines to the Vector's self survey baselines. Notice that the greatest difference between the mechanically measured and self survey baselines is 3.72 mm.

Table 3.4.1 - Comparison Between Mechanically Measured and the Vector's Self Survey Baselines in meters

Baseline Component	Mechanical Baseline	Self Survey Baseline
Baseline 1 - East	-0.57284	-0.56924
Baseline 1 - North	0.20850	0.21012
Baseline 1 - Up	0.0000	0.000166
Baseline 2 - East	-0.36434	-0.36062
Baseline 2 - North	0.78133	0.78357
Baseline 2 - Up	0.0000	0.00084
Baseline 3 - East	0.20850	0.20946
Baseline 3 - North	0.57284	0.57210
Baseline 3 - Up	0.0000	-0.00012

Table 3.4.2 - Differences Between Mechanical and Self Survey Baselines in mm

Baseline Component	Difference
Baseline 1 - East	3.60
Baseline 1 - North	1.62
Baseline 1 - Up	0.166
Baseline 2 - East	3.72
Baseline 2 - North	2.24
Baseline 2 - Up	0.84
Baseline 3 - East	0.96
Baseline 3 - North	0.74
Baseline 3 - Up	0.12

3.5 Line Bias Calculations

A line bias would be more accurately described as a differential line bias, but it has become known as a line bias. The line bias is the offset that occurs in the differential phase measurements as a result of the different electrical pathlengths each of the phase measurements travels. For example, line bias 1 is the offset in the differential phase measurement between slave antenna 1 and the master antenna. Line bias 1 is due to the difference in the electrical path lengths between the master antenna and the receiver, and antenna 1 and the receiver. If all the electronics and cables stayed at the same temperature, then the line bias would remain constant. But, the changing temperatures of the components make the electrical pathlength change, changing the line bias from day to day.

Table 3.5.1 compares the line biases that the Vector receiver calculated during its self survey to line biases calculated using the recorded differential phase measurements. The post-processed line biases were calculated by taking the mean of the offset in the differential phase measurement error computed by subtracting the ideal differential phase from the measured differential phase, as described in Section 3.3. Notice that the post-processed calculated line biases are not exactly the same as the Vector's self survey calculated line biases.

Table 3.5.1 - Comparison of the Vector's Line Biases Determined During Self Survey and by Post-Processing in mm

Data Collected	Line Bias 1	Line Bias 2	Line Bias 3
Self Survey Calculated on JD044	42.22921	3.65769	23.34093
Post-Processed on JD044	46.03187	3.006294	23.78553
Difference	-3.80	0.63	-0.44

Table 3.5.2 compares the line biases for each day of testing when there were two receivers and the patch antennas and Table 3.5.3 compares the line biases for each day of testing when there was only the Quadrex receiver and the choke ring antennas. The difference in the line bias calculation on JD046 and JD047 is small compared to the largest difference for any two days, but this difference was enough to cause a mean error of 0.5° in the Vector's attitude solution. (Ref. 4 contains a thorough discussion of the errors than can result from changing line biases and an approach to eliminate the changing line biases effect on the attitude solution.)

Table 3.5.2 - Post-Processed Quadrex Line Biases for Portion of Testing With 2 Receivers in mm

Data Collected	Line Bias 1	Line Bias 2	Line Bias 3
Post-Processed on JD045	31.17691	-7.276297	85.733491
Post-Processed on JD046	23.50699	-9.64554	88.20693
Post-Processed on JD047	28.41184	-9.52945	87.09866
Post-Processed on JD048	33.26235	-6.58825	90.08356
Post-Processed on JD059	29.168097	-8.15043	87.54953
Post-Processed on JD066	33.01402	-4.9457	89.13926
Difference in JD046 and JD047	-4.90	-0.12	1.11
Largest Difference	9.75	4.70	4.35

Table 3.5.3 - Post-Processed Quadrex Line Biases for Portion of Testing With Only the Quadrex in mm

Data Collected	Line Bias 1	Line Bias 2	Line Bias 3
Post-Processed on JD073	48.04340	-30.75701	-30.64966
Post-Processed on JD074	48.36355	-31.17862	-30.91053
Post-Processed on JD075	49.49614	-30.05021	-29.77775
Post-Processed on JD079	48.18077	-27.06417	-27.05980
Post-Processed on JD080	48.41808	-27.06151	-27.24087
Post-Processed on JD082	48.13327	-26.21867	-27.17836
Largest Difference	1.45	4.95	3.59

3.6 Repeatability of Data on Multipath Free Days

To be able to determine what each multipath-producing object contributed to the differential phase error on the measured data, it is necessary to know what the differential phase errors are when no multipath-producing object is introduced to the test setup. Four days of measured differential carrier phase data with no multipath-producing object introduced were taken with the patch antennas, and another four days with the choke ring antennas. The four days of data taken with no multipath object using the patch antennas were JD046, JD047, JD048, and JD066. The four days of data taken with no multipath object using the choke ring antennas were JD067, JD068, JD073, and JD082. Figures 3.6.1 - 3.6.6 show what the differential phase error signature looked like for each of these days using satellites 5, 17, and 27.

Figures 3.6.1a - 3.6.1d show the differential phase error trace for satellite 5 on each of the four days with no multipath object introduced and using the patch antennas, which were days JD046, JD047, JD048, and JD066. The differential phase error is plotted against GPS time of week in hours between 98 and 102. The GPS times for days JD047, JD048, and JD066 were made to

correspond to GPS time for JD046. The differential phase error signature is fairly repeatable from day to day. Notice that there is a definite signature in each day's data, and the trace does not appear to simply be noise. The possible causes of the signatures are deviations of the phase center of the antenna, background multipath, or receiver introduced errors. The most likely cause of the signatures is felt to be phase center motion of the antenna. By modeling the surrounding structures, such as Building 14 and the antenna tower, in the GTD simulation, it was found that the surroundings did not contribute significant multipath. In anechoic chamber tests performed at JSC, it has been noted that the phase center of the antenna does shift appreciably depending on the azimuth and elevation of the incoming signal. Although the antennas were lined up facing the same direction - so that if the phase center deviation on each antenna was identical, then it would cancel out - it was found in the anechoic chamber tests that every antenna exhibits slightly different antenna phase center deviation that would explain the signatures.

Figures 3.6.2a - 3.6.2d show the differential phase error trace for each of the four days with no multipath object introduced and using the choke ring antennas for satellite 5, which were days JD067, JD068, JD073, and JD082. The differential phase error is plotted against GPS time of week in hours between 98 to 102. The GPS times for days JD067, JD068, JD073, and JD082 were made to correspond to GPS time for JD046. The differential phase error signature is fairly repeatable from day to day, but again notice that there is a definite signature in each day's data, and the trace does not appear to simply be noise. Notice that the signatures for the four days using the patch antennas are quite different than the signatures using the choke ring antennas. It is not clear looking at Figures 3.6.1 and 3.6.2 that the choke ring antenna is an improvement over the patch antenna. The results given in Section 7 when the multipath objects are introduced show the advantages of the choke ring antenna.

Figures 3.6.3a - 3.6.3d show the differential phase error trace for each of the four days with no multipath object introduced and using the patch antennas for satellite 17. Again, the differential carrier phase signature is repeatable and has a definite signature.

Figures 3.6.4a - 3.6.4d show the differential phase error trace for each of the four days with no multipath object introduced and using the choke ring antennas for satellite 17. Again, the differential carrier phase signature is repeatable and has a definite signature. Also note that the choke ring signatures look very different from the patch antenna signatures.

Figures 3.6.5a - 3.6.5d and 3.6.6a - 3.6.6d show similar results for satellite 27.

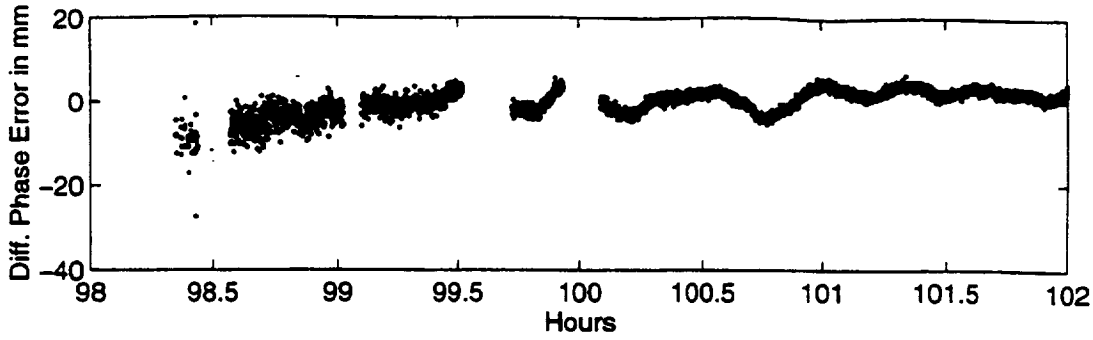

Figure 3.6.1a - Differential phase error for satellite 5 on JD046 with patch antennas.

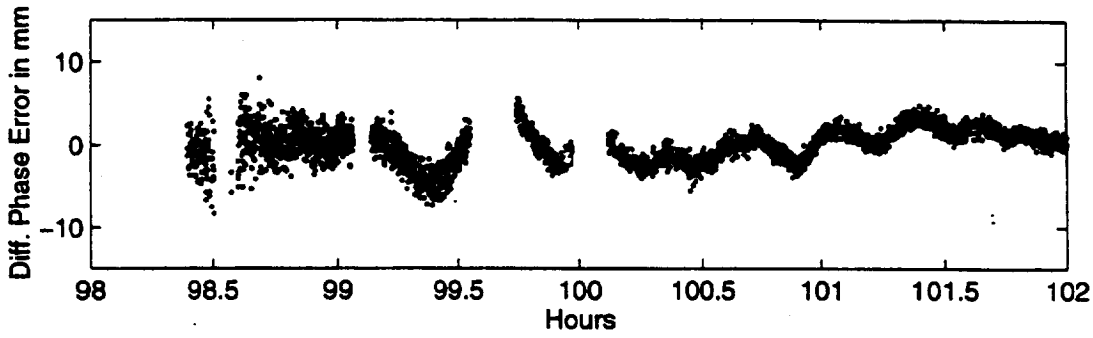

Figure 3.6.1b - Differential phase error for satellite 5 on JD047 with patch antennas.

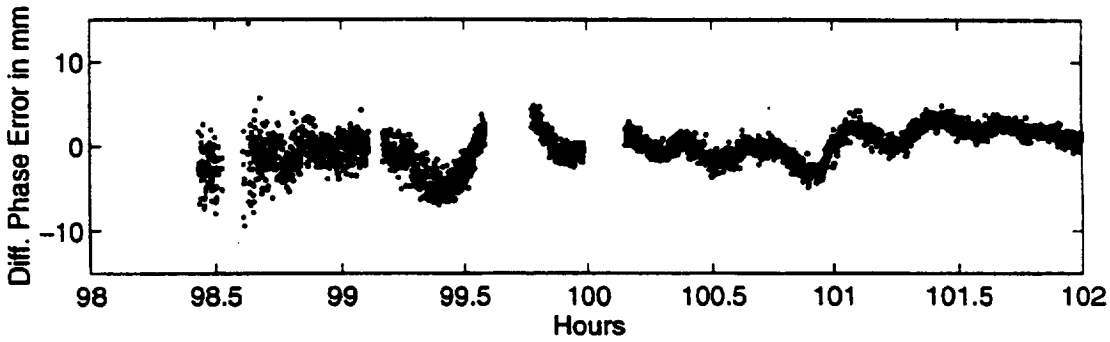

Figure 3.6.1c - Differential phase error for satellite 5 on JD048 with patch antennas.

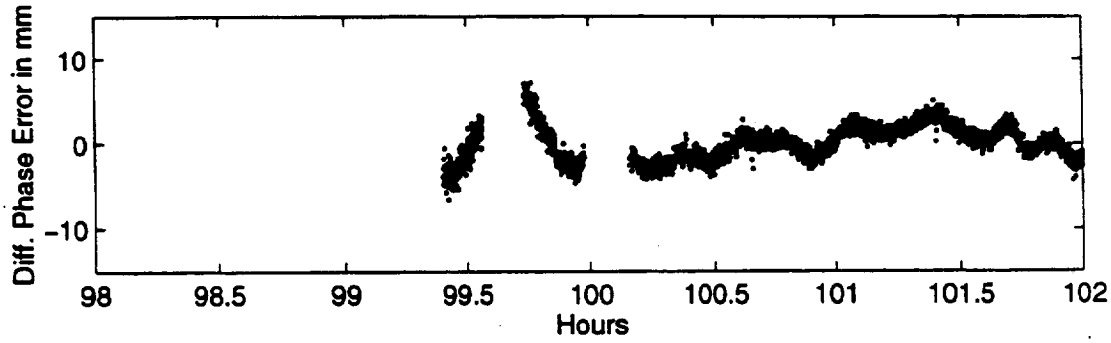

Figure 3.6.1d - Differential phase error for satellite 5 on JD066 with patch antennas.

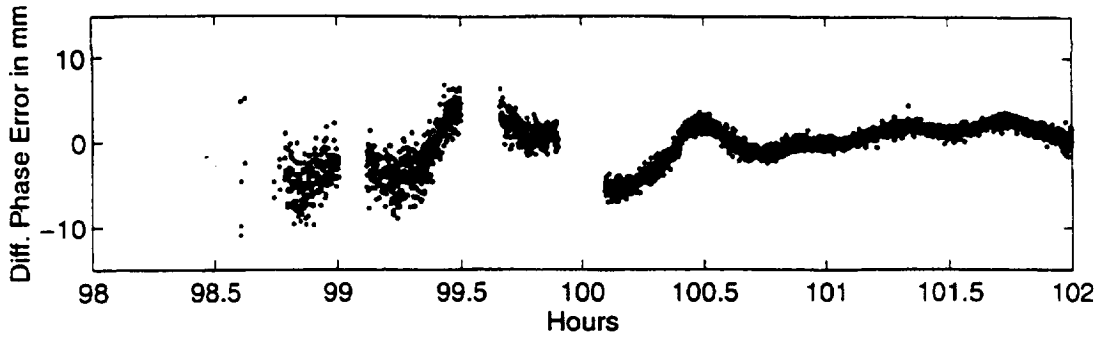

Figure 3.6.2a - Differential phase error for satellite 5 on JD067 with choke ring antennas.

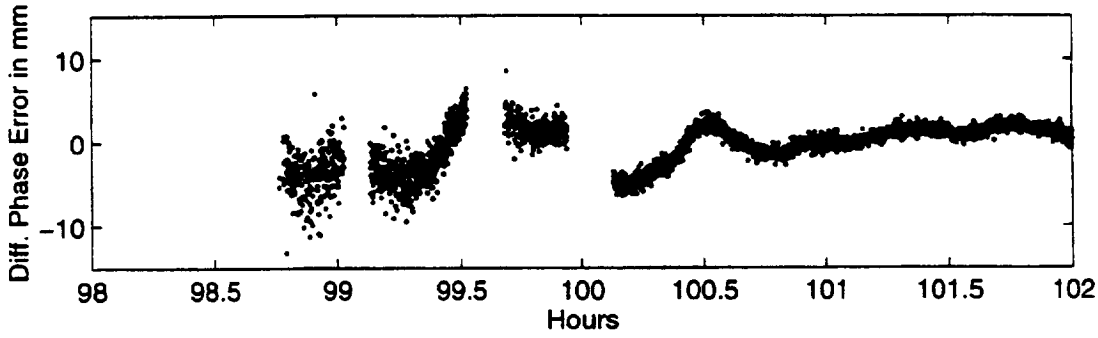

Figure 3.6.2b - Differential phase error for satellite 5 on JD068 with choke ring antennas.

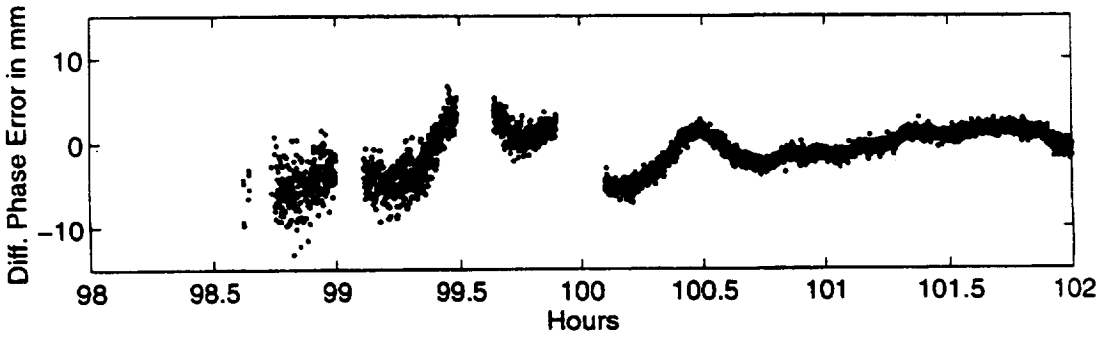

Figure 3.6.2c - Differential phase error for satellite 5 on JD073 with choke ring antennas.

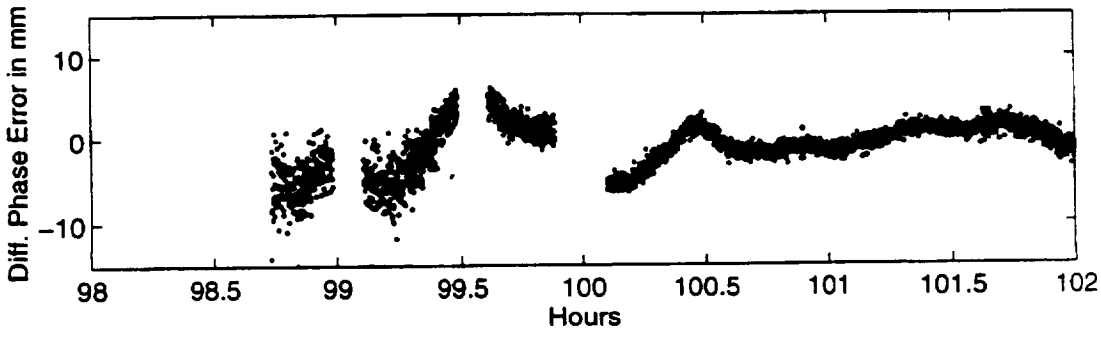

Figure 3.6.2d - Differential phase error for satellite 5 on JD082 with choke ring antennas.

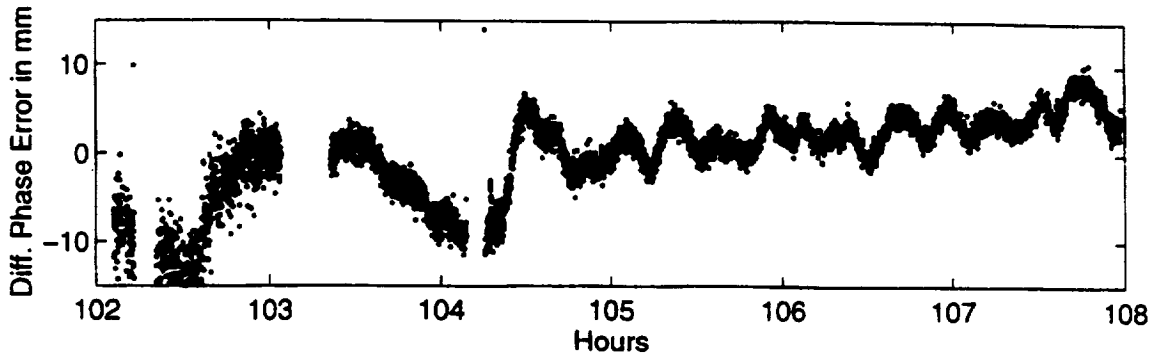

Figure 3.6.3a - Differential phase error for satellite 17 on JD046 with patch antennas.

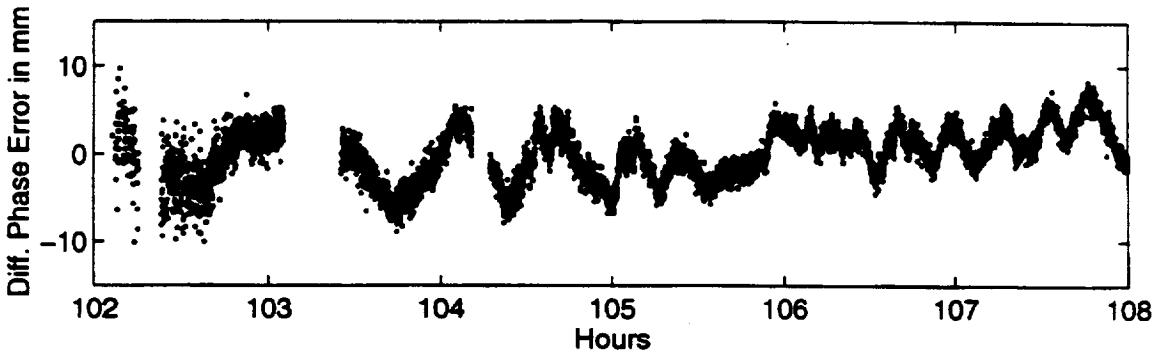

Figure 3.6.3b - Differential phase error for satellite 17 on JD047 with patch antennas.

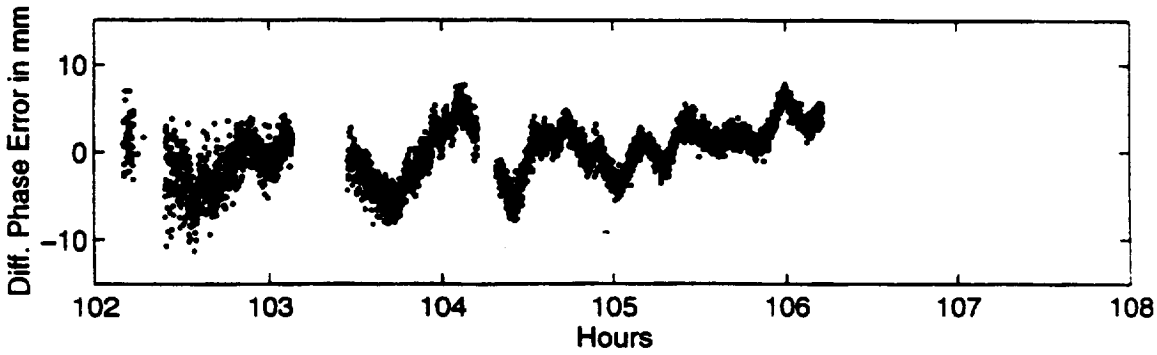

Figure 3.6.3c - Differential phase error for satellite 17 on JD048 with patch antennas.

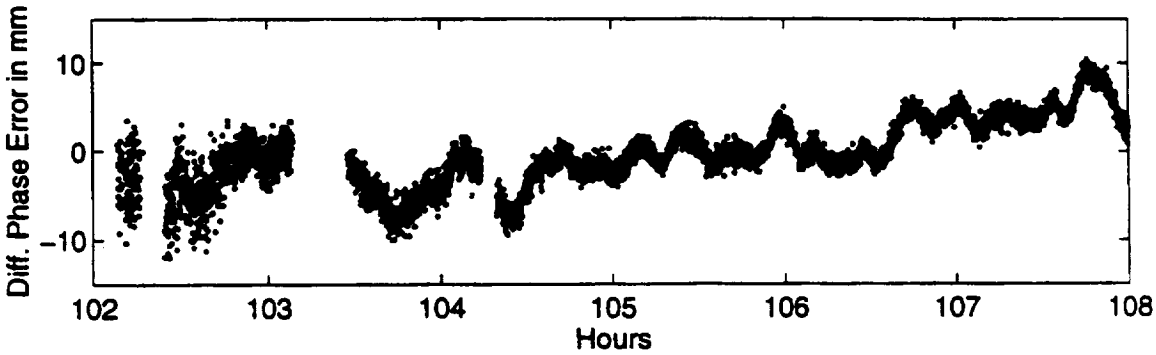

Figure 3.6.3d - Differential phase error for satellite 17 on JD066 with patch antennas.

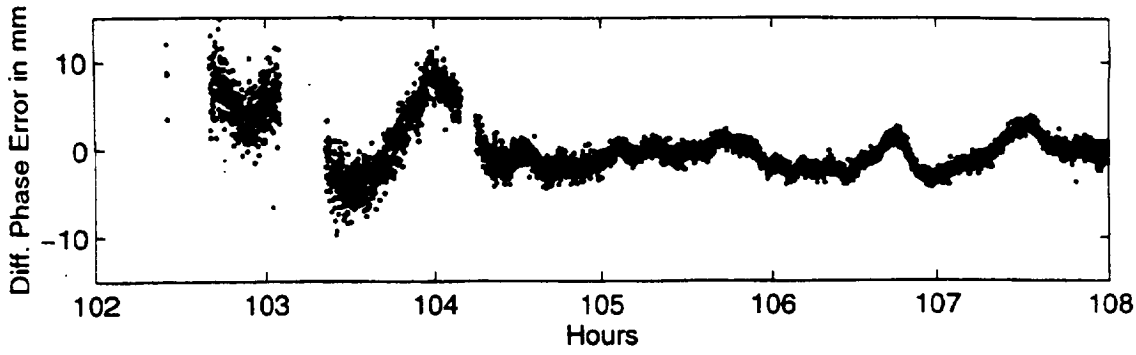

Figure 3.6.4a - Differential phase error for satellite 17 on JD067 with choke ring antennas.

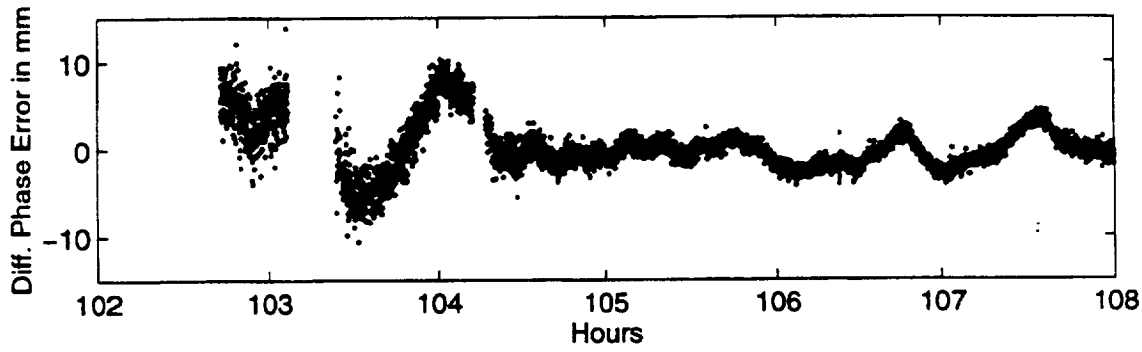

Figure 3.6.4b - Differential phase error for satellite 17 on JD068 with choke ring antennas.

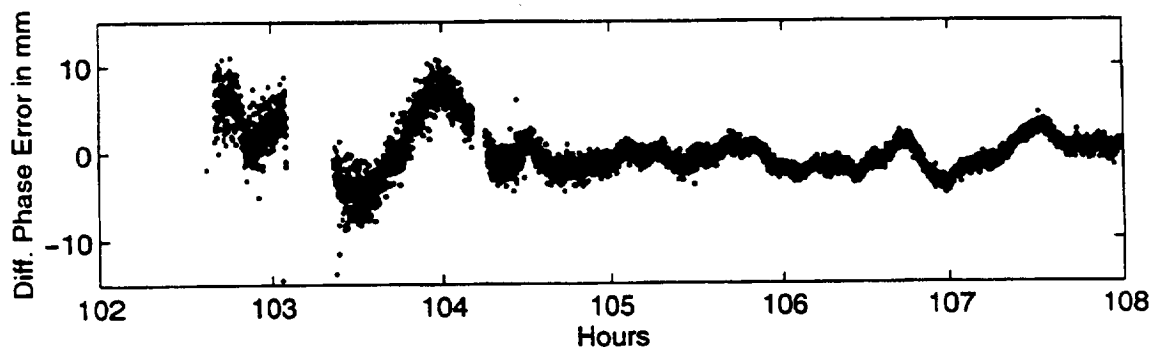

Figure 3.6.4c - Differential phase error for satellite 17 on JD073 with choke ring antennas.

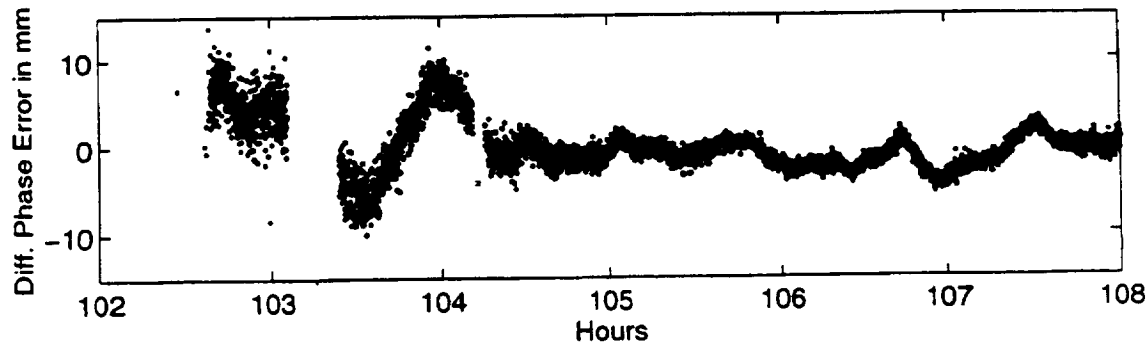

Figure 3.6.4d - Differential phase error for satellite 17 on JD082 with choke ring antennas.

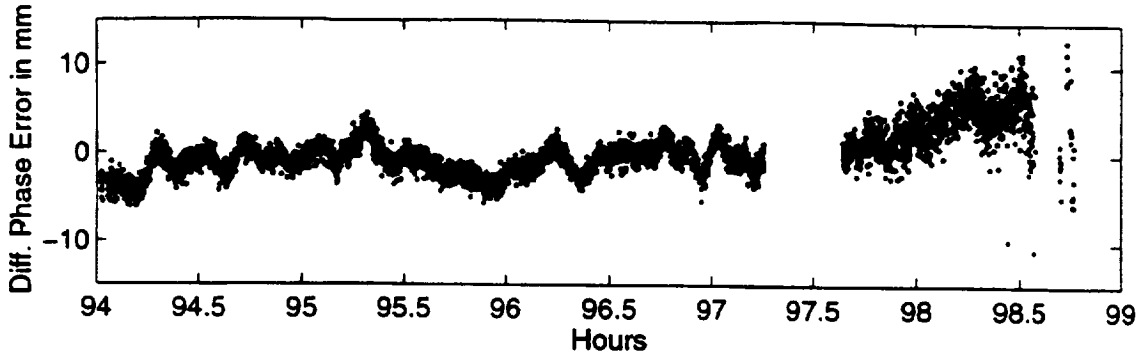

Figure 3.6.5a - Differential phase error for satellite 27 on JD046 with patch antennas.

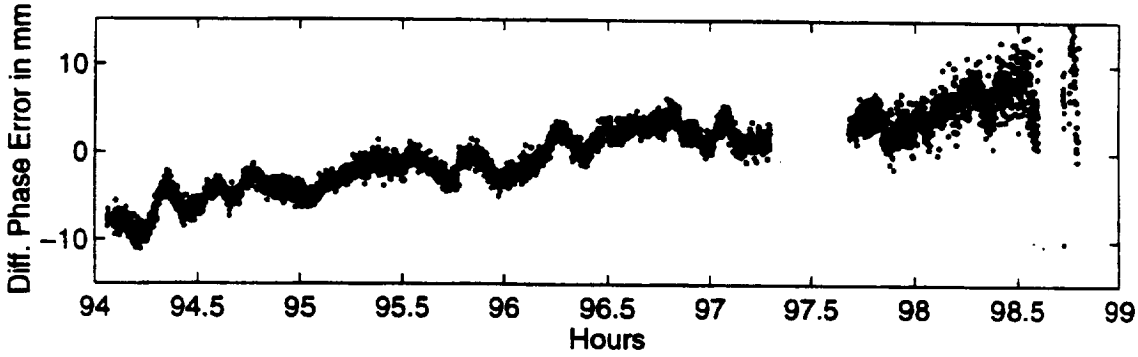

Figure 3.6.5b - Differential phase error for satellite 27 on JD047 with patch antennas.

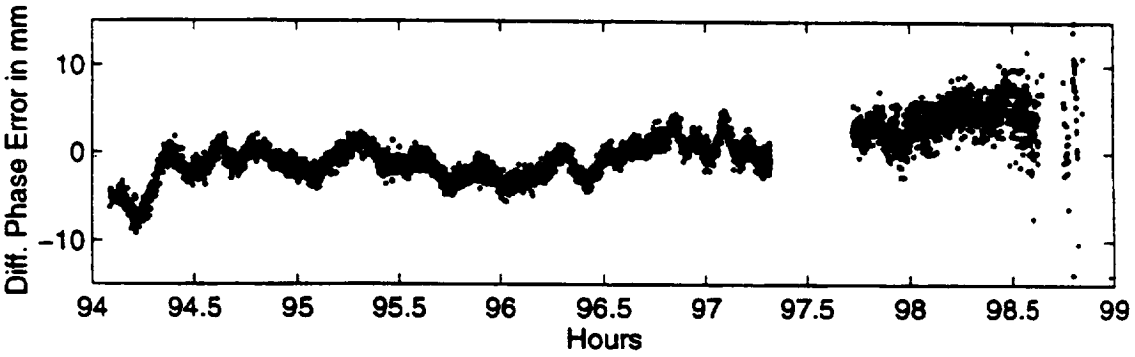

Figure 3.6.5c - Differential phase error for satellite 27 on JD048 with patch antennas.

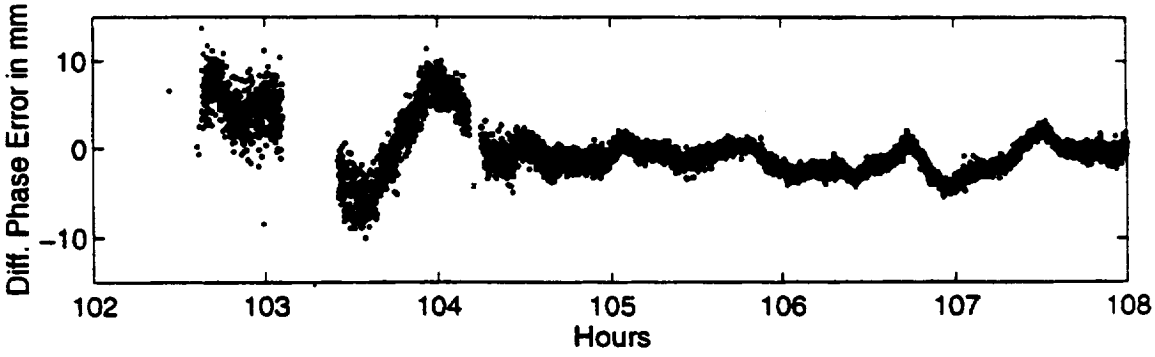

Figure 3.6.5d - Differential phase error for satellite 27 on JD066 with patch antennas.

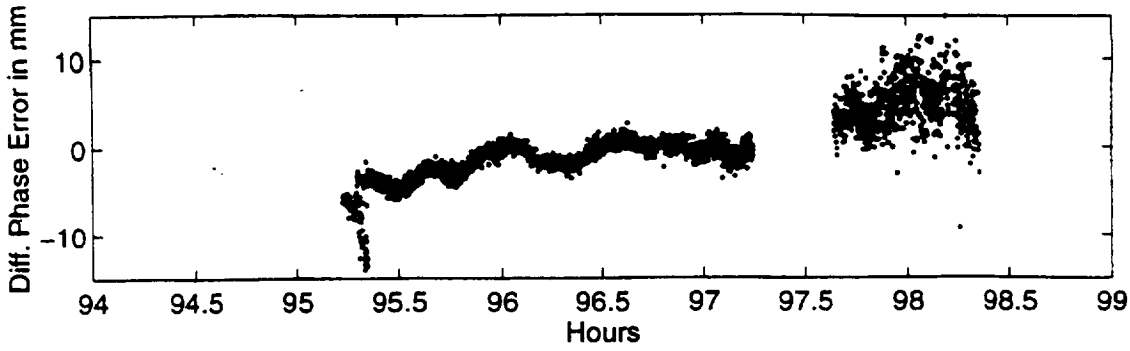

Figure 3.6.6a - Differential phase error for satellite 27 on JD046 with patch antennas.

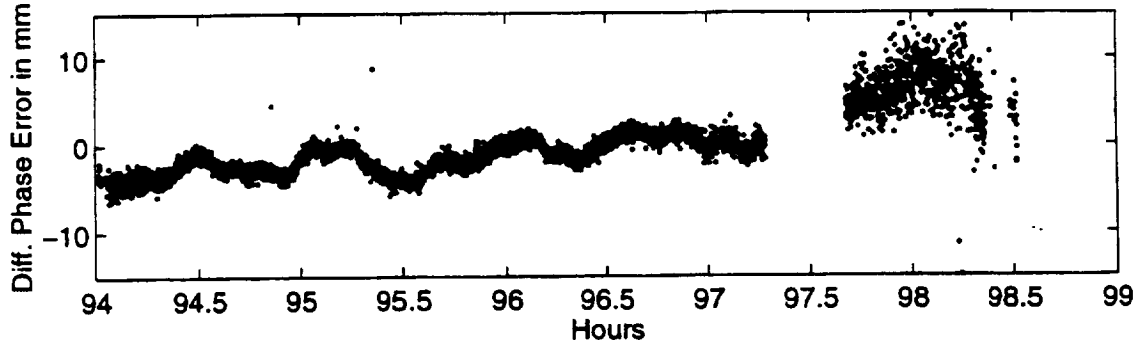

Figure 3.6.6b - Differential phase error for satellite 27 on JD047 with patch antennas.

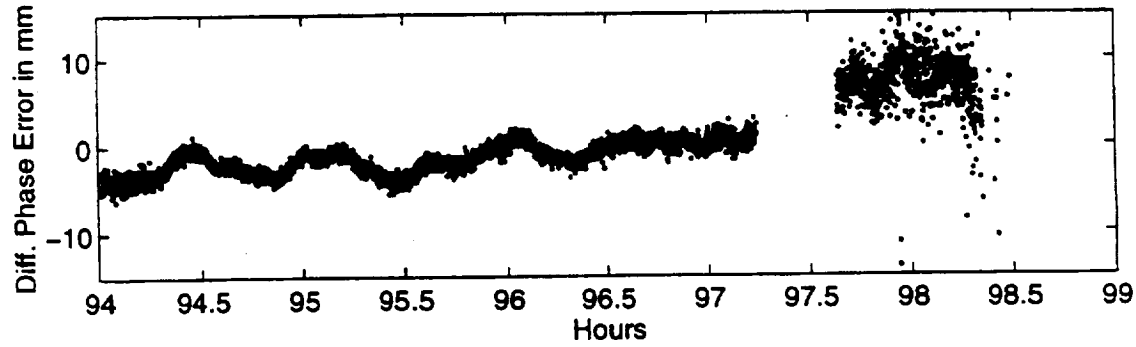

Figure 3.6.6c - Differential phase error for satellite 27 on JD048 with patch antennas.

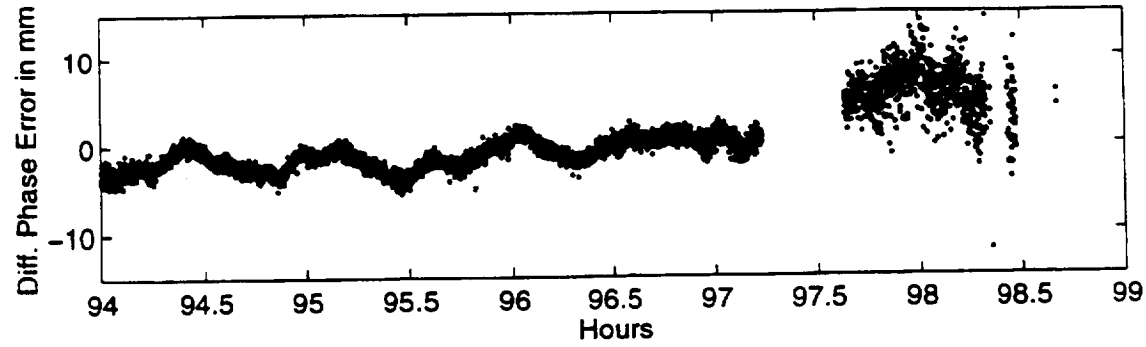

Figure 3.6.6d - Differential phase error for satellite 27 on JD066 with patch antennas.

4 Antenna Patterns

The antenna is an important element for the GPS subsystem. The GPS antenna receives and translates the GPS satellite signal into amplitude and phase information that is input to the GPS receiver. Therefore, GPS system performance is dependent on the antenna design and resulting antenna patterns.

Two different antenna types, Trimble microstrip patch antennas, shown in Figure 3.1.3, and MicroPulse choke ring antennas, shown in Figure 3.1.7, were used in this study. The patch antenna is smaller and provides a wider beamwidth, thus better hemispherical coverage. The choke ring antenna consists of several concentric metallic circular fins on a ground plane. The concept is similar to corrugations found on a corrugated horn antenna. The antenna radiating elements are located at the center of the ground plane. The purpose of the choke ring ground plane is to provide multipath rejection in the low elevation angles and thus better performance for a GPS system operated in a multipath environment. Therefore, the radiation pattern usually exhibits higher boresight and lower broadside gains and better axial ratio. The choke ring antenna is larger and weighs more than the simple microstrip patch antenna.

Since the GPS antenna is right-hand circular polarized, it is convenient to represent the antenna patterns in terms of right-hand circular polarized (RHCP) and left-hand circular polarized (LHCP) field components rather than the commonly used vertical and horizontal linear field components. The definitions of the GPS antenna patterns are shown below. The antenna patterns are represented graphically in Figures 4.1 and 4.2.

The electric field at any point in space for the GPS antenna patterns is defined by:

$$\mathbf{E} = \mathbf{r}E_r + \mathbf{l}E_l$$

where the direction unit vectors, $\mathbf{r}$ and $\mathbf{l}$, for the RHCP and LHCP fields are:

$$\mathbf{r} = \frac{1}{\sqrt{2}}(\theta - j\phi)$$

$$\mathbf{l} = \frac{1}{\sqrt{2}}(\theta + j\phi)$$

and the RHCP and LHCP field components, E_r and E_l are:

$$E_r = \frac{1}{\sqrt{2}}\left(E_\theta + jE_\phi\right)$$

$$E_l = \frac{1}{\sqrt{2}}\left(E_\theta - jE_\phi\right)$$

where E_θ and E_ϕ are the linear field components in the θ and ϕ directions defined in conventional spherical coordinates.

In this study, the GPS antennas were modeled as a point source with a combination RHCP pattern and an LHCP pattern that were obtained from the antenna patterns measured in JSC's

anechoic chamber. This simple model provides valid results only for multipath producers located in the far-field range of the GPS antenna. The far-field range R is determined by:

$$R = 2D^2 / \lambda$$

where D is the largest antenna dimension and λ is the wavelength. For omni-type low-gain GPS antennas, such as those used in the field tests, D is usually between 0.5λ and 1λ. For the worst case assumption $D=\lambda$, the far-field range $R=2\lambda$, which is about 0.4 meters for the GPS L1 frequency. The radiation pattern of this simple equivalent radiation source antenna model exhibits the same polarization sense and similar characteristics as the measured GPS antenna in both gain and phase, but only in the far field. If multipath producers are located in the near-field distance from the GPS antenna, a more complex antenna model is required to simulate the currents on the antenna to take into account the near field effects.

All GPS antennas are modeled as transmitting sources in this analysis. By reciprocity, the transmitting and the receiving patterns of an antenna are identical.

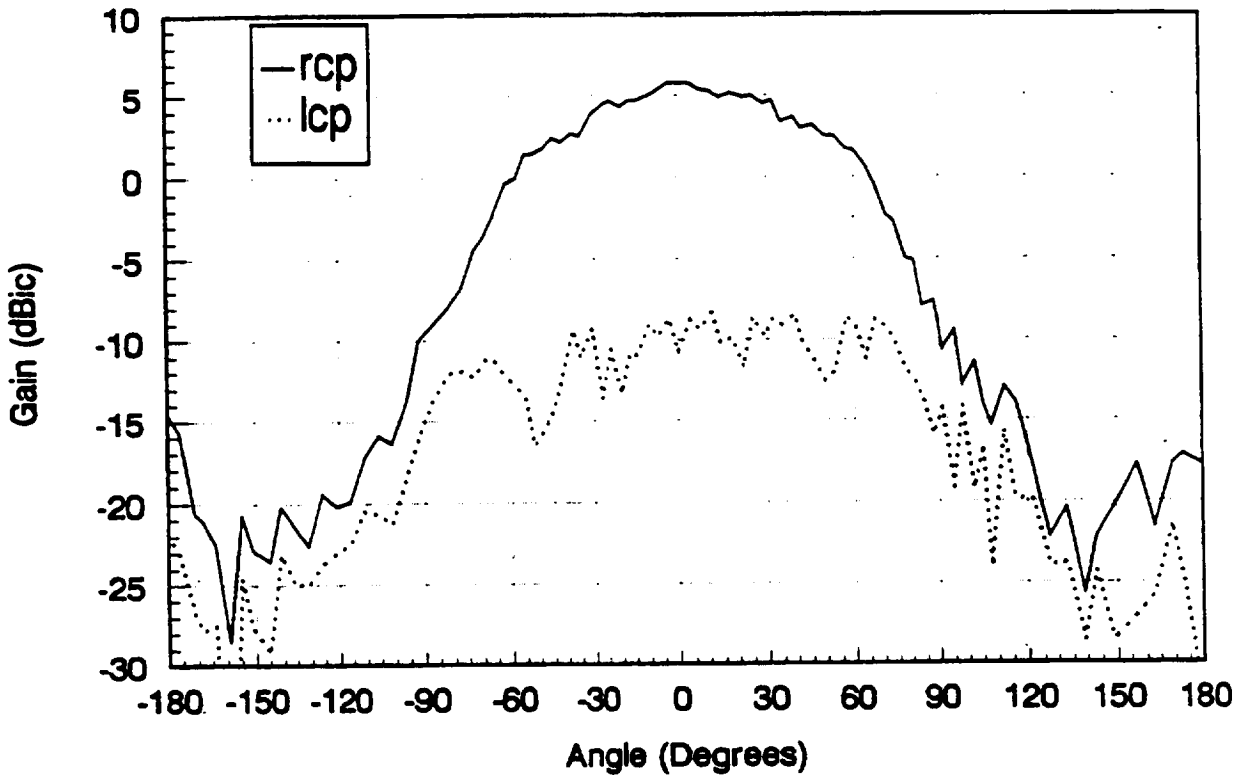

Figure 4.1 - GPS patch antenna pattern.

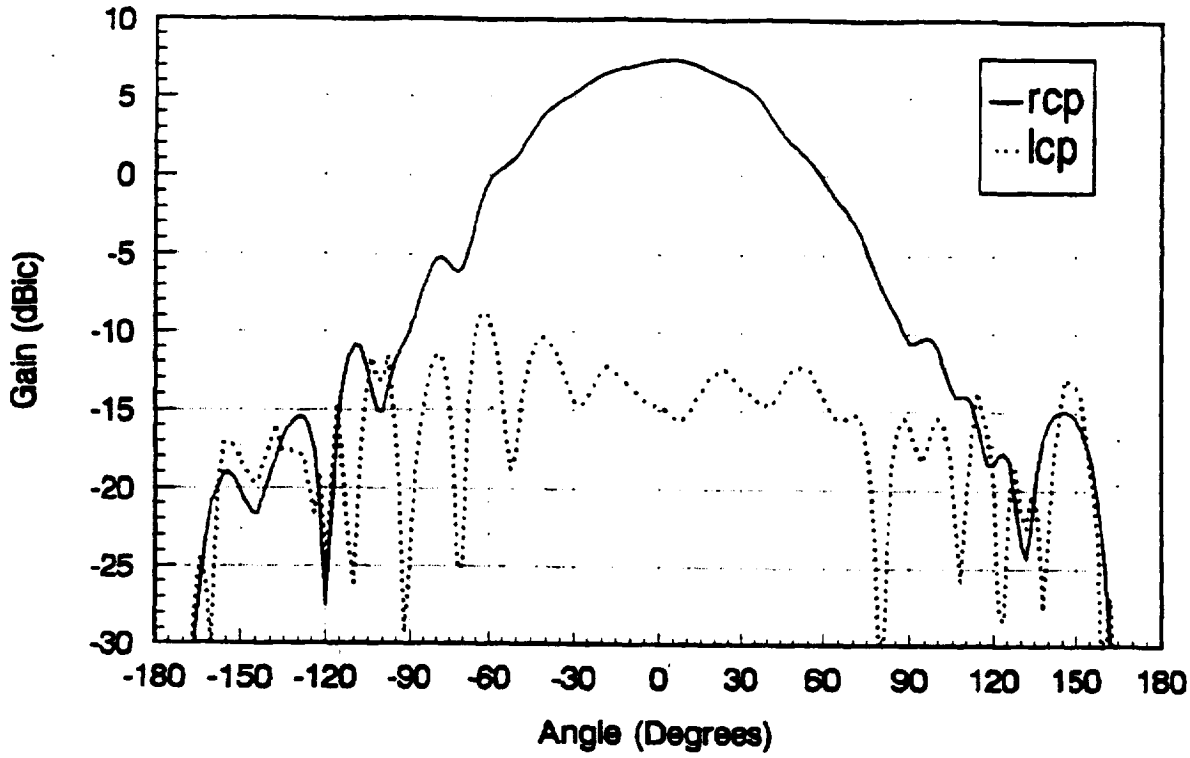

Figure 4.2 - GPS choke ring antenna pattern.

5 GTD Calculations

This section contains a very brief description of the geometrical theory of diffraction (GTD). It outlines a key equation and concept which provide the foundations for this work. The GTD is one of the most widely used computational electromagnetics (CEM) techniques. The reasons for this include the increased availability of low-cost but powerful computers, increasing interest in electromagnetic interactions with complicated geometry, and the simplicity of the method. The fundamentals of GTD can be understood more easily than other popular CEM techniques.

The GTD technique provides a high-frequency approximate solution to the electromagnetic fields including incident, reflected, and diffracted fields and their interactions. The fields are obtained from an asymptotic solution of Maxwell's equations and correspond to the leading terms of the asymptotic expansion for large values of wavenumber or frequency. In the field computation using GTD, the incident, reflected, and diffracted fields are determined by the field incident on the reflection or diffraction point multiplied by a dyadic reflection or diffraction coefficient, a spreading factor, and a phase term. The reflected and diffracted field at a field point r, $\mathbf{E}^{r,d}(r)$, in general have the following form:

$$\mathbf{E}^{r,d}(r) = \mathbf{E}^{i}(r)\mathbf{D}^{r,d}\mathbf{A}^{r,d}(s)e^{-jks}$$

where

$\mathbf{E}^{i}(r)$ is the field incident on the reflection or diffraction point r

$\mathbf{D}^{r,d}$ is a dyadic reflection or diffraction coefficient

$\mathbf{A}^{r,d}$ is a spreading factor

s is the distance from the reflection or diffraction point r to the field point r.

$\mathbf{D}^{r,d}$ and $\mathbf{A}^{r,d}$ can be found from the geometry of the structure at the reflection or diffraction point r and the properties of the incident wave at that point.

The application of GTD to a given radiation problem requires first decomposing the scattering structure into simple geometrical shapes, and knowing the reflection and diffraction coefficients for these geometrical shapes. Next, all field components contributing to the radiation intensity in the field point must be traced, and the individual contributions must be determined. The resultant field is given by summing all the complex contributing components:

$$\mathbf{E}^{tot} = \mathbf{E}^{inc} + \sum_{n=1}^{N}\mathbf{E}_{n}^{ref} + \sum_{m=1}^{M}\mathbf{E}_{m}^{dif}$$

where

$\mathbf{E}^{tot}$ is the total field at the observation point
$\mathbf{E}^{inc}$ is the direct incident fields from the antennas
$\mathbf{E}^{ref}$ is the reflected fields from the plates and cylinders
$\mathbf{E}^{dif}$ are the diffracted fields from plates and cylinders.

More detailed information about GTD and the specific GTD code used in this study can be found in Reference 5.

6 DECAT Calculations

6.1 DECAT Description

The DECAT is a computer simulation tool that models the dynamic motion of planets and vehicles, models the communication equipment on board those vehicles, and calculates communications parameters of interest. The number and setup of the vehicles, the communications equipment on the vehicles, and the parameters to calculate are user-determined for each simulation. DECAT is mostly used as a time-domain simulator, that, at each time step, determines the new positions of the dynamic elements and performs the desired calculations.

A DECAT simulation contains a user-defined number of vehicles. Each vehicle in a DECAT simulation is modeled with its motion, structure, and communications equipment. Each vehicle model must include a description of the vehicle's motion. This motion may be defined relative to the motion of a planet or another vehicle in the simulation. Motion models include models for orbiting vehicles and ground stations. Each vehicle model may include a structure model to model the physical body of the vehicle. The structures may be divided into segments, which consist of polygons. The segments in the structure may be assigned a motion, such as tracking or anti-tracking the sun. Each vehicle model may also include communications equipment models of any on-board transmitters, receivers, and antennas. The transmitters and receivers are modeled by the gains and losses that they contribute to the communications link. The antennas are modeled by their gain pattern and their boresight motion. The antenna gain pattern may be an ideal pattern or a measured pattern, and it may be a cut of a pattern or a full radiation distribution pattern (RDP).

A DECAT simulation may call a user-defined set of functions to calculate the communications parameters of interest. These parameters include whether a communication link is blocked by the structure on a vehicle, what the received signal-to-noise ratio (SNR) is at a receiver, and the number of equal-angle multipath signals received.

6.2 DECAT Multipath Calculations

The DECAT multipath function determines all the non-blocked, single-reflection, equal-angle (specular) multipath paths between a transmitter and a receiver given the transmitting and receiving antenna locations and the structure near the receiving antenna. The algorithm works as follows (Ref. 6). First, the function determines if the direct path is blocked by the Earth. If Earth blockage occurs, no other calculations are performed. If the direct path is not blocked by the Earth, the function determines if the direct path is blocked by the structure. Then, for each polygon of each segment in the structure, the function determines if that polygon causes multipath. If it causes multipath, the function determines if the path from the transmitter to the reflecting polygon is

blocked or if the path from the reflecting polygon to the receiver is blocked. If neither path is blocked, a specular reflection occurs and its path length and associated antenna gain are recorded. Since a circularly polarized signal's polarization reverses when it reflects off a perfectly conducting structure, the multipath signals are oppositely polarized from the direct signals. Therefore, the function uses one antenna pattern for the direct path gain and another antenna pattern (cross-polarized from the first) for the indirect path gains. The function reports if the direct link was blocked by the Earth or structure, the number of paths from the transmitting antenna to the receiving antenna, the path length for each path, and the antenna gain for each path.

The data is post-processed to determine the composite phase at each antenna, the differential phase at each slave antenna, and the phase error at each slave antenna. The composite phase at each antenna is determined by phasor-summing together the signals from all the paths to the antenna. Although a signal will experience a loss when it reflects off a structure, the reflection loss was assumed to be 0 dB, which is the reflection loss for a perfect conductor and which will give the worst case (strongest) multipath signals. The differential phase, the phase at each slave antenna relative to the master antenna, is determined using the following equation:

$$differential\_phase(i) = slave\_phase(i) - master\_phase$$

where i is the slave antenna number.

The composite phase at each antenna and differential phase at each slave antenna are determined both for an ideal case, which does not include the structural effects of blockage and multipath, and for the actual case, which includes the effects of blockage and multipath. The phase error for each slave antenna is determined using the following equation:

$$phase\_error(i) = actual\_differential\_phase(i) - ideal\_differential\_phase(i)$$

where i is the slave antenna number.

Since the DECAT models only the direct signal and the specularly reflected multipath signals, some regions are modeled better than others. DECAT is expected to perform well in regions where the direct signals or the reflected signals are the dominant components, but it is not expected to perform well in regions where diffraction or scattering are dominant components. Furthermore, since DECAT uses polygons to model the structure, it is expected to perform well for structures which can be accurately modeled by polygons, such as plates and boxes, and not as well for structures which can only be approximated by polygons, such as cylinders.

6.3 DECAT Simulation Setup

Specific GPS space vehicle (SV) tracks for specific test days were chosen for simulation. A DECAT simulation was run for each of the chosen SV tracks and days. Each simulation included a

model for the test setup for the day chosen and a model of the GPS SV chosen. Each simulation used the multipath function and the SNR calculation function.

The GPS SVs were modeled by their motion and their communications equipment. The motion was modeled using an ideal elliptical orbit using the classical orbital parameters as input. The orbital parameters were taken from the YUMA almanac for the start of the week for each day being simulated. The ideal elliptical orbit model, although simple, produced azimuths and elevations which were very close to those measured at the test setup. Each GPS SV model includes a 0 dB gain omni-directional antenna and a transmitter whose output power is set to the calculated GPS effective isotropic radiated power (EIRP) of 27 dBW.

The test setup was modeled with its position, structure, and communications equipment. The test setup was placed at the position indicated in Table 6.3.1, which is the position of the Building 14 antenna range survey marker plus the height of the ground plane. The structure was rotated 20.52° to model the offset from North.

Table 6.3.1 - Position of Test Setup

Latitude (degrees)	29.558320
Longitude (degrees)	264.902175
Altitude (meters)	5.5445

The test structure for each date was modeled using polygons. The plates were modeled using a single polygon for the reflecting face, and the box was modeled with 6 polygons, one for each face. The cylinders were modeled with 10 polygons, 2 for the ends and 8 for the cylinder sides. For a few large cylinder cases, the cylinders were also modeled using 122 polygons, 2 for the ends and 120 for the cylinder sides. The polygon models of the reflecting plates and box are expected to produce results similar to the measured data, since plates and boxes can be accurately modeled using only polygons. However, the polygon models of the two cylinders are not expected to perform as well, since an N-sided cylinder model does not accurately model a cylinder.

The test setup communications equipment consisted of four antennas, one master and three slaves, and a receiver. The antennas were placed in the field test locations, and their boresites were pointed up. The patch antennas on JD045 and JD059 were modeled using cuts of antenna patterns, as shown in Figure 4.1. The choke ring antennas used on JD074, JD075, JD079, and JD080 were modeled using MicroPulse L1/L2 choke ring antenna patterns measured in the JSC anechoic chamber and shown in Figure 4.2. The choke ring antennas were placed an additional 3.38 in. (0.085852 m) above the ground plane to account for the additional height of the choke rings. The receiver parameters were not relevant to the results of these simulations.

7 Comparison of Field Data, GTD Data, and DECAT Data

7.1 Comparison of Field Data, GTD Data, and DECAT Data for JD045 With 4-ft by 12-ft Aluminum Sheet and Patch Antennas

For JD045, the 4-ft by 12-ft aluminum sheet was placed on the North side of the table as shown in Figure 3.1.2. The satellite tracks for JD045 are shown in Figure 7.1.1. Notice that there is no blockage of any of the satellites for this day. The diffraction region exists predominantly below 61° and the reflection region exists above 61°.

Figure 7.1.2 shows the comparison between the field data, GTD data, and DECAT data for satellite 4. Satellite 4 is predominantly in the reflection region and the differential phase errors are easy to see and have a distinct frequency characteristic. The upper plot in Figure 7.1.2 compares the measured differential phase errors to the GTD and DECAT calculated differential phase errors. The lower plot in Figure 7.1.2 shows the measured differential phase errors for a day with no intentional multipath producer. Remember that the differential phase errors for the measured data are calculated by subtracting the receiver's measured phase from the true phase. Therefore, the top plot in Figure 7.1.1 contains any background differential phase error signatures. The lower plot in Figure 7.1.1 shows what that background signature looked like on a day when no intentional multipath producer was present. By visually inspecting the upper and lower plots of the measured differential phase errors, the reader can notice any differential phase errors that are due to the flat plate. The authors tried to subtract the two measured signals, but it was more difficult to see the multipath trace in the resulting noisy signal than by visually inspecting the two traces. Both DECAT and GTD match the field test data well. Notice that for satellite 4, the background signature is very stable since the satellite is at high elevations.

Figure 7.1.3 shows the comparison data for satellite 14. Satellite 14 was entirely in the diffraction region; therefore, DECAT calculated all zeroes for satellite 14 since it only solves for reflected signals. The differential phase errors caused by the flat plat are difficult to ascertain by looking at the measured data, and the GTD calculated errors are small.

Figure 7.1.4 shows the comparison data for satellite 17. Satellite 17 transitions from the diffraction region, to the reflection region, and back to the diffraction region. Again, it is difficult to see any differential phase errors in the measured data in the diffraction region. However, the reflection region produces significant differential phase errors, and both DECAT and GTD calculate similar differential phase errors. Notice that satellite 17 has a noticeable differential phase error signature when no intentional multipath producer is present.

Figure 7.1.5 shows the comparison data for satellite 19. Satellite 19 transitions from the diffraction region, to the reflection region, and back to the diffraction region and has a similar ground track to satellite 17. Again, it is difficult to see any differential phase errors in the measured data in the diffraction region. However, the reflection region produces significant differential phase errors, and both DECAT and GTD calculate similar differential phase errors. Notice that satellite 19 has a very stable differential phase error signature when no intentional multipath producer is present. It is interesting that satellites 17 and 19 have such similar ground tracks but such different differential phase error signatures when no intentional multipath producer is present. It is not known why the two satellites produced such varied signatures when no intentional multipath producer was present.

Figure 7.1.6 shows the comparison data for satellite 26. Satellite 26 was entirely in the diffraction region; therefore, DECAT calculated all zeroes since it only solves for reflected signals. The differential phase errors caused by the flat plat are difficult to ascertain by looking at the measured data, and the GTD calculated errors are small. However, the frequency characteristic of the differential phase errors in the measured data is obvious, and GTD matched the measured data very well.

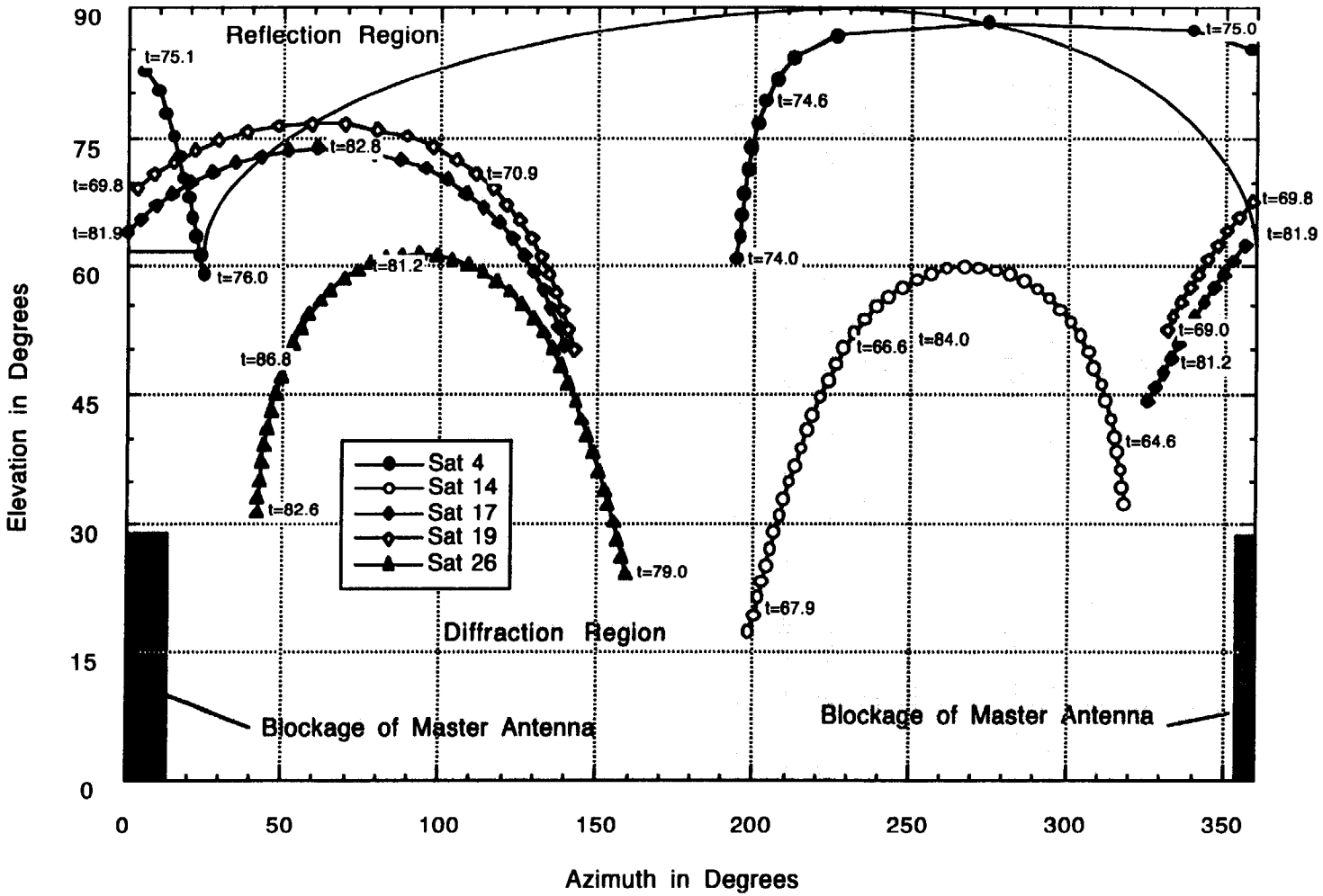

Figure 7.1.1 - Satellite tracks for JD045 with aluminum sheet and patch antennas.

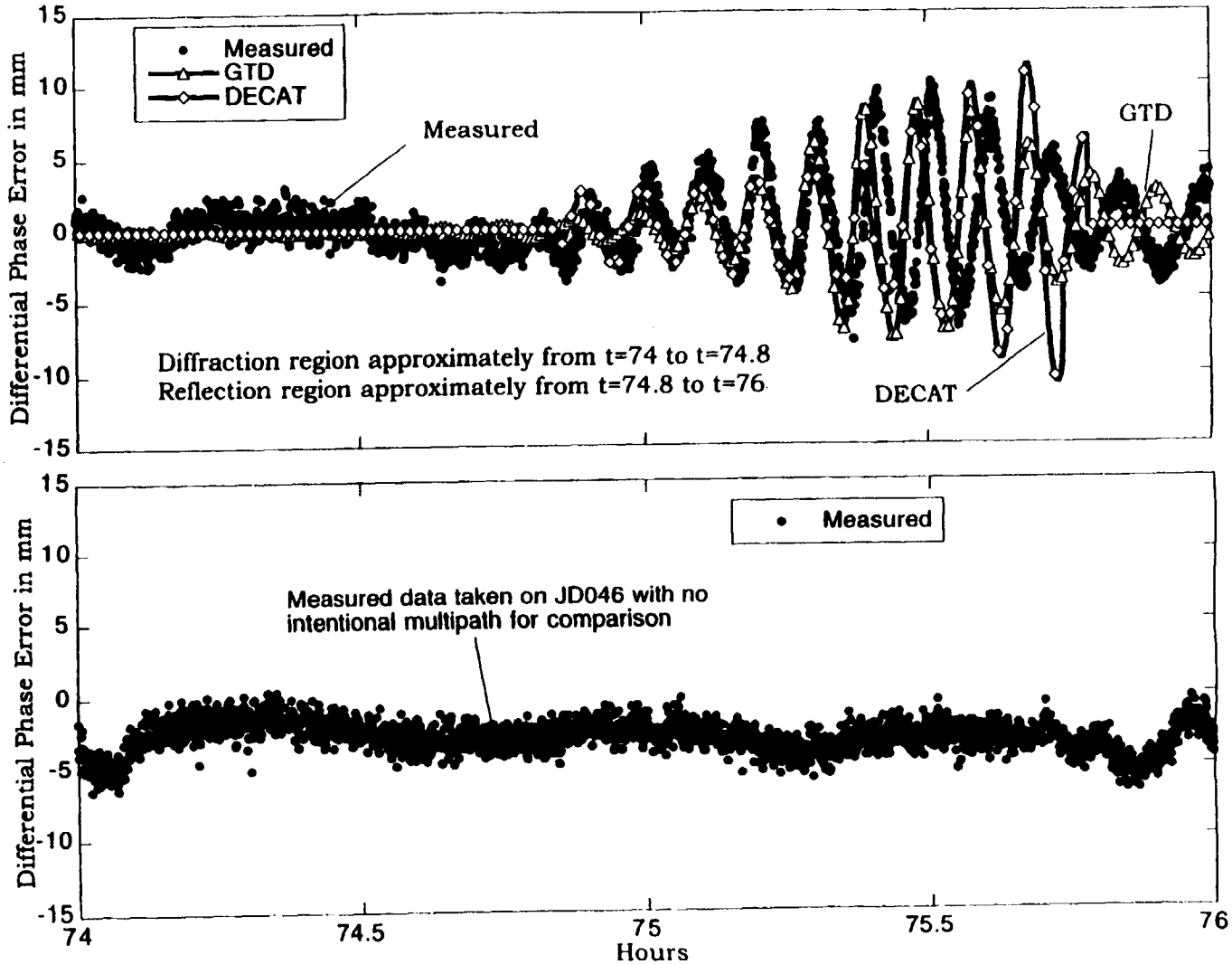

Figure 7.1.2 - Comparison of measured and predicted differential phase errors for 4-ft by 12-ft aluminum sheet with patch antennas (JD045) - satellite 4, antenna 1.

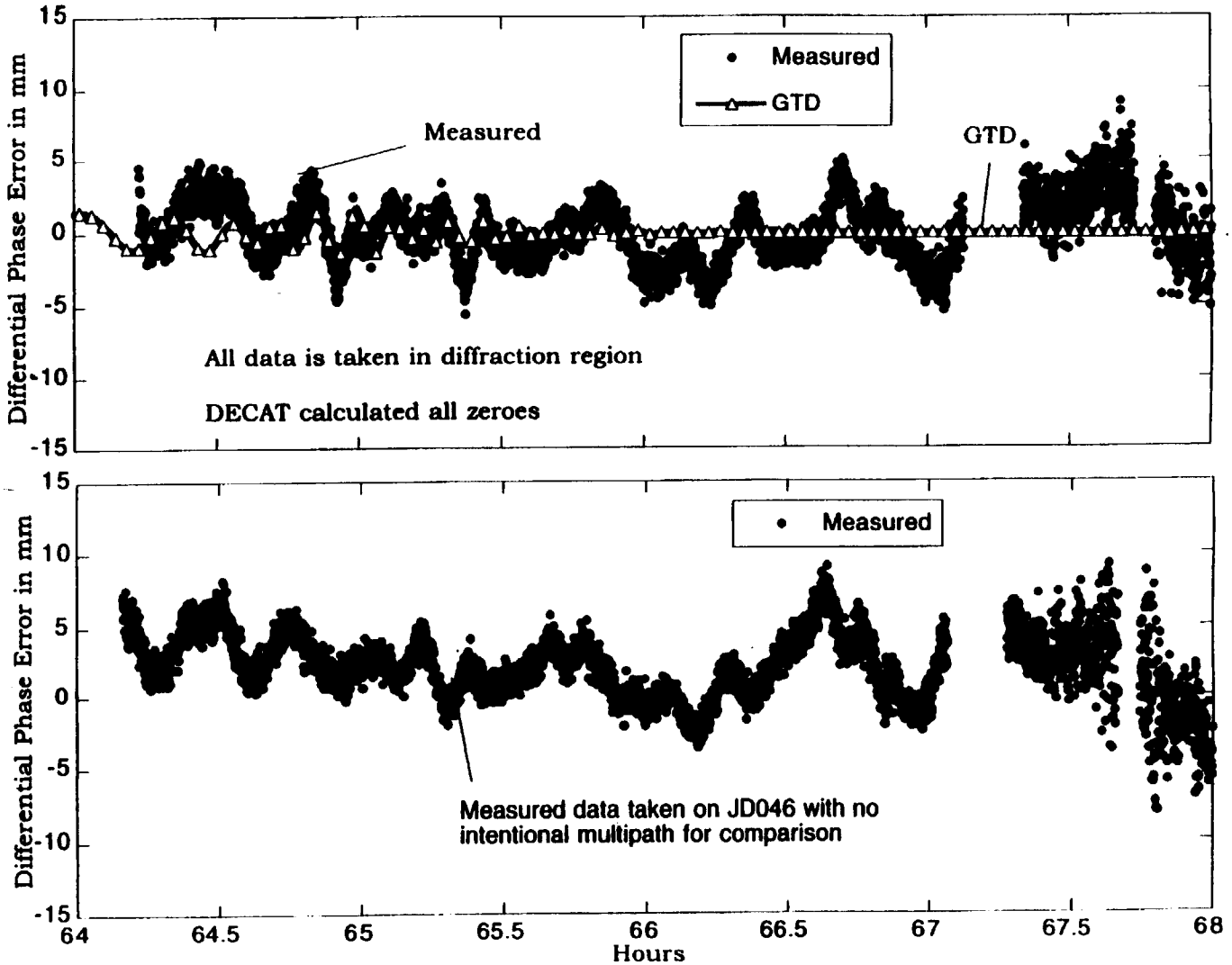

Figure 7.1.3 - Comparison of measured and predicted differential phase errors for 4-ft by 12-ft aluminum sheet with patch antennas (JD045) - satellite 14, antenna 2.

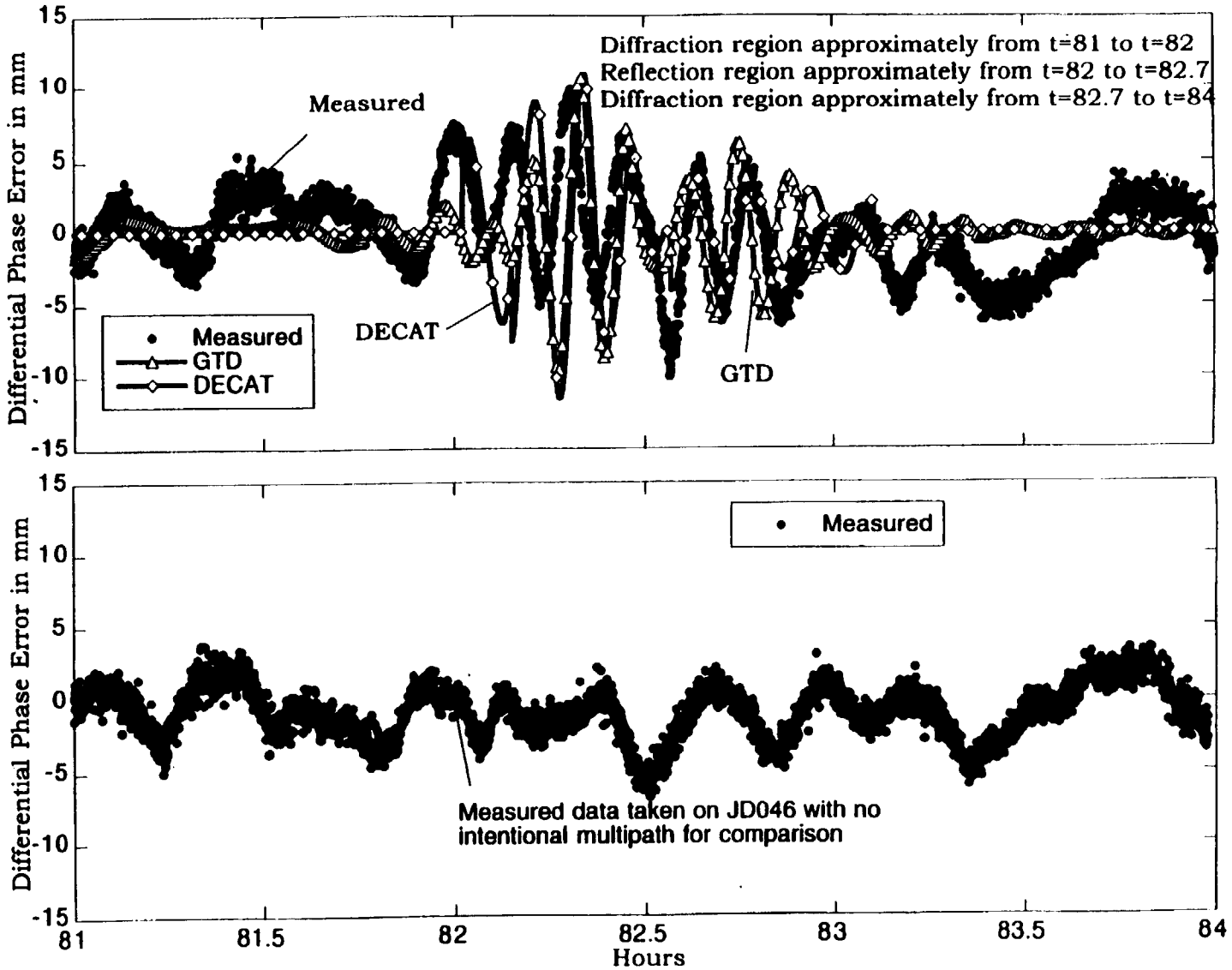

Figure 7.1.4 - Comparison of measured and predicted differential phase errors for 4-ft by 12-ft aluminum sheet with patch antennas (JD045) - satellite 17, antenna 2.

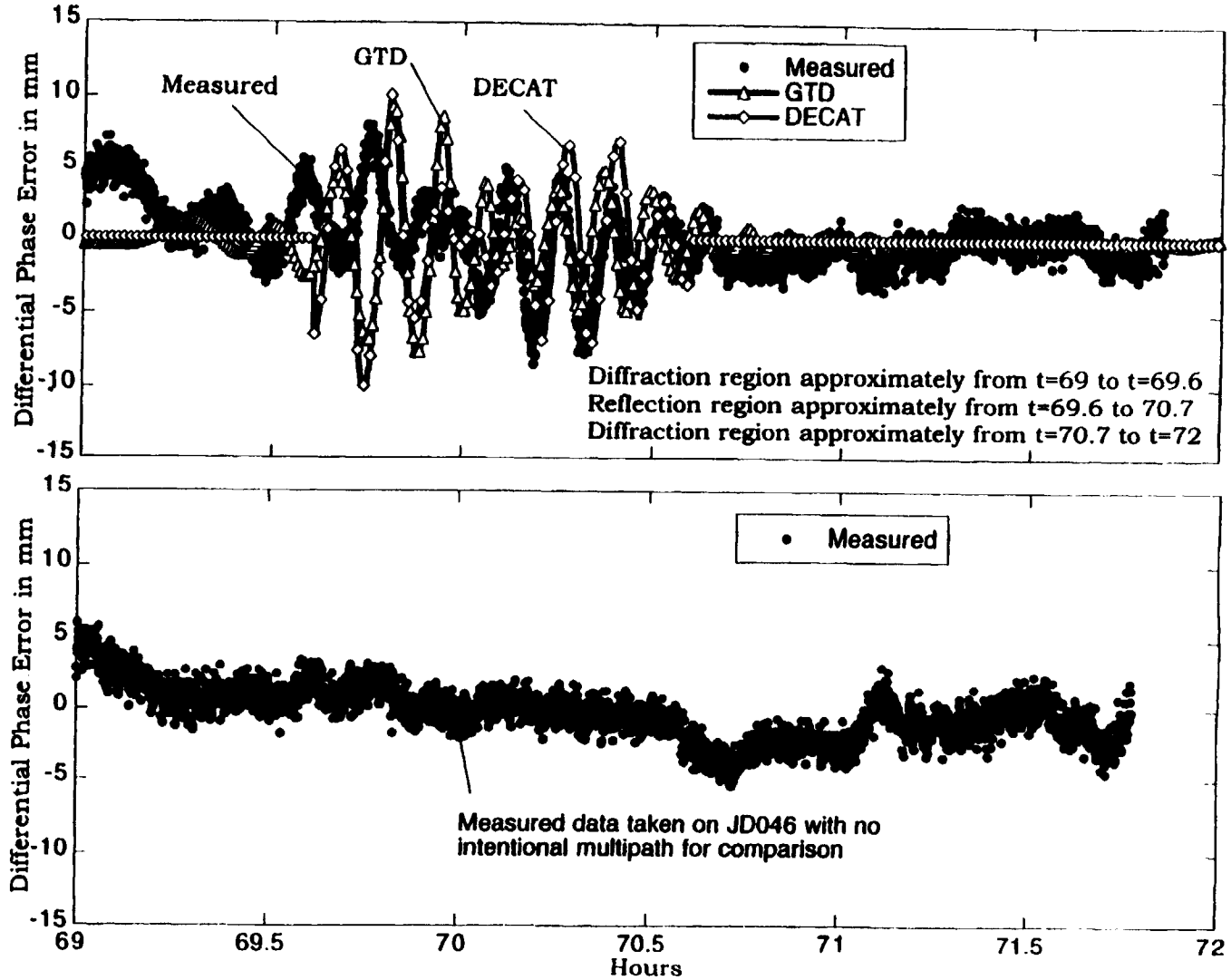

Figure 7.1.5 - Comparison of measured and predicted differential phase errors for 4-ft by 12-ft aluminum sheet with patch antennas (JD045) - satellite 19, antenna 3.

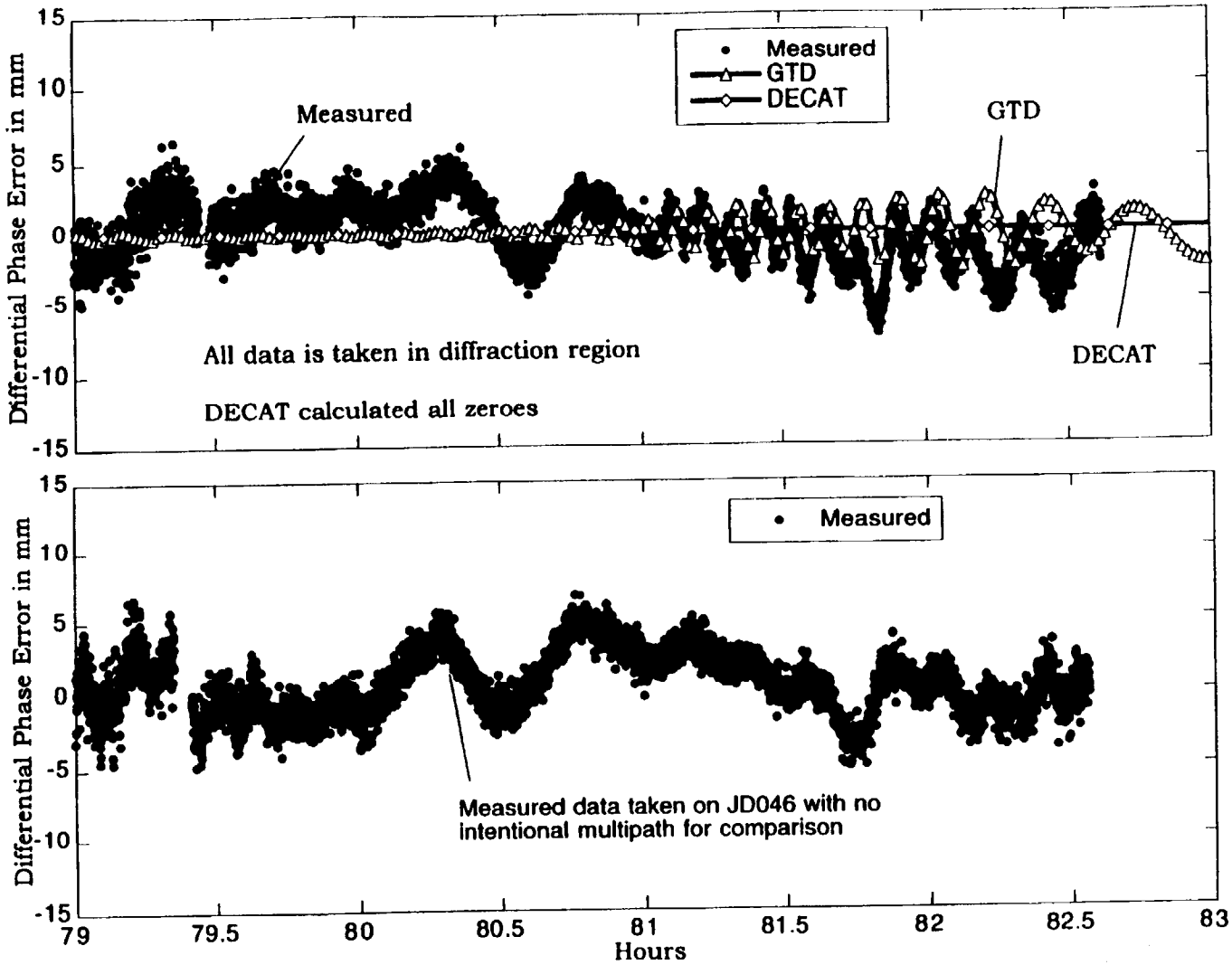

Figure 7.1.6 - Comparison of measured and predicted differential phase errors for 4-ft by 12-ft aluminum sheet with patch antennas (JD045) - satellite 26, antenna 1.

7.2 Comparison of Field Data, GTD Data, and DECAT Data for JD059 With 4-ft by 12-ft Aluminum Sheet and Patch Antennas

For JD059, the 4-ft by 12-ft aluminum sheet was placed on the South side of the table as shown in Appendix A. The satellite tracks for JD059 are shown in Figure 7.2.1. Notice that there are satellites that pass through the blockage region. The diffraction region exists predominantly below 58° and the reflection region exists above 58°.

Figure 7.2.2 shows the comparison between the field data, GTD data, and DECAT data for satellite 5. Satellite 5's ground track is almost entirely in the diffraction region, and DECAT calculated all zeroes. However, there is a noticeable multipath signature that starts at GPS time of week of 76 hours. GTD matches the frequency and magnitude of the multipath signatures very well.

Figure 7.2.3 shows the comparison data for satellite 6. Satellite 6 passes through the diffraction, reflection, and back to the diffraction regions. The differential phase errors caused by the flat plate are most noticeable in the reflection region. GTD matches the data fairly well, DECAT not quite as well, but the signature on the multipath free day is noisy, making it difficult to distinguish in the data the differential phase errors caused by the flat plate and the background differential phase errors.

Figure 7.2.4 shows the comparison data for satellite 7. Satellite 7 transitions from the diffraction region, briefly to the reflection region, and back to the diffraction region. In this case, the most noticeable multipath is in the diffraction region, and the GTD calculations match well. DECAT doesn't solve for diffracted signals, so it doesn't match the data well. The differential phase errors for the day when no intentional multipath producer is present are very small.

Figure 7.2.5 shows the comparison data for satellite 16. Satellite 16 passes through the diffraction, reflection, and blockage regions. GTD matches the measured data quite well, but as expected DECAT only matches in the reflection region. The background signature for the measured data when no intentional multipath is present has a distinct signature, and at the lower elevations, from GPS time of week 72.7 to 74, tends to have a higher standard deviation.

Figure 7.2.6 shows the comparison data for satellite 24. Satellite 24 transitions from the diffraction region, to the reflection region, and back to the diffraction region. There is a noticeable multipath signature in the measured data in the reflection region. GTD matches the measured data very well and DECAT matches not quite as well.

Figure 7.2.7 shows the comparison data for satellite 27. Satellite 27 passes through the diffraction, reflection, and blockage regions. GTD matches the measured data quite well, but, as expected, DECAT only matches in the reflection region. The background signature for the measured data when no intentional multipath is present has a distinct signature, and at the lower elevations, from GPS time of week 72.7 to 74, tends to look noisier.

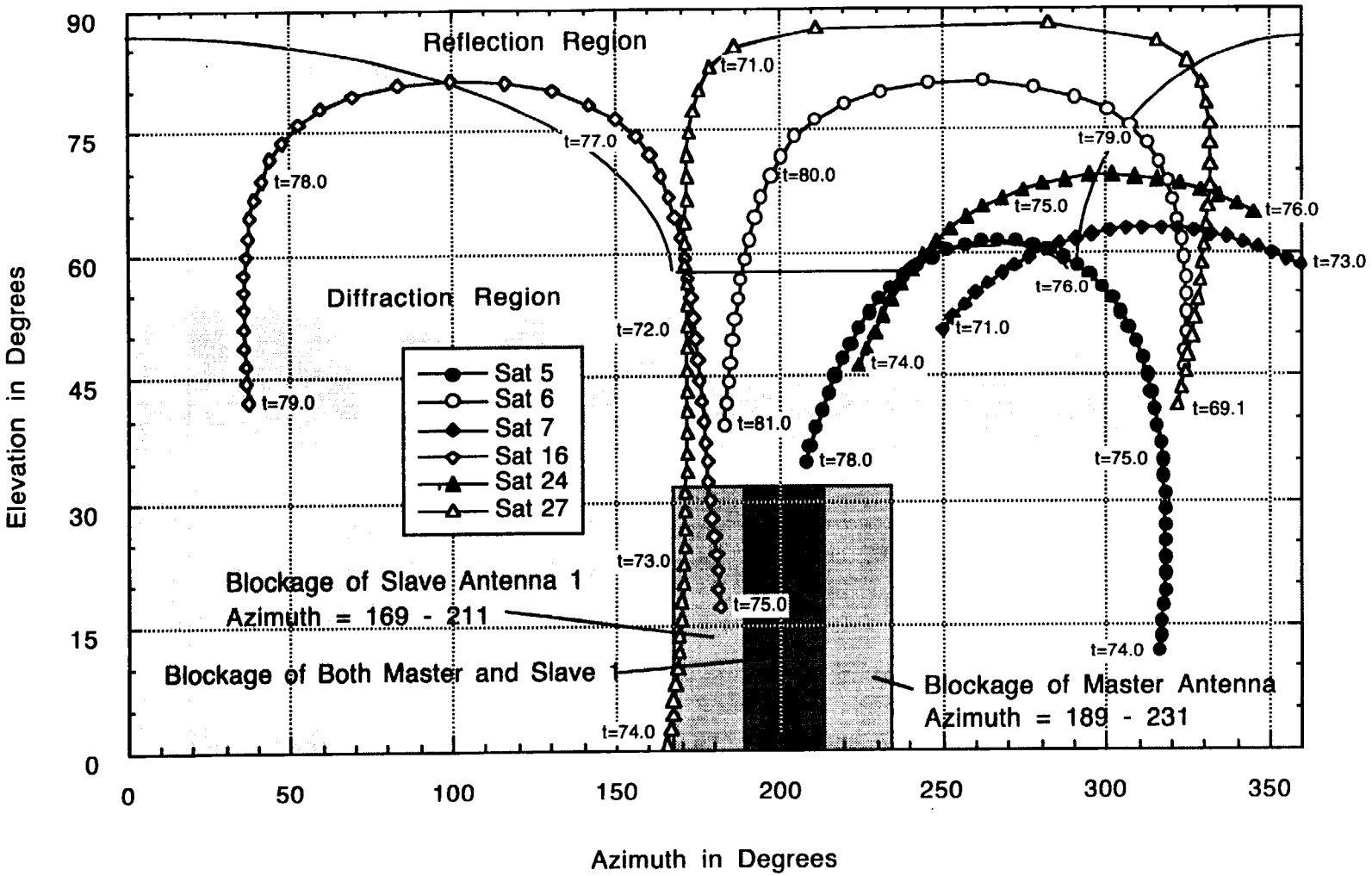

Figure 7.2.1 - Satellite tracks for JD059 with aluminum sheet and patch antennas.

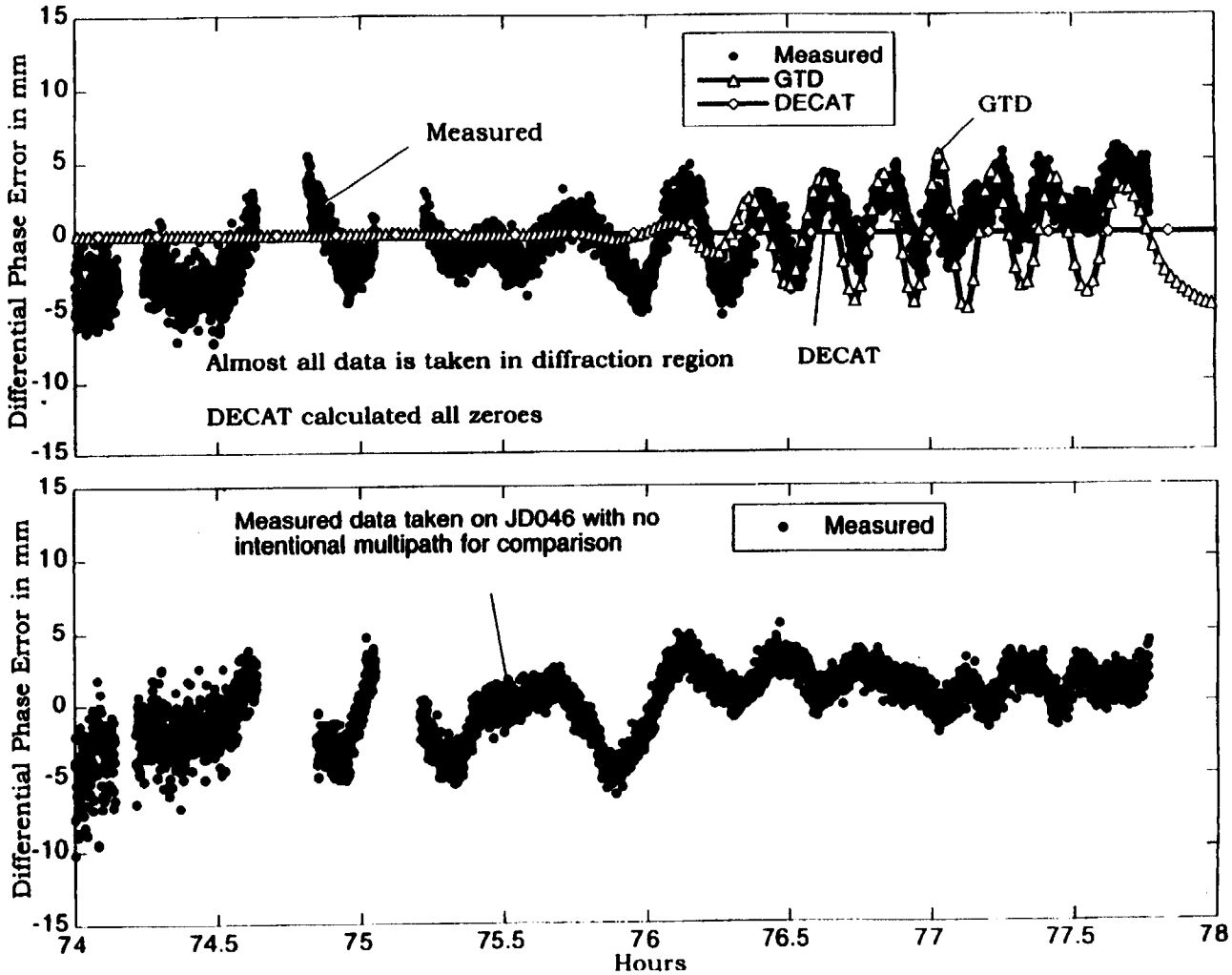

Figure 7.2.2 - Comparison of measured and predicted differential phase errors for 4-ft by 12-ft aluminum sheet with patch antennas (JD059) - satellite 5, antenna 1.

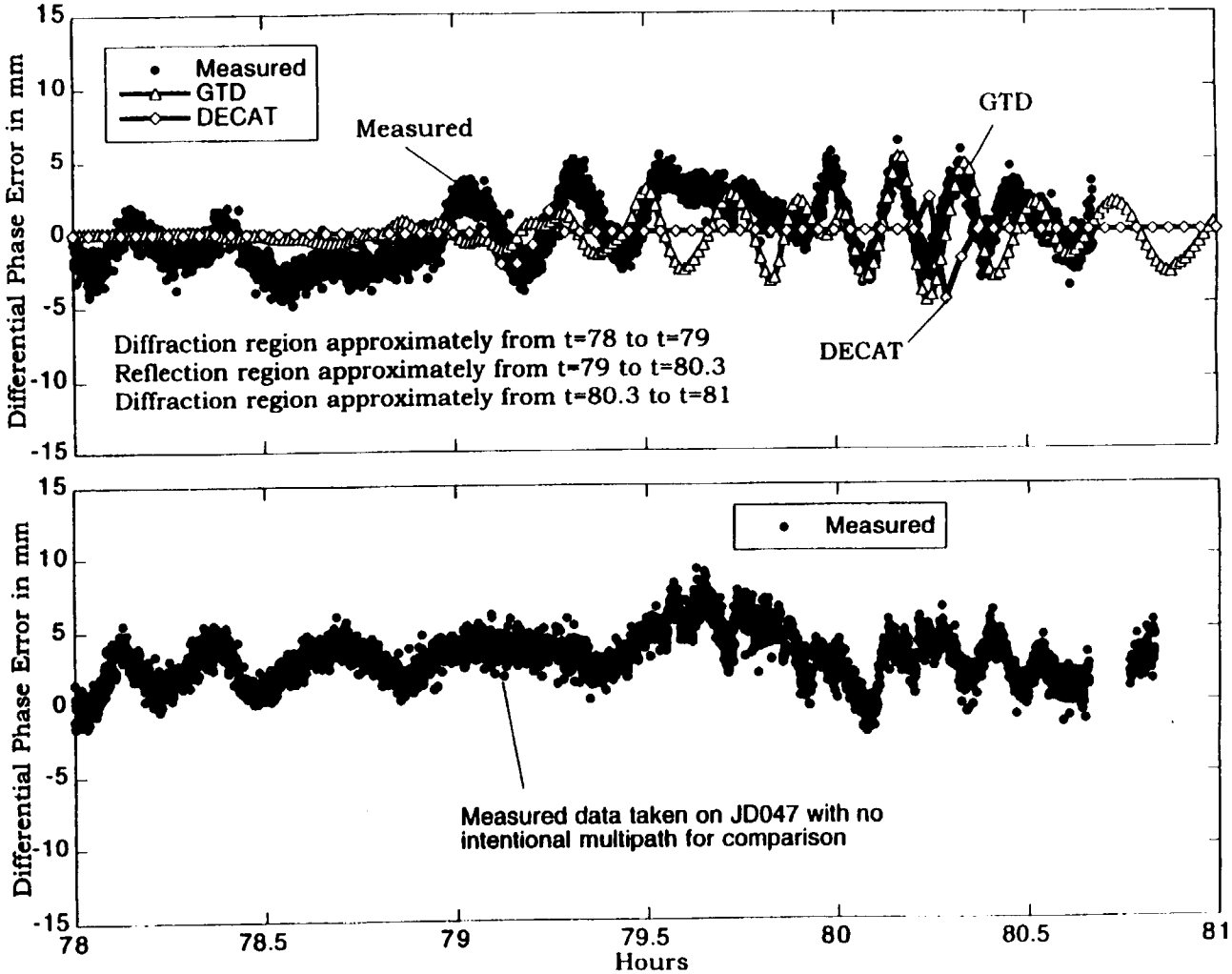

Figure 7.2.3 - Comparison of measured and predicted differential phase errors for 4-ft by 12-ft aluminum sheet with patch antennas (JD059) - satellite 6, antenna 1.

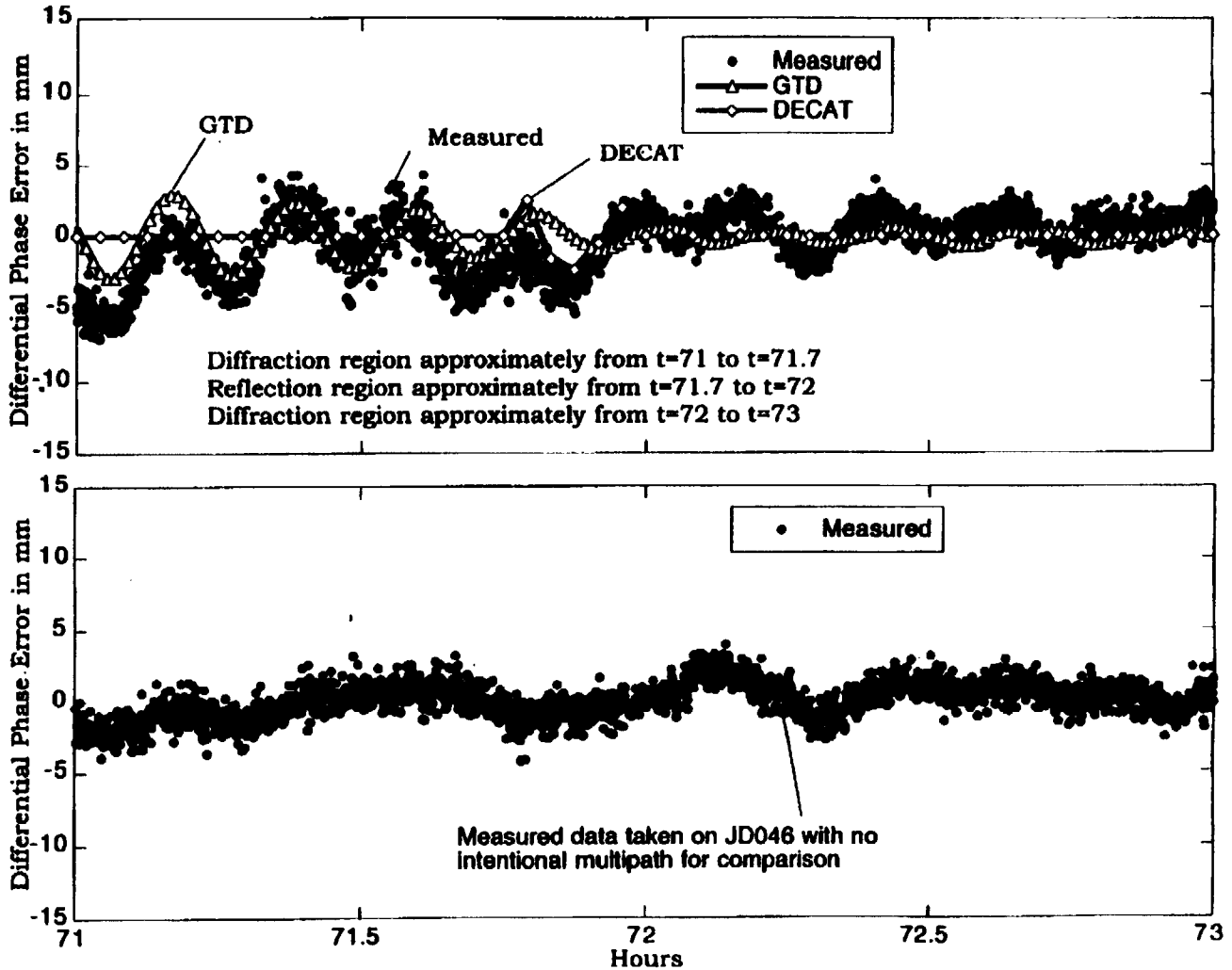

Figure 7.2.4 - Comparison of measured and predicted differential phase errors for 4-ft by 12-ft aluminum sheet with patch antennas (JD059) - satellite 7, antenna 1.

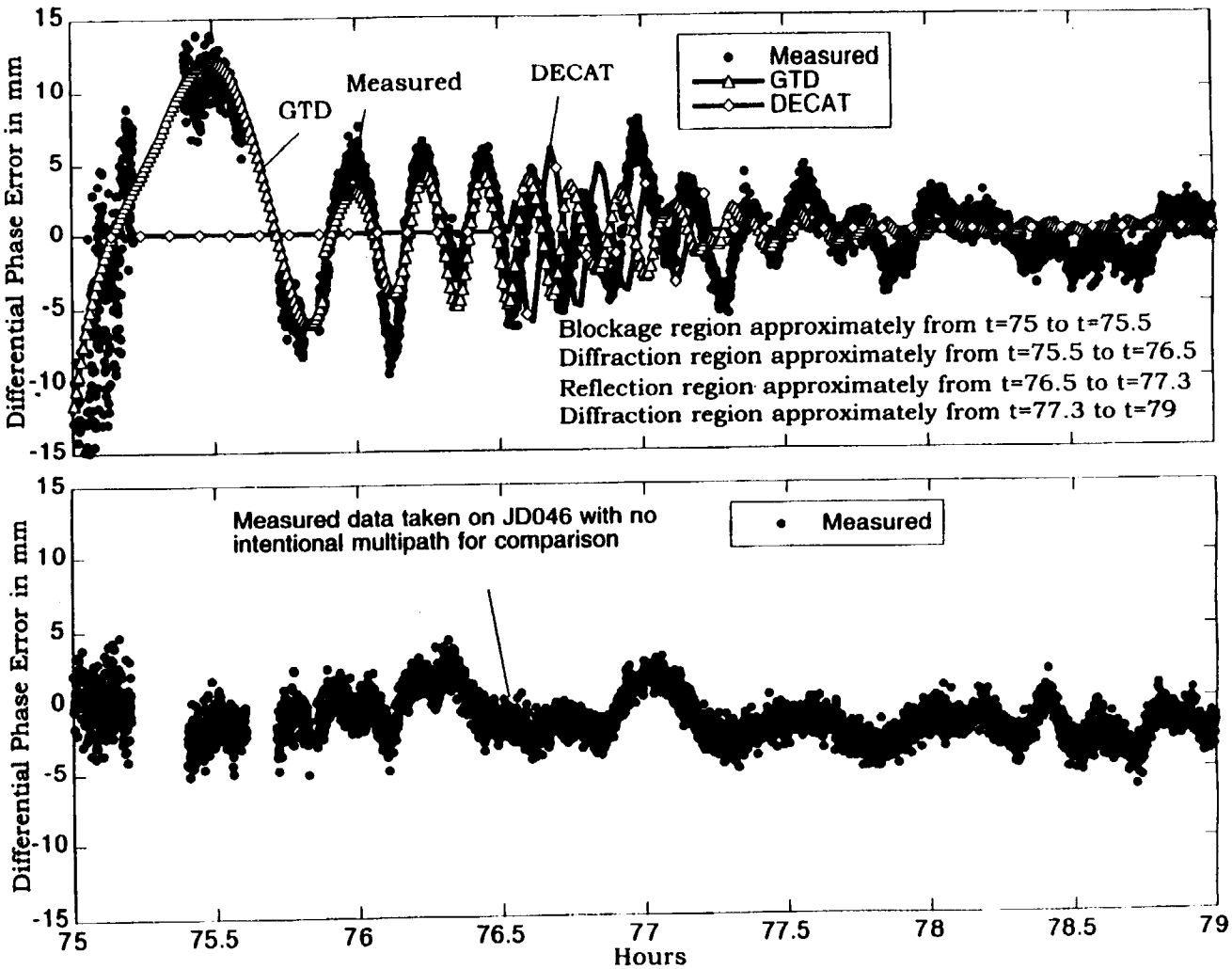

Figure 7.2.5 - Comparison of measured and predicted differential phase errors for 4-ft by 12-ft aluminum sheet with patch antennas (JD059) - satellite 16, antenna 1.

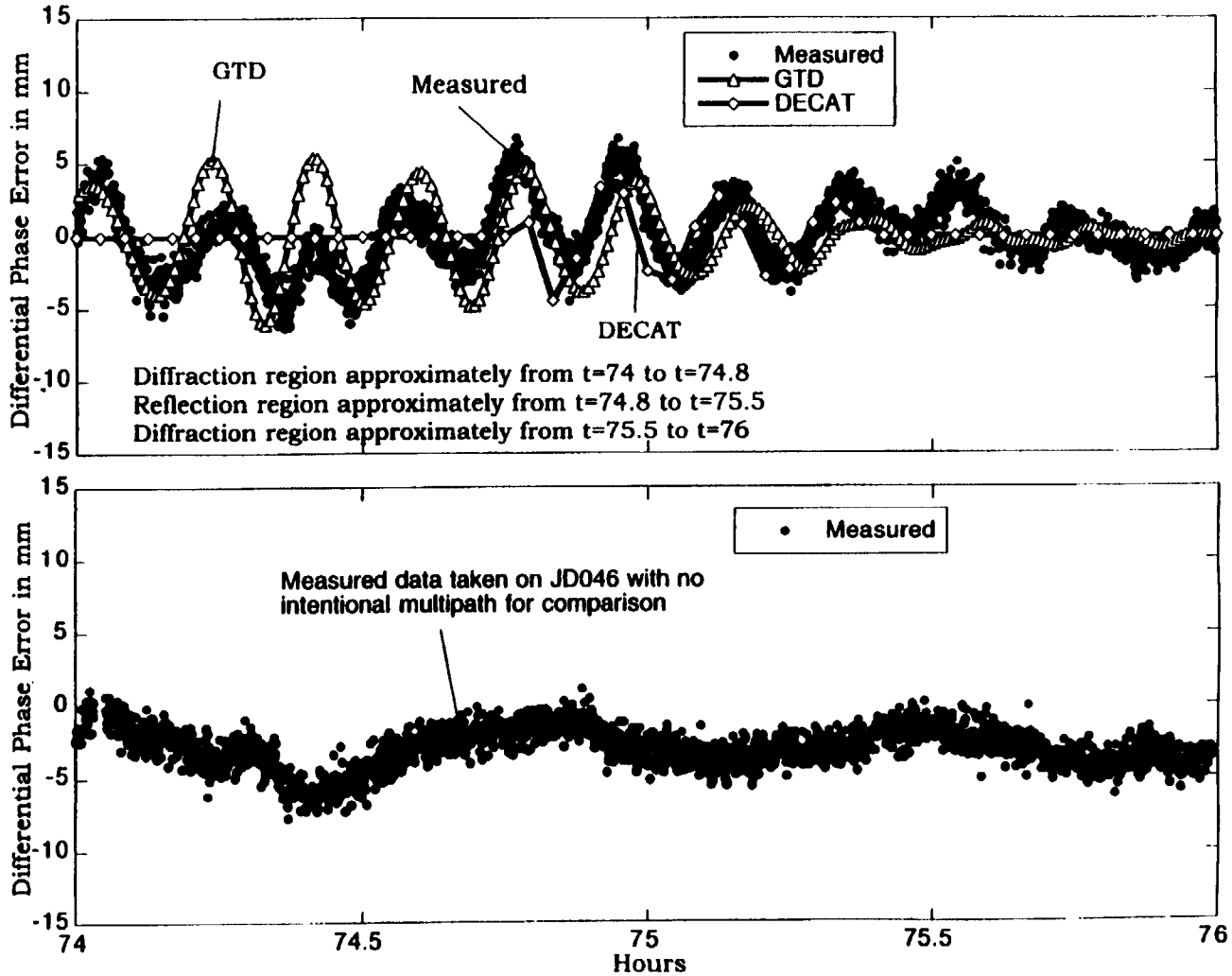

Figure 7.2.6 - Comparison of measured and predicted differential phase errors for 4-ft by 12-ft aluminum sheet with patch antennas (JD059) - satellite 24, antenna 1.

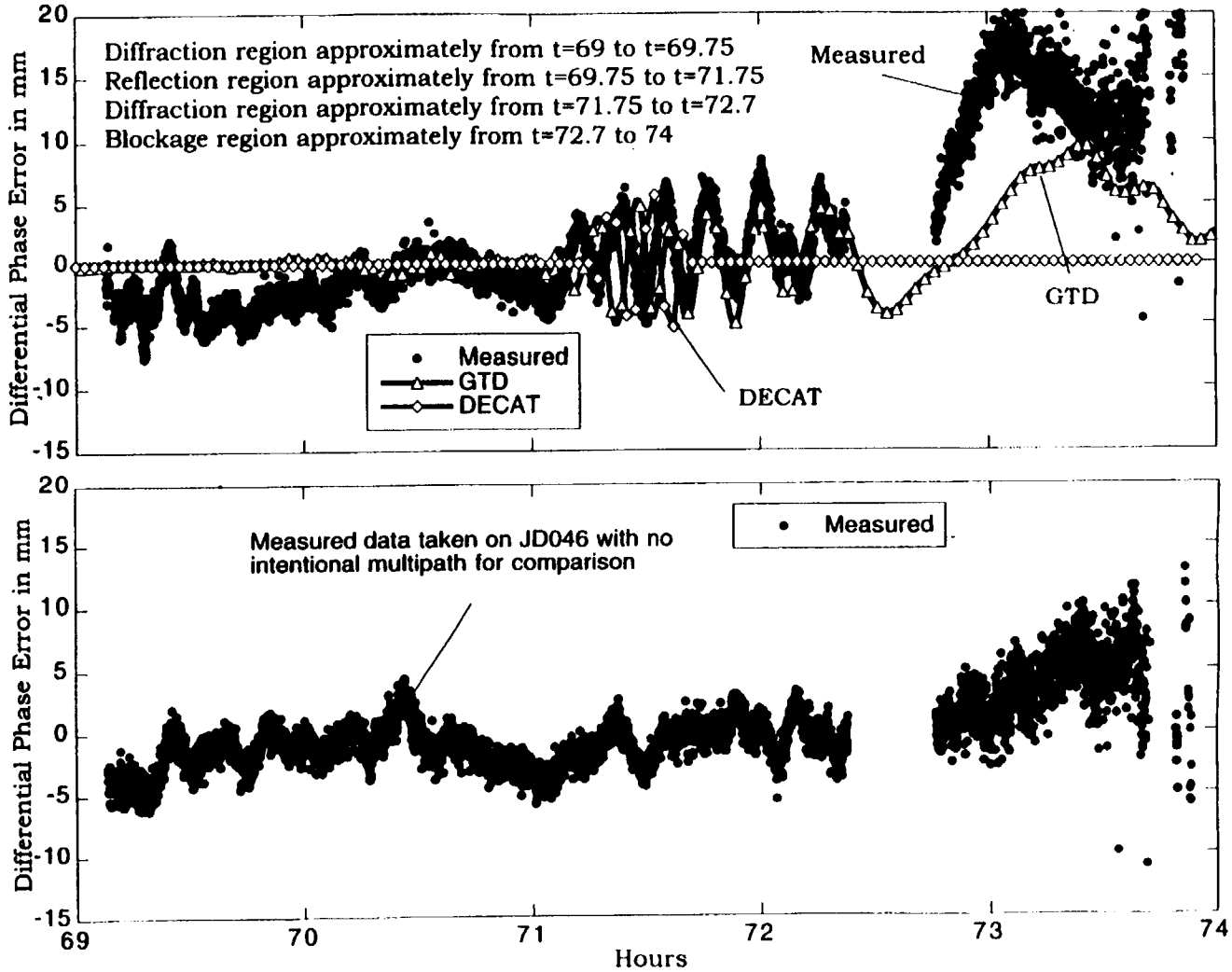

Figure 7.2.7 - Comparison of measured and predicted differential phase errors for 4-ft by 12-ft aluminum sheet with patch antennas (JD059) - satellite 27, antenna 1.

7.3 Comparison of Field Data, GTD Data, and DECAT Data for JD080 With 4-ft by 12-ft Aluminum Sheet and Choke Ring Antennas

For JD080, the 4-ft by 12-ft aluminum sheet was placed on the South side of the table with the antennas in the same position as for JD059. However, the choke ring antennas were used for JD080 and the patch antennas were used for JD059. The satellite tracks for JD080 are shown in Figure 7.3.1. The same satellites are compared in Figures 7.3.2 - 7.3.7 as were compared in section 7.2, but the choke ring antennas were used rather than the patch antennas. GTD and DECAT match the measured data with similar results as noted using the patch antennas. It is interesting to see the different multipath traces that result using the two different types of antennas. In general, the multipath traces evident in the choke ring data have a smaller magnitude than the multipath traces in the data taken using the patch antennas. The ISS opted to use choke ring antennas to reduce the magnitude of multipath. The GTD calculations match the magnitudes and frequency characteristics of the phase errors for both the patch antenna (JD059) and the choke ring antenna (JD080).

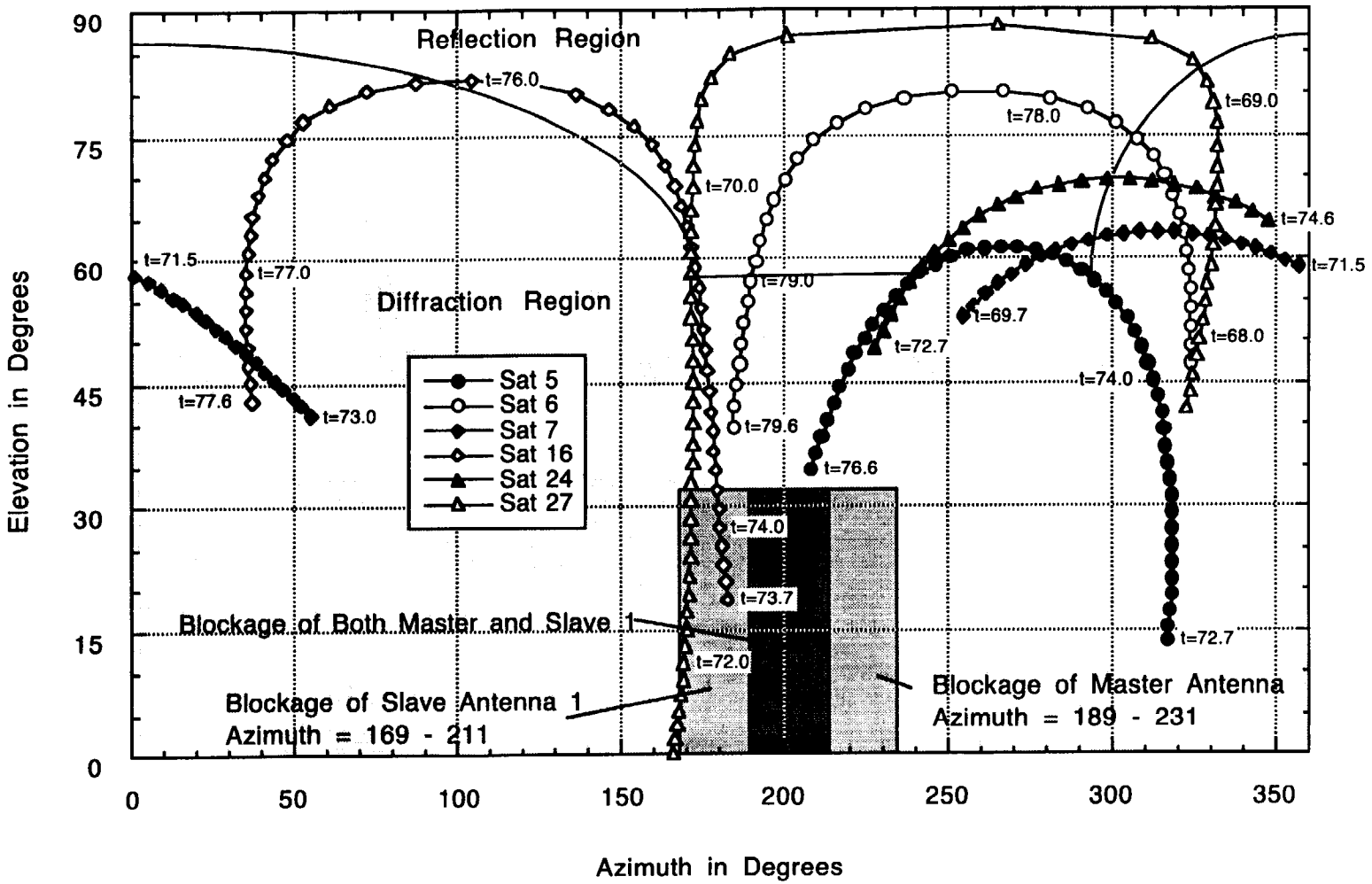

Figure 7.3.1 - Satellite tracks for JD080 with aluminum sheet and choke ring antennas.

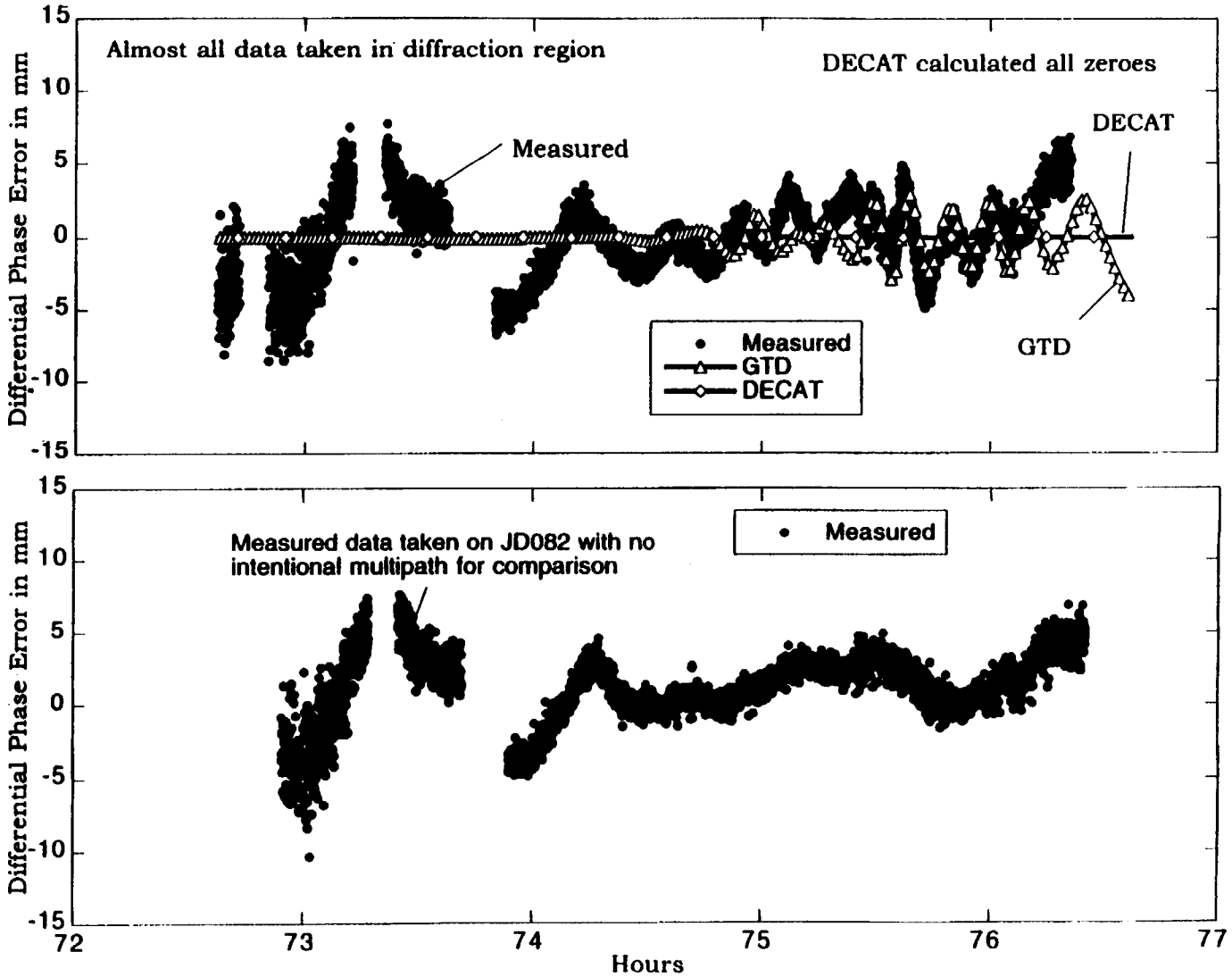

Figure 7.3.2- Comparison of measured and predicted differential phase errors for 4-ft by 12-ft aluminum sheet with choke ring antennas (JD080) - satellite 5, antenna 1.

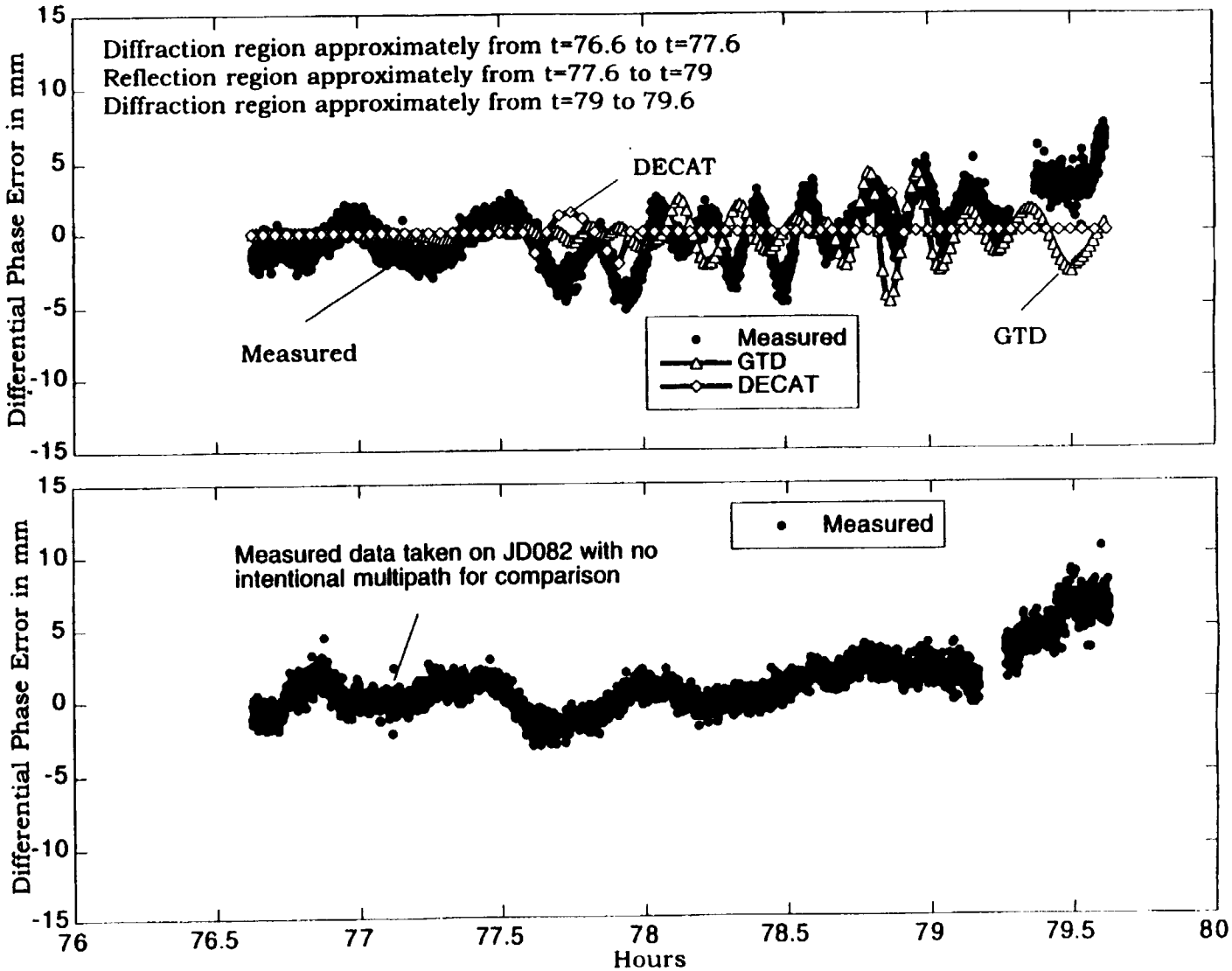

Figure 7.3.3 - Comparison of measured and predicted differential phase errors for 4-ft by 12-ft aluminum sheet with choke ring antennas (JD080) - satellite 6, antenna 1.

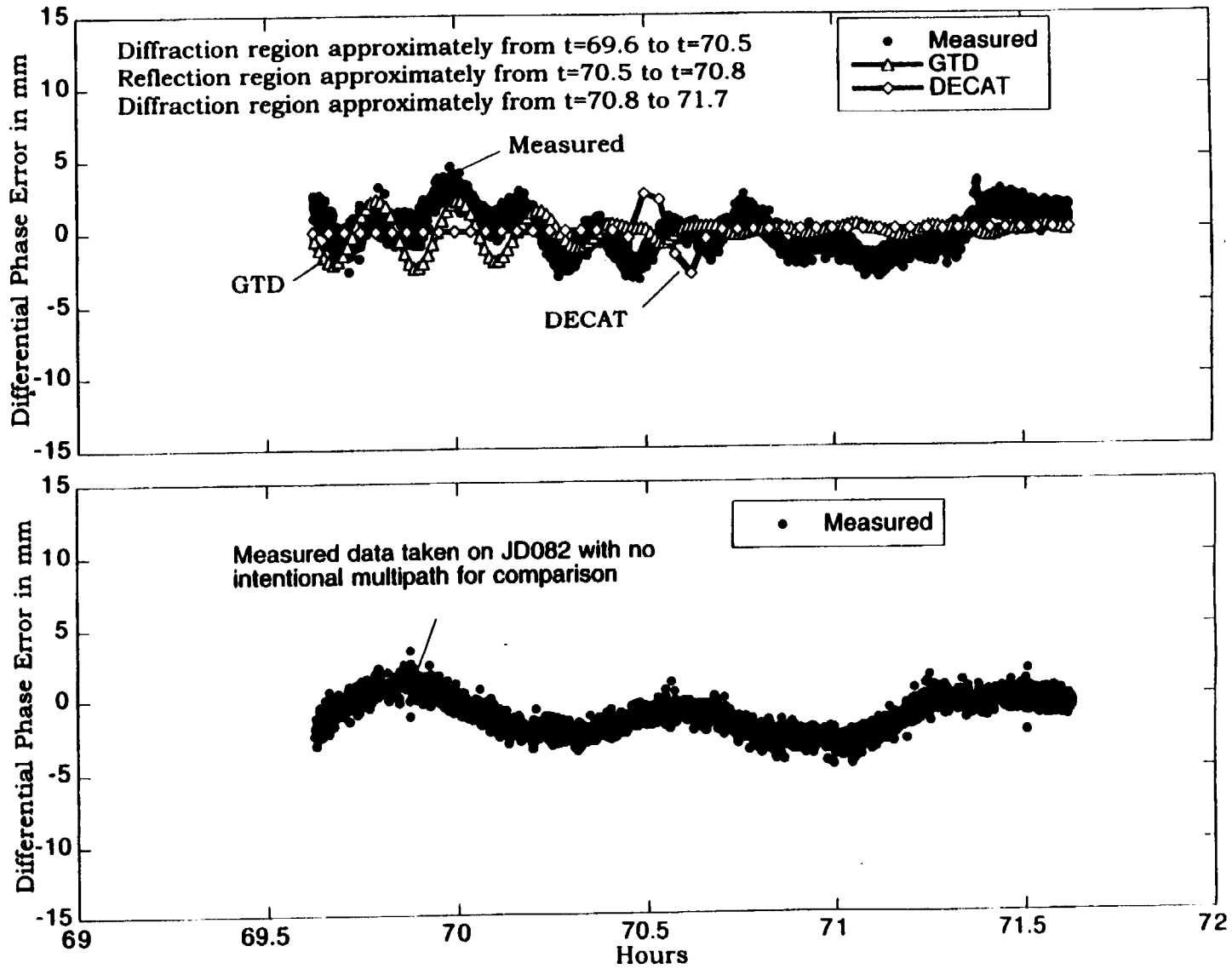

Figure 7.3.4 - Comparison of measured and predicted differential phase errors for 4-ft by 12-ft aluminum sheet with choke ring antennas (JD080) - satellite 7, antenna 1.

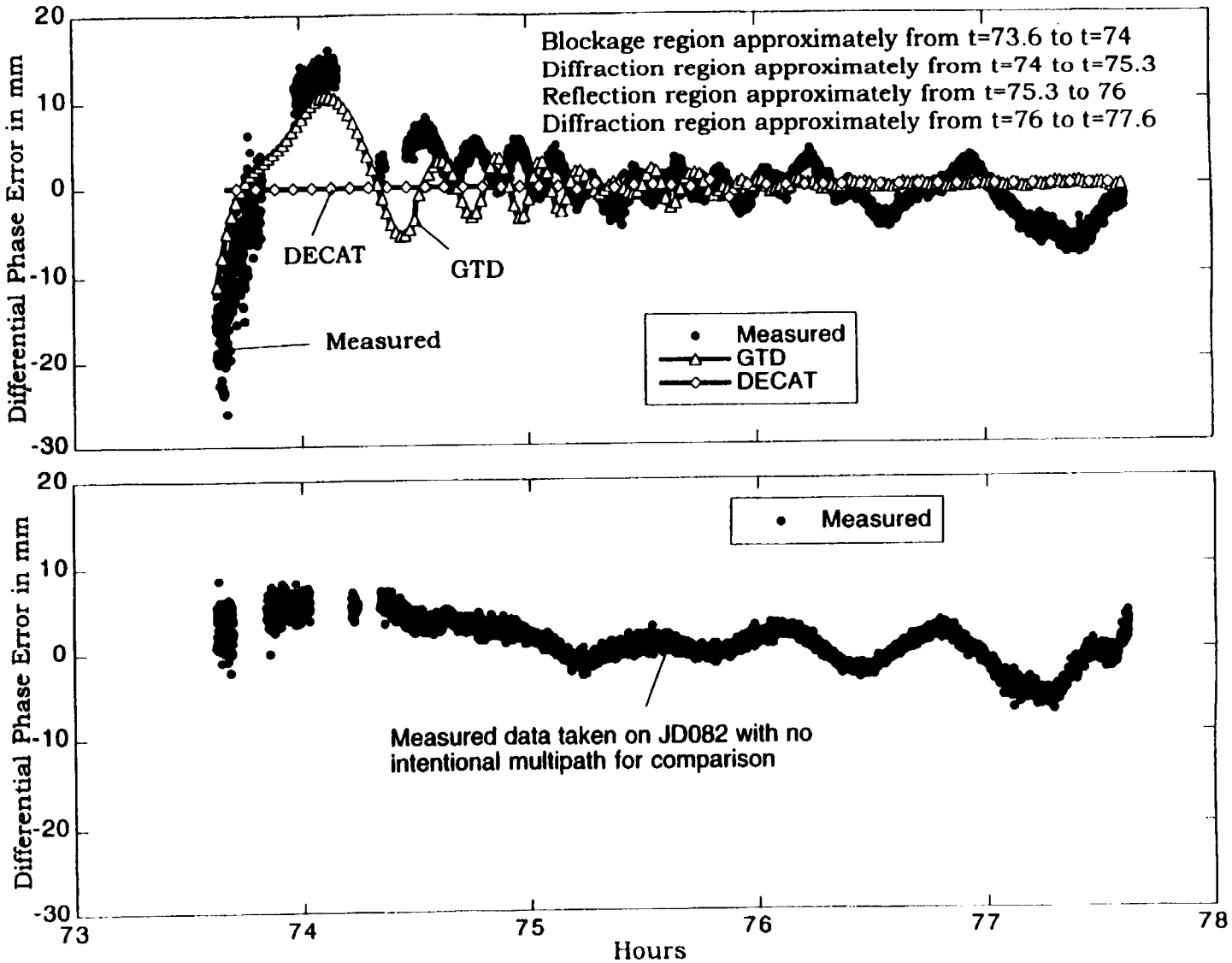

Figure 7.3.5 - Comparison of measured and predicted differential phase errors for 4-ft by 12-ft aluminum sheet with choke ring antennas (JD080) - satellite 16, antenna 1.

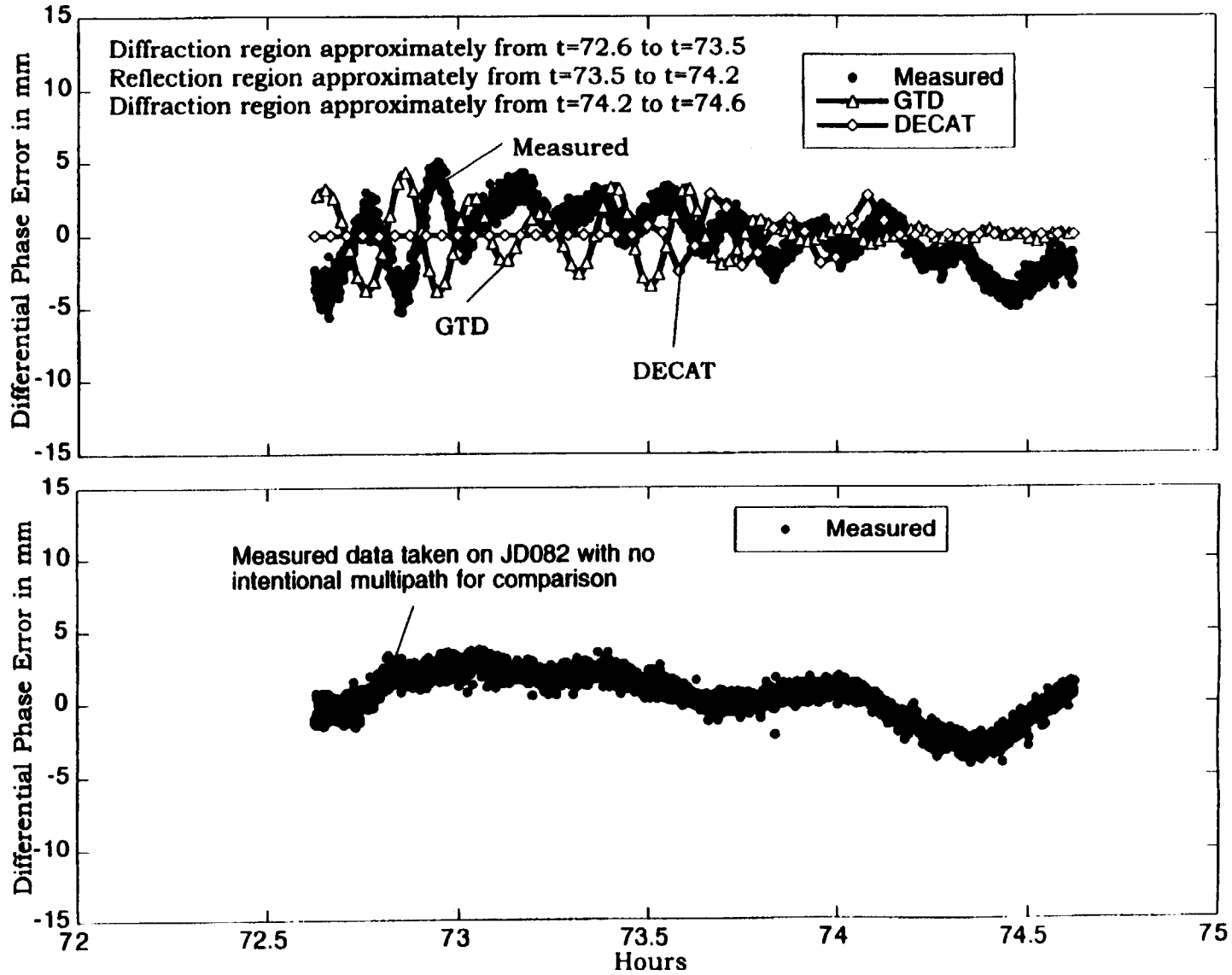

Figure 7.3.6 - Comparison of measured and predicted differential phase errors for 4-ft by 12-ft aluminum sheet with choke ring antennas (JD080) - satellite 24, antenna 1.

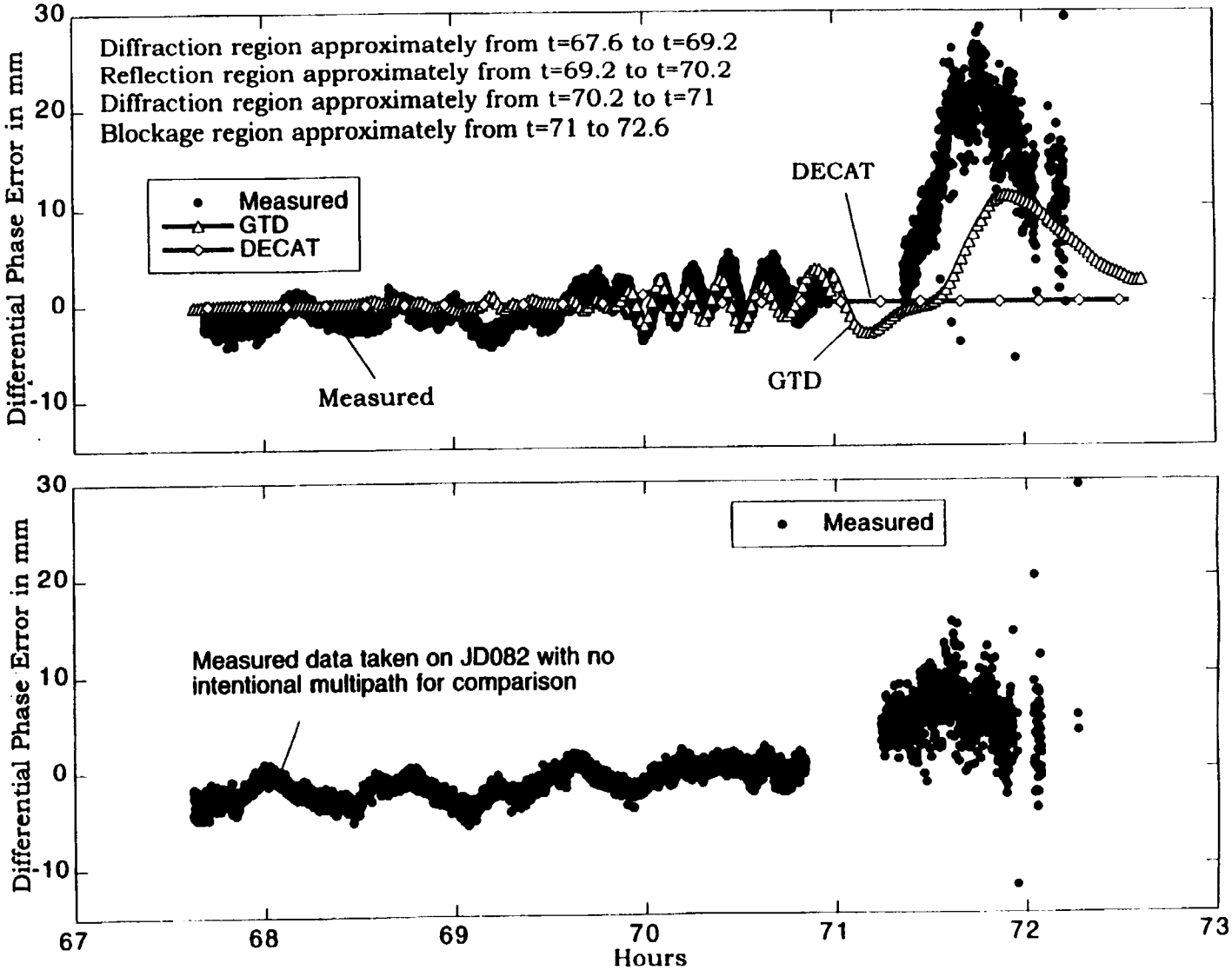

Figure 7.3.7 - Comparison of measured and predicted differential phase errors for 4-ft by 12-ft aluminum sheet with choke ring antennas (JD080) - satellite 27, antenna 1.

7.4 Comparison of Field Data, GTD Data, and DECAT Data for JD074 With 3-ft-Diameter Cylinder and Choke Ring Antennas

For JD074, the 3-ft-diameter, 4-ft-tall cylinder was placed on the South side of the choke ring antennas on the edge of the table as shown in Appendix A. The satellite tracks for JD074 are shown in Figure 7.4.1. Notice that there are satellites that pass through the blockage region, which is large in this case. The diffraction region exists above 63° and the reflection region exists below 63°. Notice that the diffraction region now exists above, rather than below, 63° since the cylinder is not tilted like the flat plate was. As expected, DECAT doesn't match the data as well for the cylinder as it did for the flat plate since it models cylinders as a collection of polygons.

Figure 7.4.2 shows the comparison between the field data, GTD data, and DECAT data for satellite 1. Satellite 1 passes through the diffraction, reflection, and blockage regions. Notice that the cylinder produces much more significant differential phase errors, as large as 30 mm, in the blockage region than did the flat plat in JD059 or JD080. GTD matches the measured data quite well.

Figure 7.4.3 shows the comparison data for satellite 4. Satellite 4 passes through the diffraction, reflection, and blockage regions. The cylinder in this case produces almost 60 mm of differential carrier phase error. GTD matches the measured data quite well.

Figure 7.4.4 shows the comparison data for satellite 5. Satellite 5 passes through the reflection, diffraction, and blockage regions. The cylinder in this case produces 95 mm, or half a wavelength, of differential carrier phase error. Knowing that the receiver will continue to track a signal with that much differential carrier phase error is significant for ISS, and knowing that the GTD calculations match that error is also significant.

Figure 7.4.5 shows the comparison data for satellite 6. Satellite 6 passes through the reflection, diffraction, and blockage regions. The cylinder in this case produces 70 mm of differential carrier phase error. Again, GTD matches the large differential carrier phase errors in the measured data quite well.

Figure 7.4.6 shows the comparison between the field data, GTD data, and DECAT data for satellite 18. Satellite 18 passes through the reflection, diffraction, and blockage regions.

Figure 7.4.7 shows the comparison data for satellite 21. Satellite 21 passes through the reflection and diffraction regions. The cylinder in this case produces much less severe differential phase errors than when there is blockage. However, it appears that neither GTD nor DECAT matches the data as well as in the previous plots. Possible reasons for this are still being investigated.

Figure 7.4.8 shows the comparison data for satellite 23. Satellite 23 passes through the reflection region only. GTD matches the data fairly well, and DECAT matches not as well. Even though DECAT models only reflections, since it modeled the cylinder as a collection of flat plates, the agreement is not as good as GTD.

Figure 7.4.9 and 7.4.10 show similar results to previous figures. It is interesting to note in Figure 7.4.10 that in the blockage region, when the satellite is blocked and at a low elevation, the measured data is much more scattered.

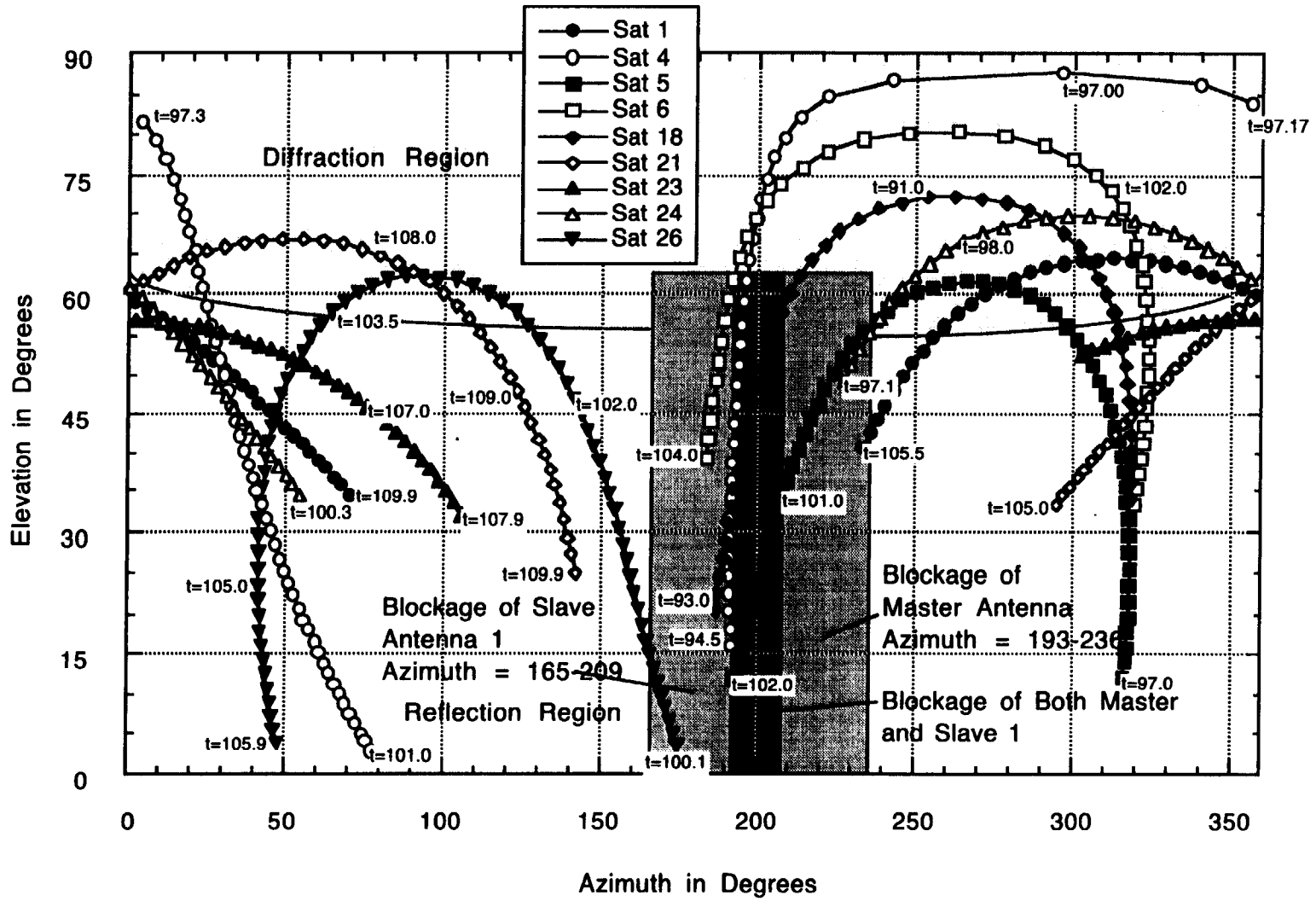

Figure 7.4.1 - Satellite tracks for JD074 with 3-ft-diameter cylinder and choke ring antennas.

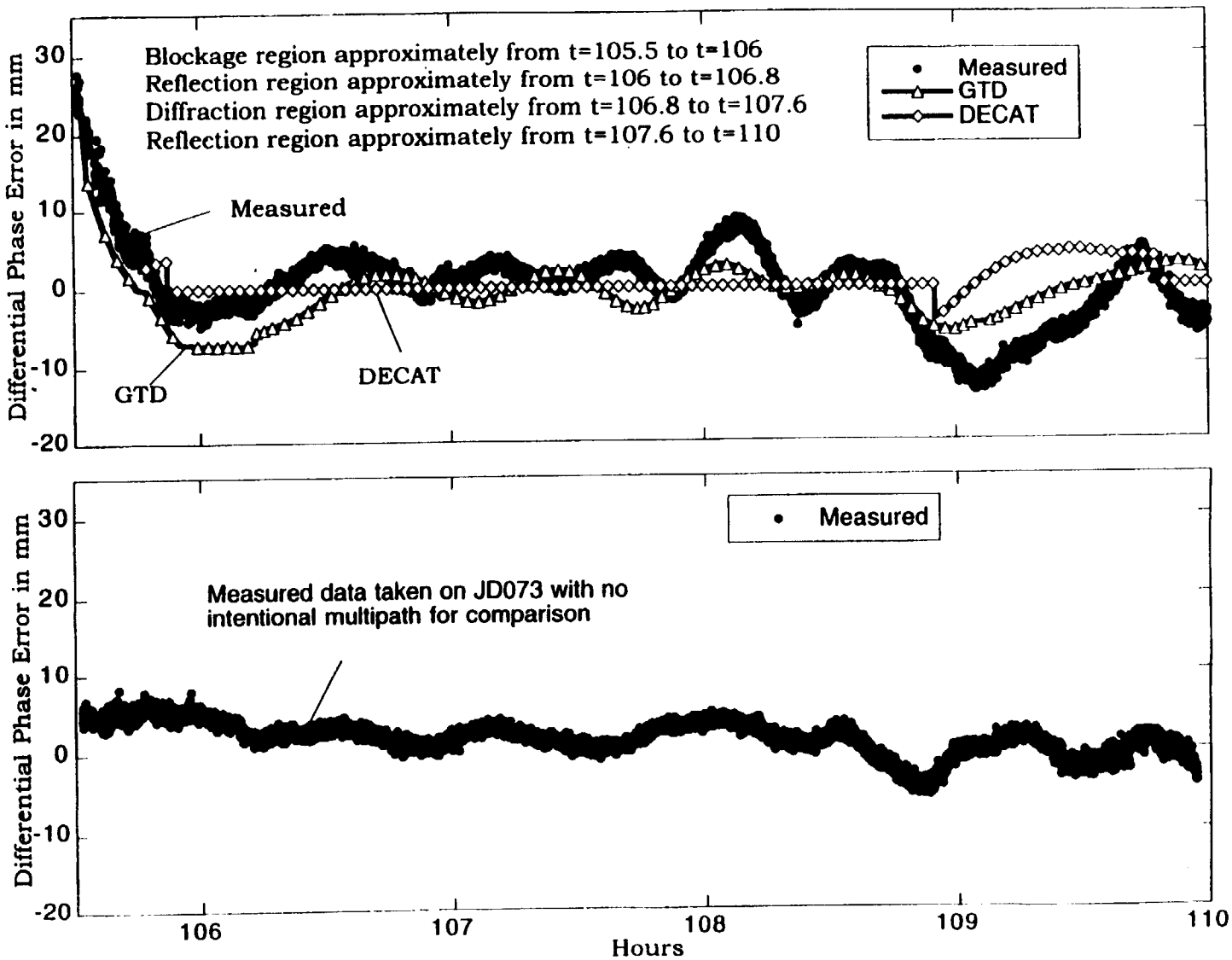

Figure 7.4.2 - Comparison of measured and predicted differential phase errors for 3-ft-diameter cylinder with choke ring antennas (JD074) - satellite 1, antenna 1.

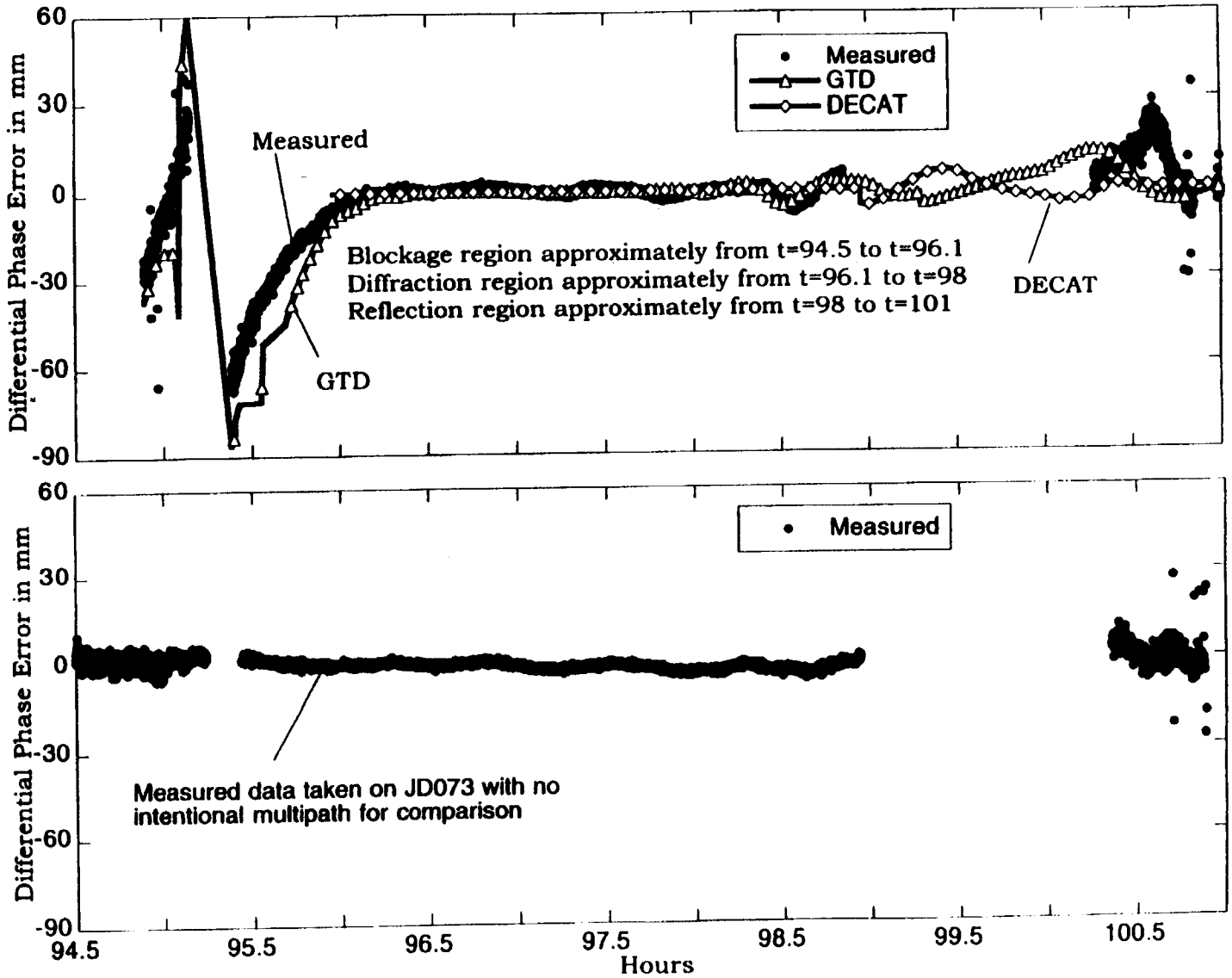

Figure 7.4.3 - Comparison of measured and predicted differential phase errors for 3-ft-diameter cylinder with choke ring antennas (JD074) - satellite 4, antenna 1.

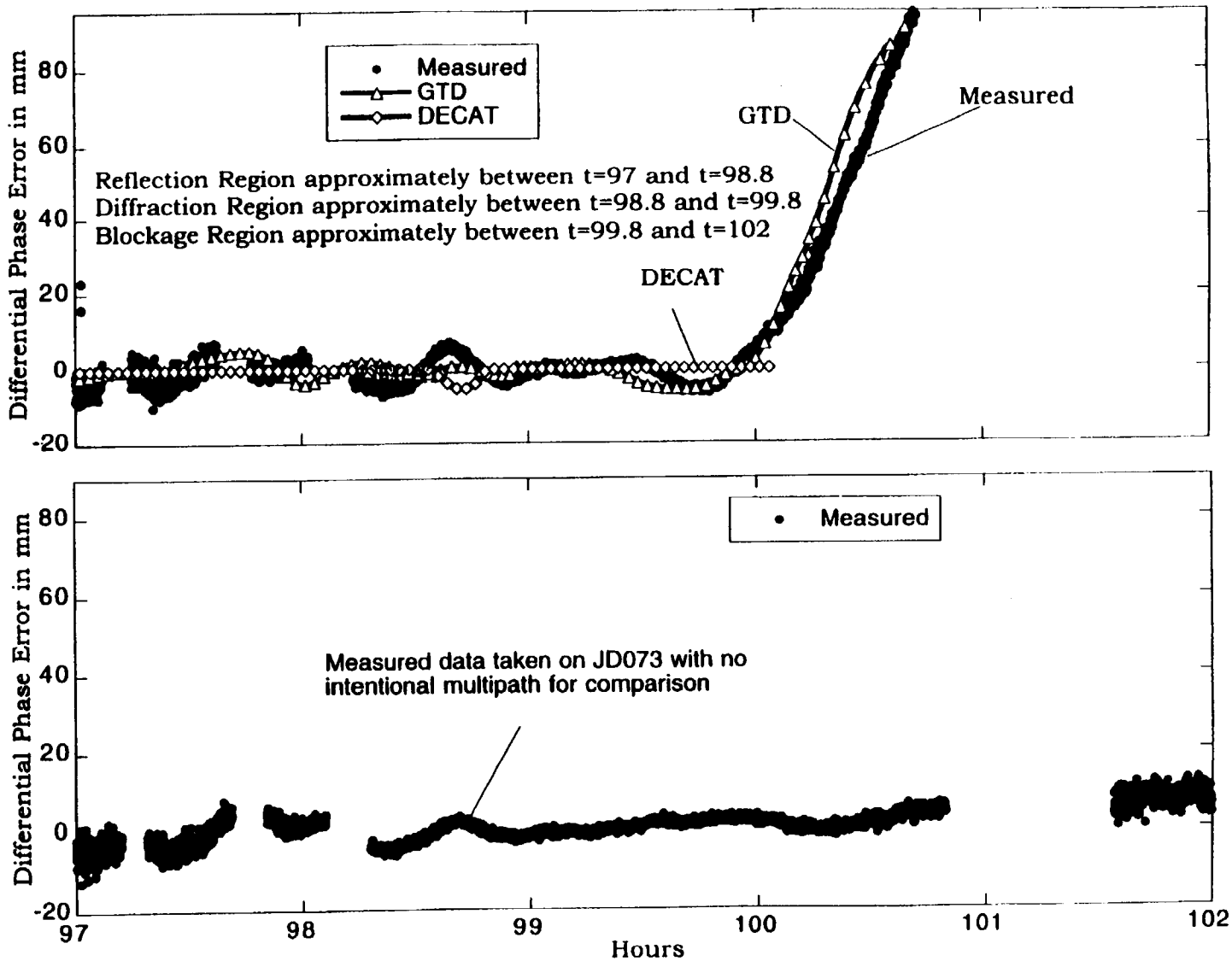

Figure 7.4.4 - Comparison of measured and predicted differential phase errors for 3-ft-diameter cylinder with choke ring antennas (JD074) - satellite 5, antenna 1.

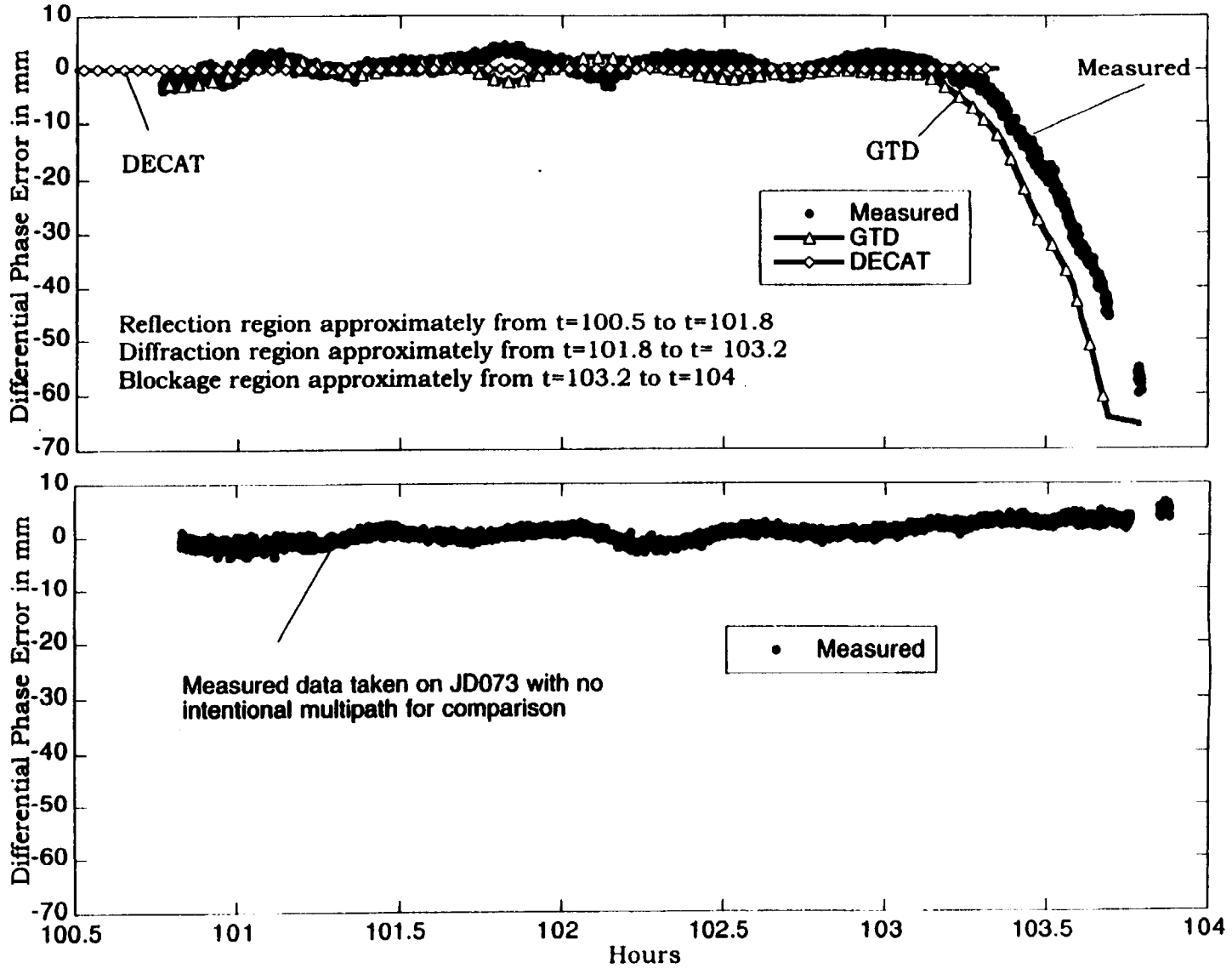

Figure 7.4.5 - Comparison of measured and predicted differential phase errors for 3-ft-diameter cylinder with choke ring antennas (JD074) - satellite 6, antenna 1.

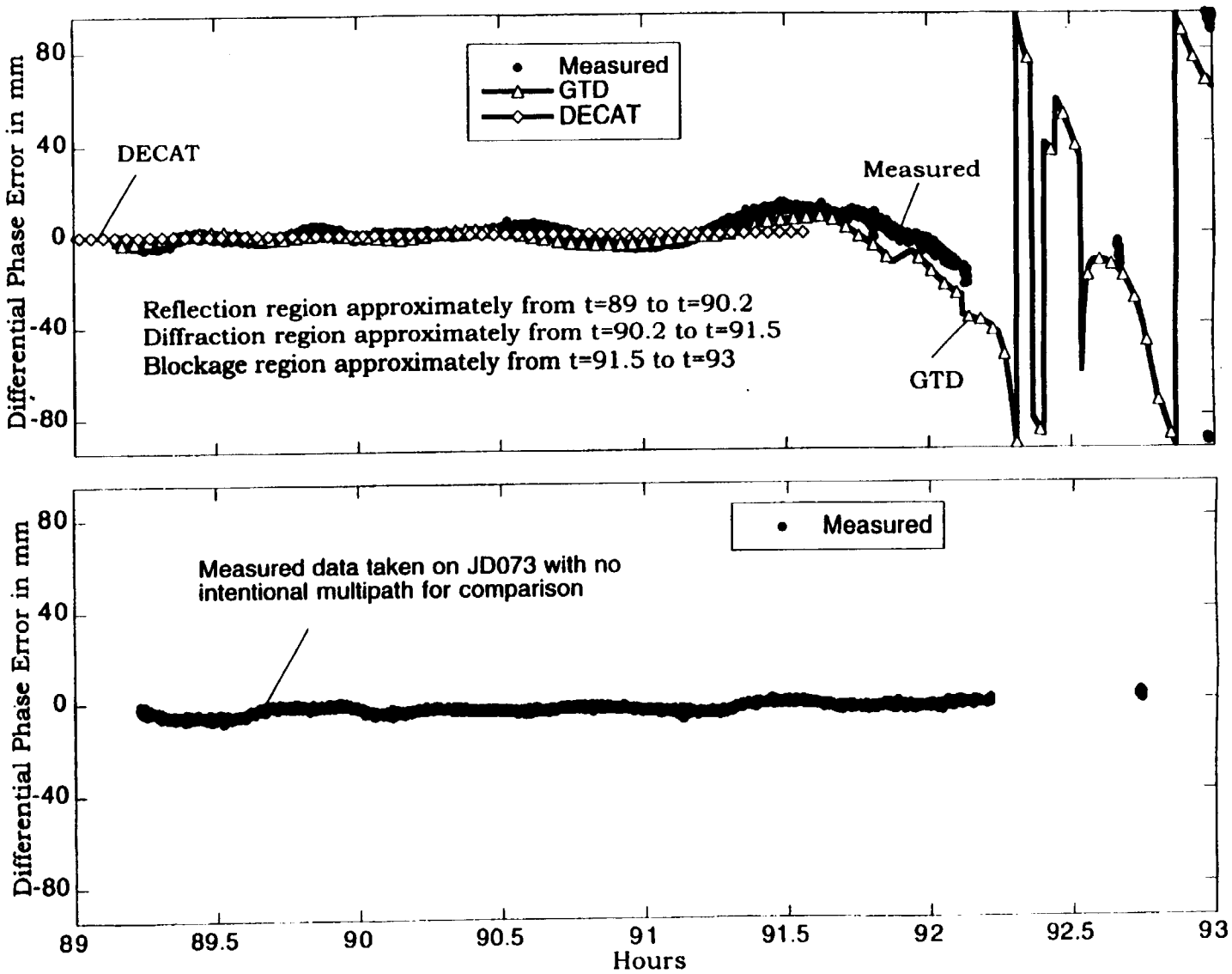

Figure 7.4.6 - Comparison of measured and predicted differential phase errors for 3-ft-diameter cylinder with choke ring antennas (JD074) - satellite 18, antenna 1.

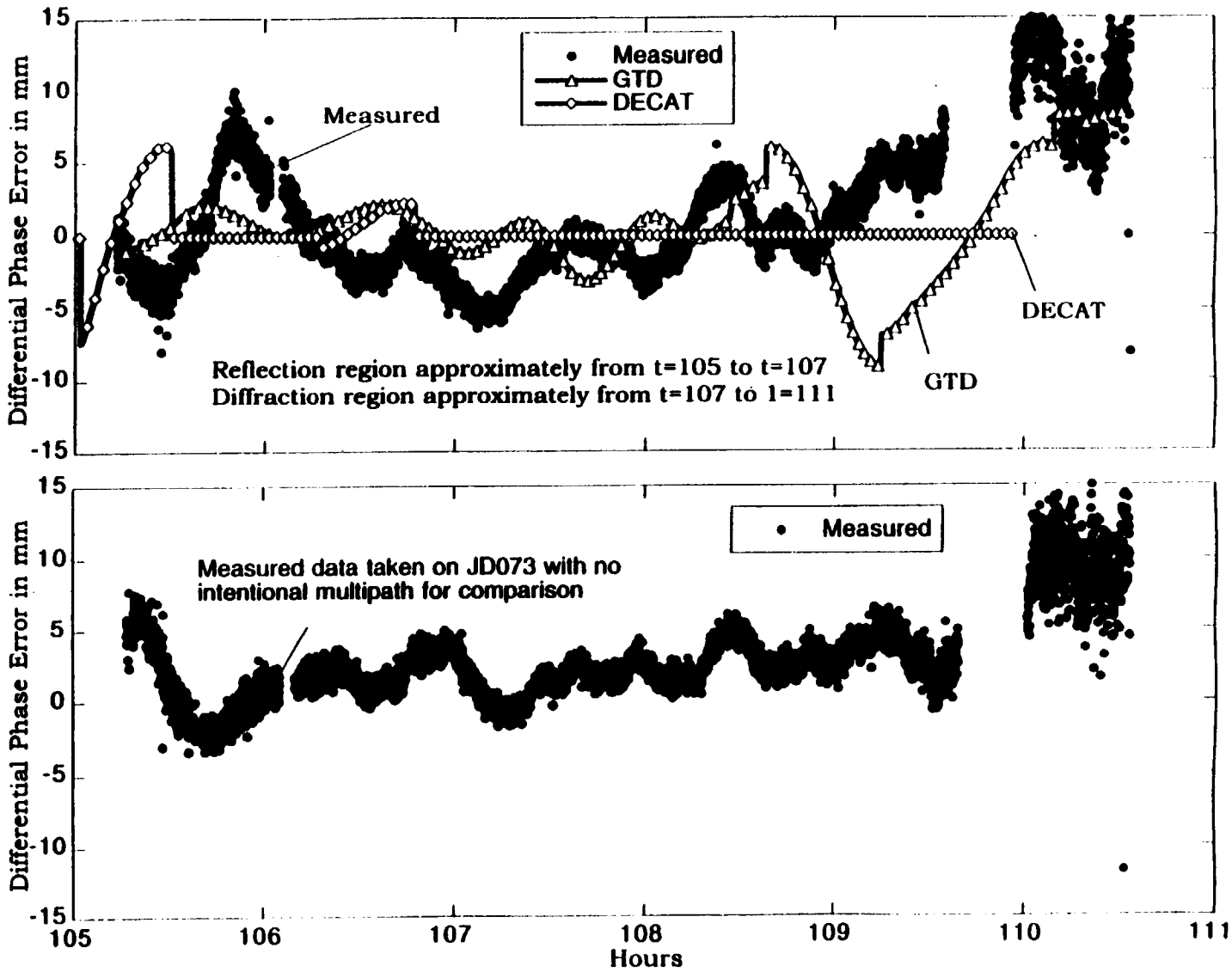

Figure 7.4.7 - Comparison of measured and predicted differential phase errors for 3-ft-diameter cylinder with choke ring antennas (JD074) - satellite 21, antenna 1.

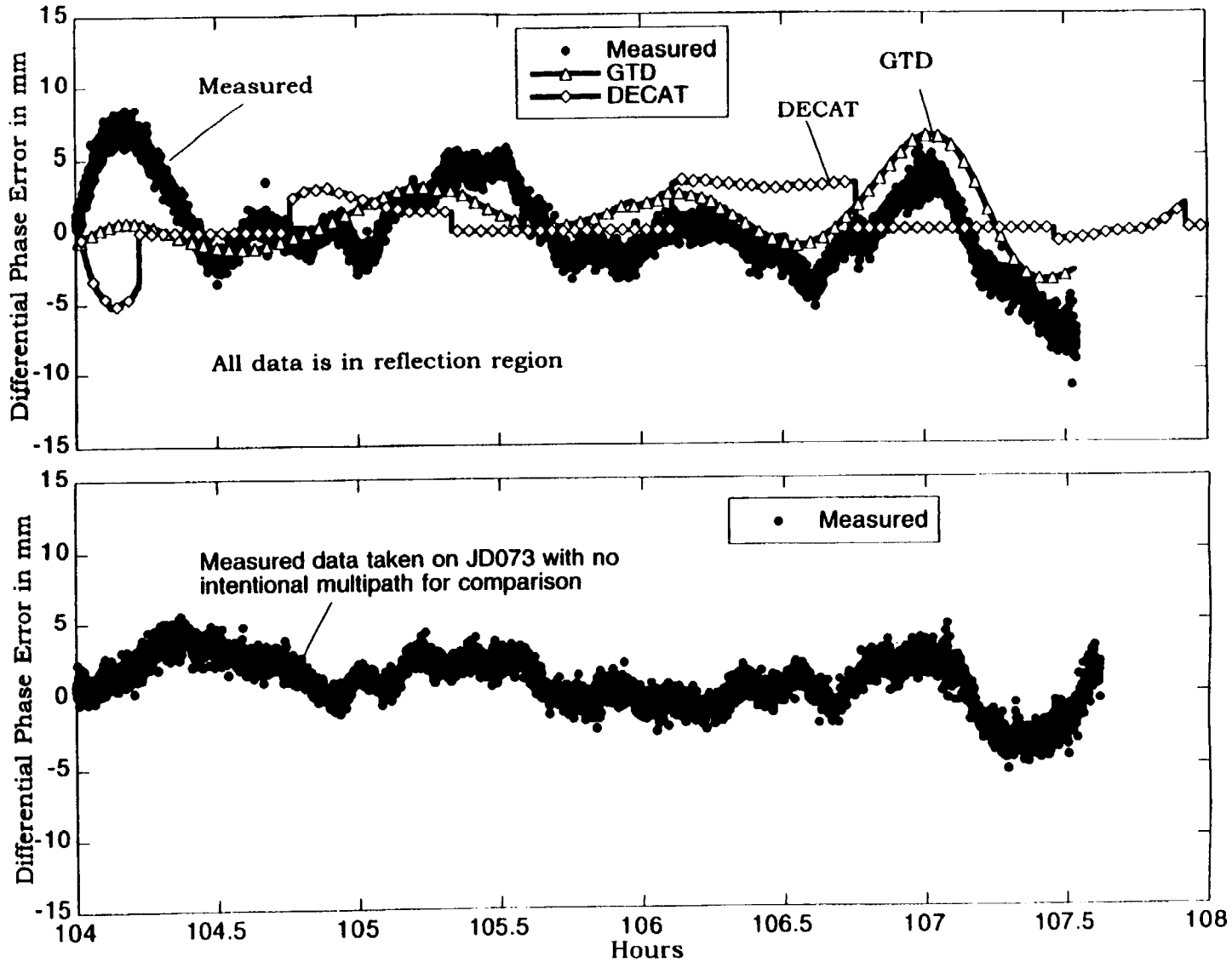

Figure 7.4.8 - Comparison of measured and predicted differential phase errors for 3-ft-diameter cylinder with choke ring antennas (JD074) - satellite 23, antenna 1.

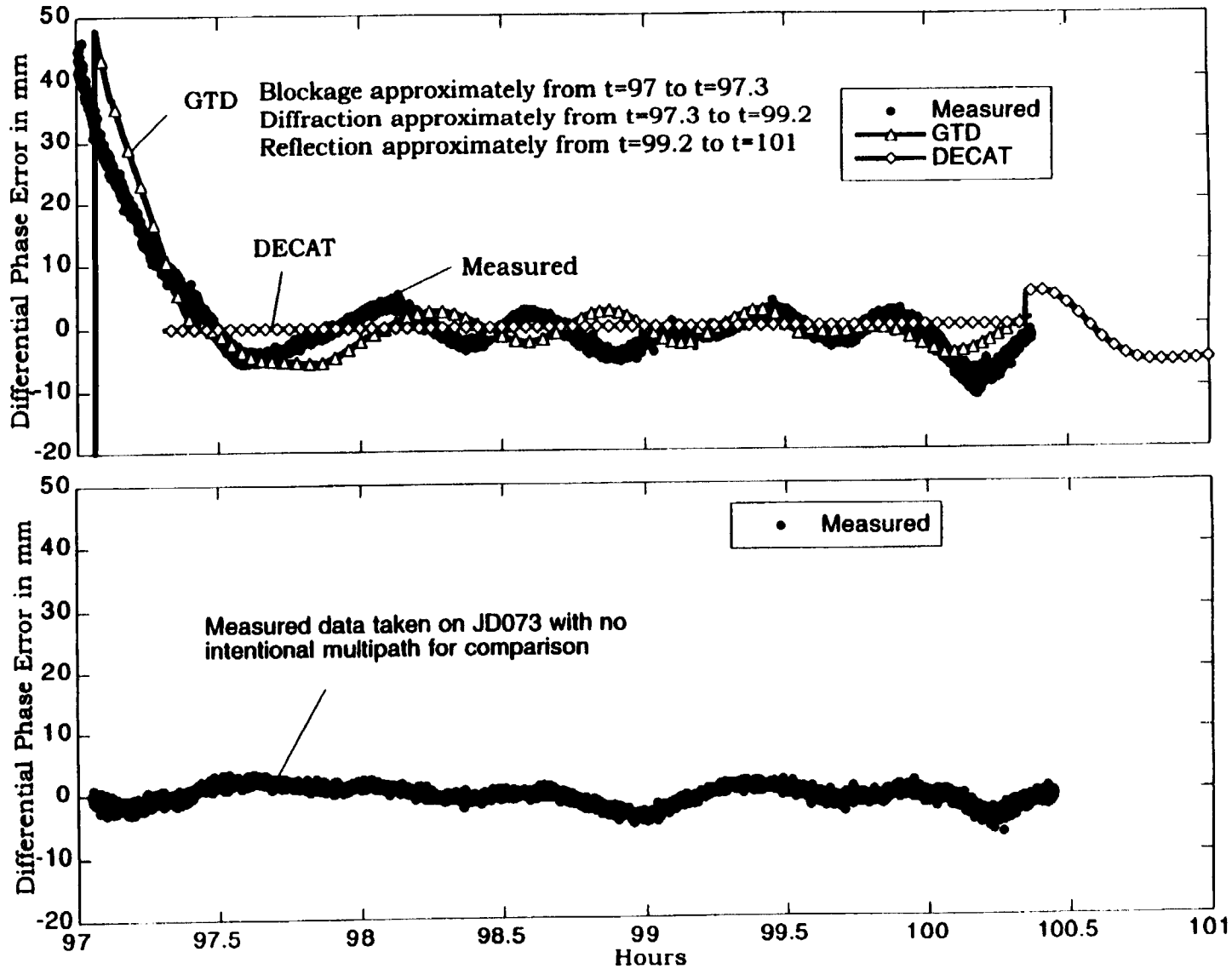

Figure 7.4.9 - Comparison of measured and predicted differential phase errors for 3-ft-diameter cylinder with choke ring antennas (JD074) - satellite 24, antenna 1.

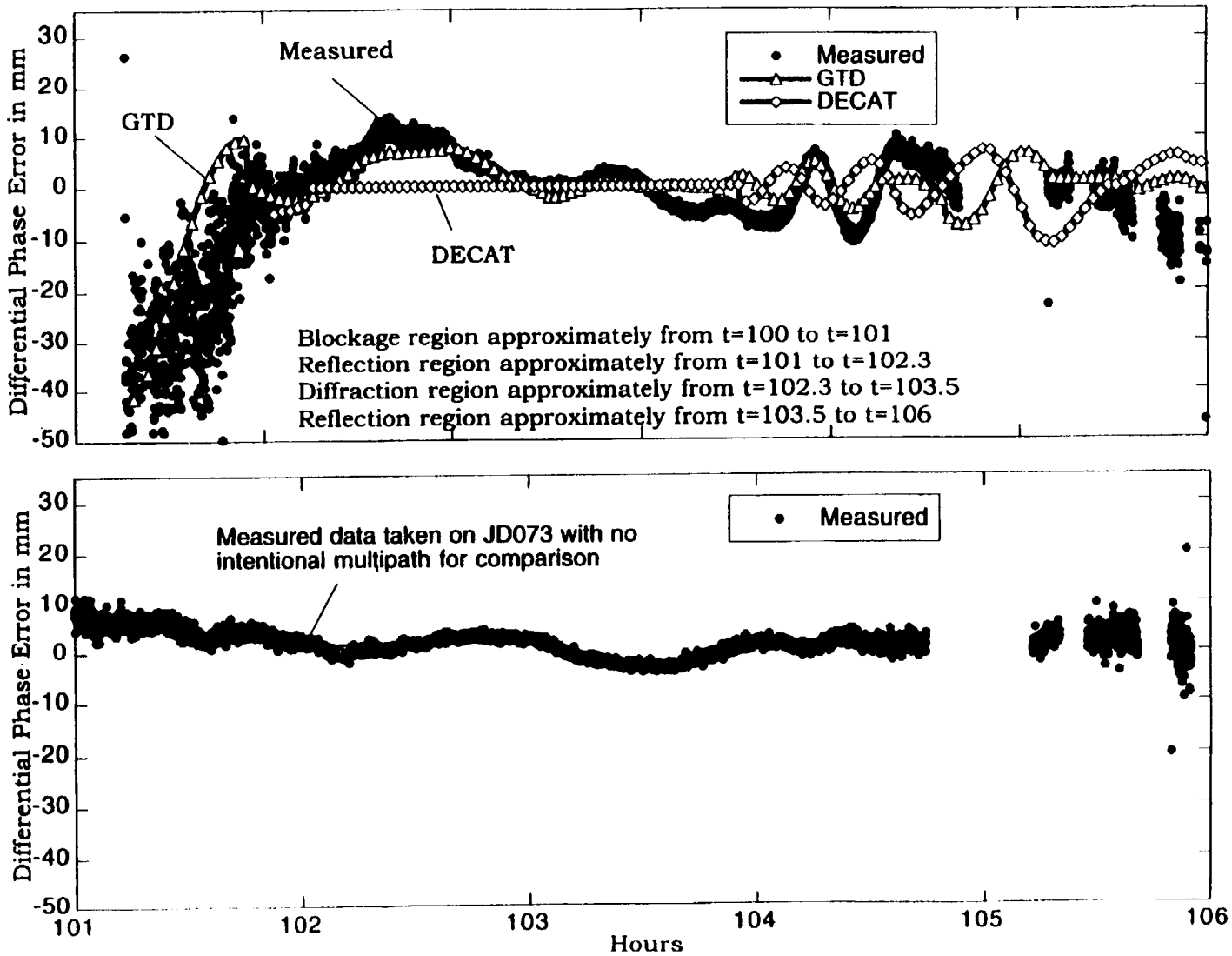

Figure 7.4.10 - Comparison of measured and predicted differential phase errors for 3-ft-diameter cylinder with choke ring antennas (JD074) - satellite 26, antenna 1.

7.5 Comparison of Field Data, GTD Data, and DECAT Data for JD079 With 9-in.-Diameter Cylinder and Choke Ring Antennas

For JD079, the 9-in.-diameter cylinder was placed on the South side of the antenna array and was tilted 45° as shown in Appendix A. The satellite tracks for JD079 are shown in Figure 7.5.1.

Figure 7.5.2 shows the comparison between the field data, GTD data, and DECAT data for satellite 17. Satellite 17's ground track passes through the diffraction and reflection regions There is a noticeable multipath trace in the measured data in the reflection region, but GTD doesn't match the data as well for this case as it did for the 3-ft-diameter cylinder. GTD calculations begin to become inaccurate when the size of the multipath object approaches the size of the wavelength. The 9-in.-diameter cylinder is close in diameter to the approximately 7.5-in. GPS carrier phase wavelength. DECAT calculated only small phase changes in the reflection region.

Figures 7.5.3 and 7.5.4 show the comparison data for satellites 18 and 23. Both satellites' ground tracks are predominantly in the diffraction region and DECAT calculated all zeroes. There is not much noticeable multipath in the measured data for either case.

Figures 7.5.5 and 7.5.6 show the comparison data for satellites 26 and 31. Both satellites' ground tracks are in the reflection and diffraction regions. DECAT calculated almost all zeroes even in the reflection regions due to the modeling of the cylinder as a collection of polygons. There is a noticeable multipath trace in the measured data, and GTD matches the measured data well in both cases.

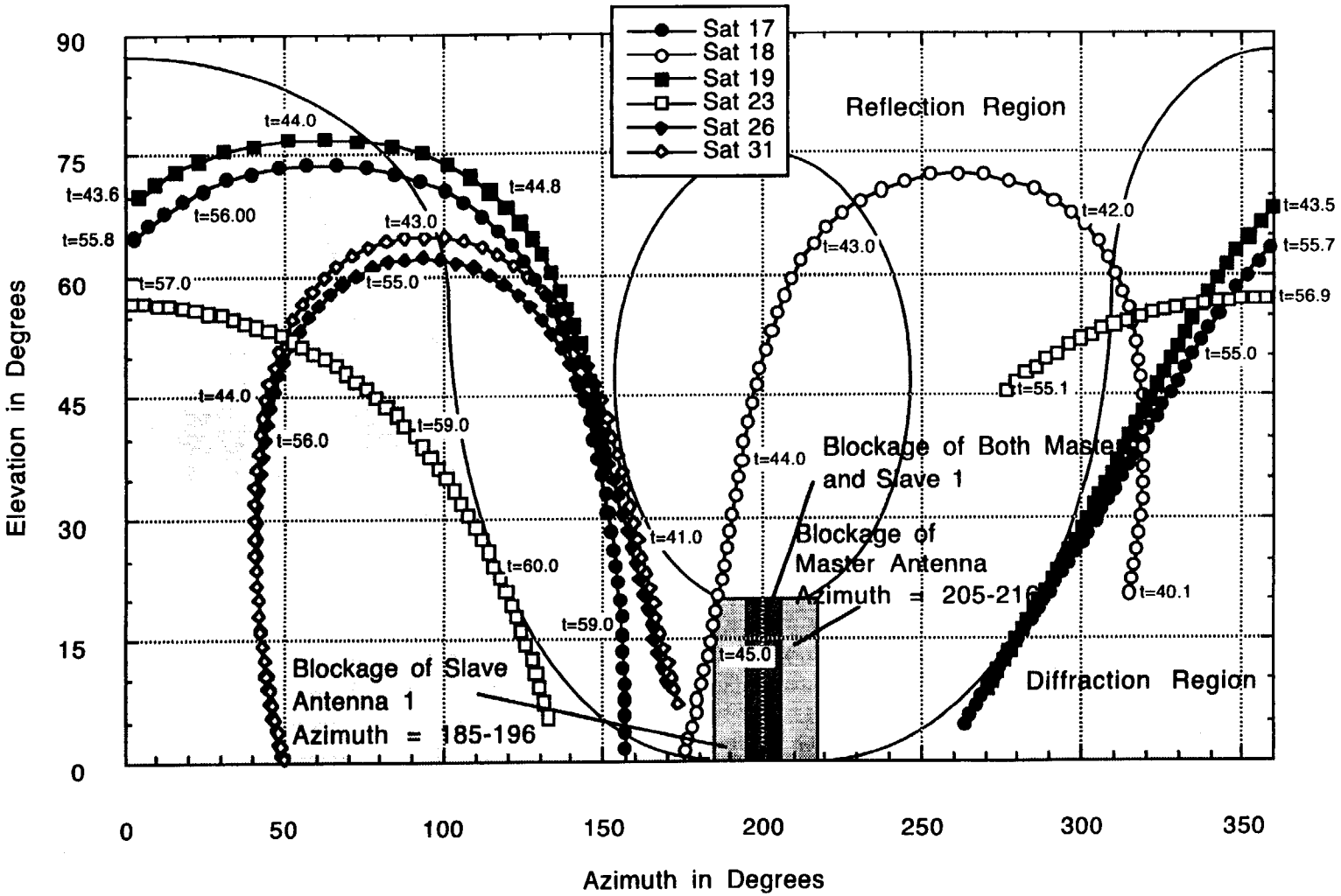

Figure 7.5.1 - Satellite tracks for JD079 with 3-in.-diameter cylinder and choke ring antennas.

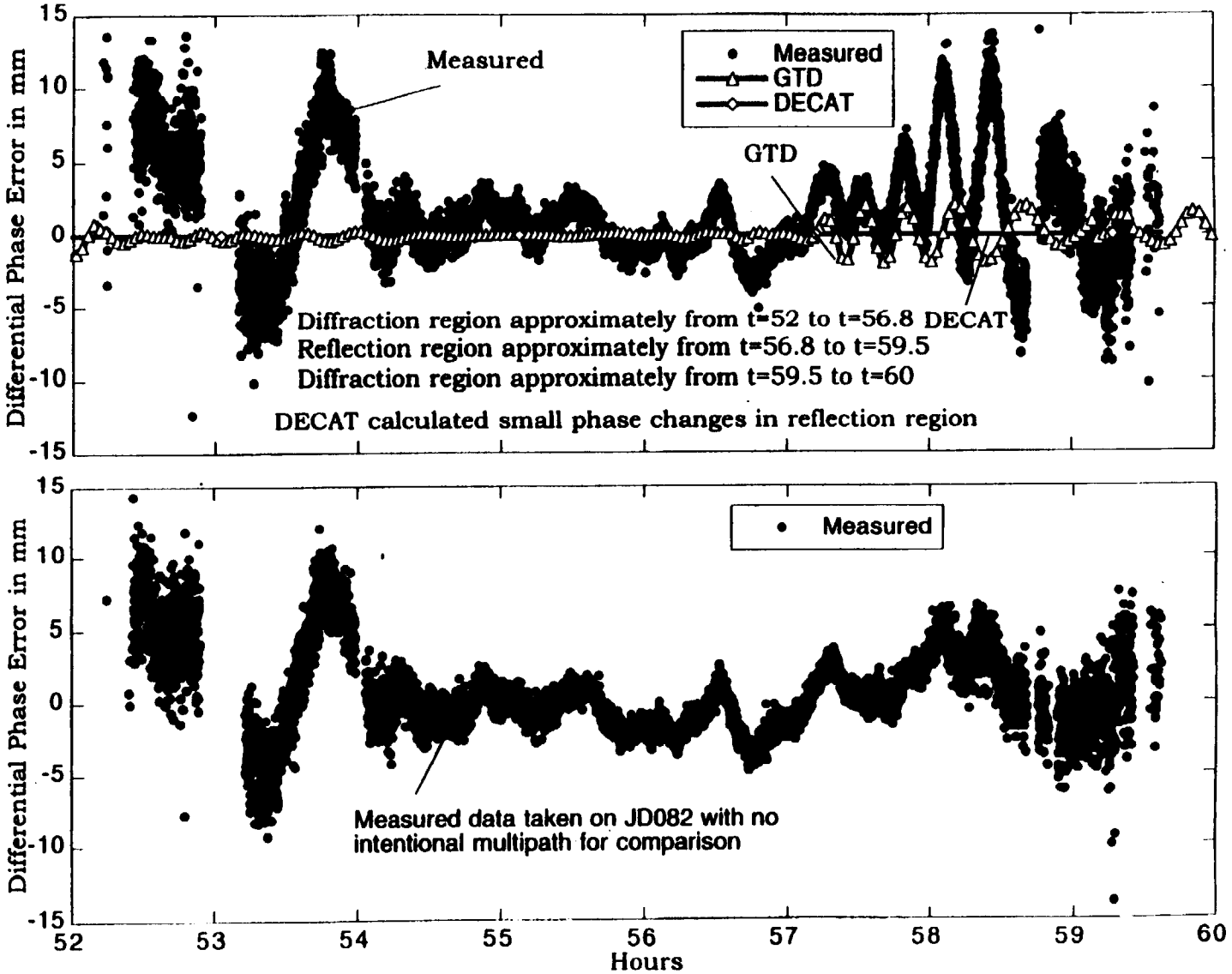

Figure 7.5.2 - Comparison of measured and predicted differential phase errors for 9-in.-diameter cylinder with choke ring antennas (JD079) - satellite 17, antenna 1.

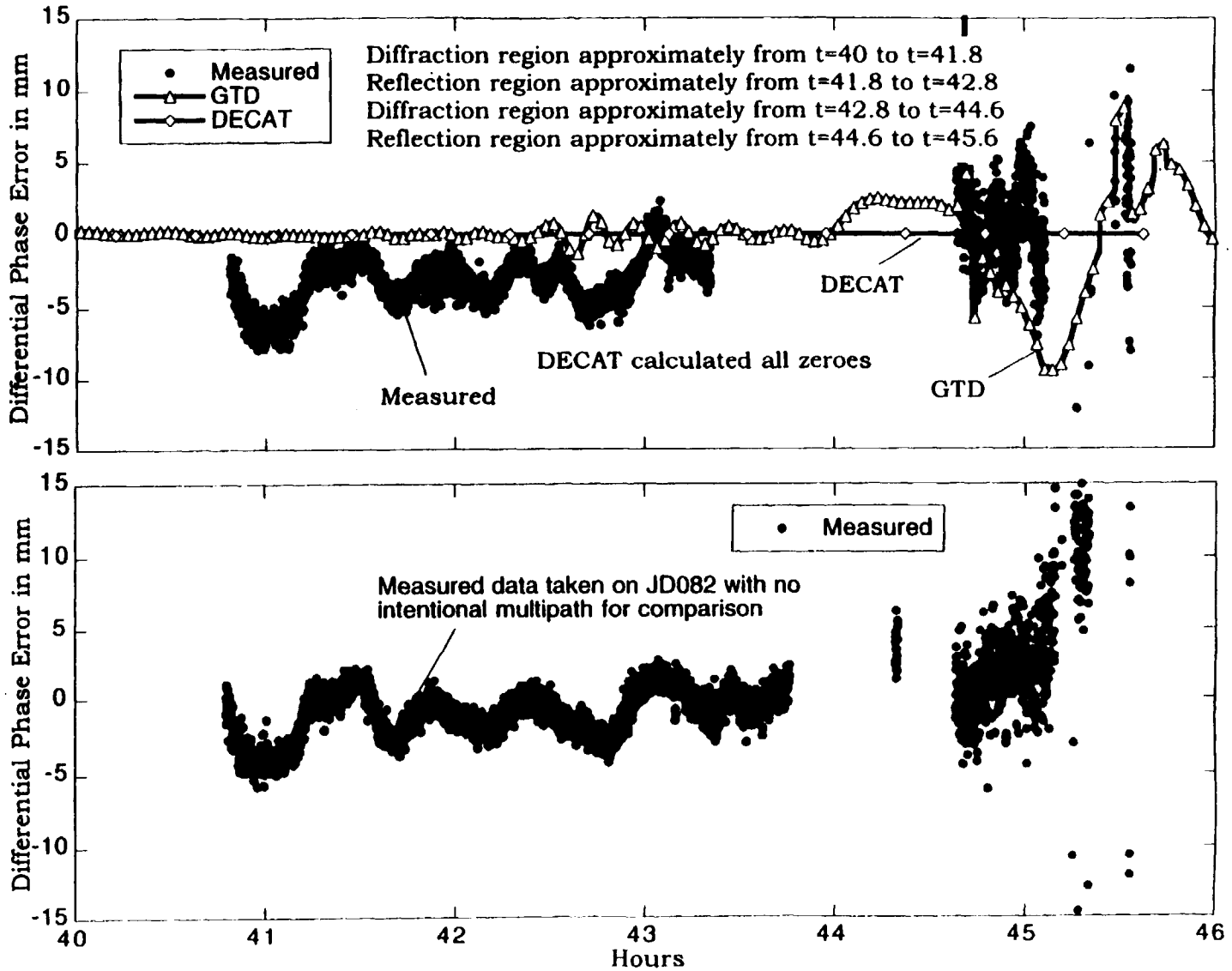

Figure 7.5.3 - Comparison of measured and predicted differential phase errors for 9-in.-diameter cylinder with choke ring antennas (JD079) - satellite 18, antenna 1.

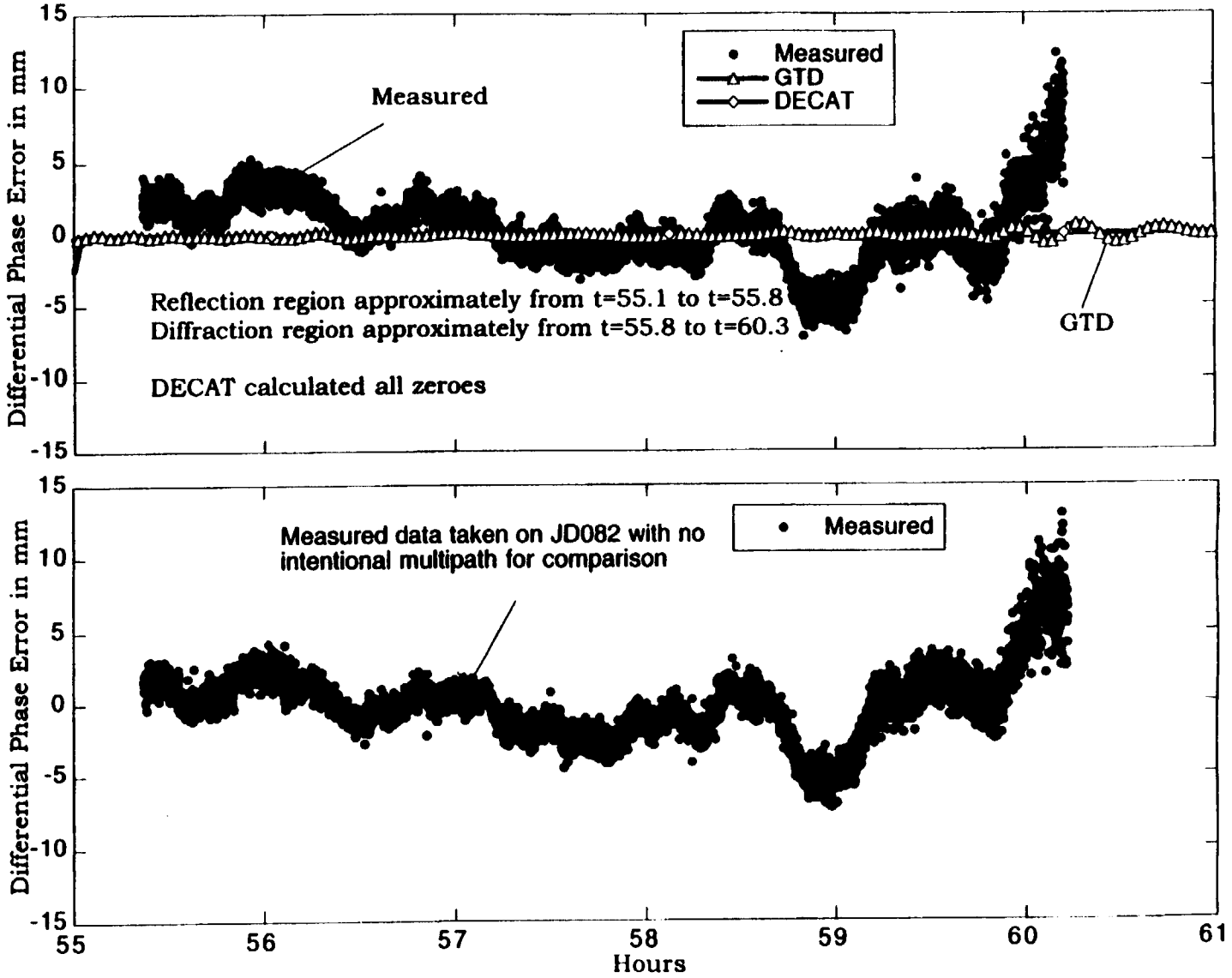

Figure 7.5.4 - Comparison of measured and predicted differential phase errors for 9-in.-diameter cylinder with choke ring antennas (JD079) - satellite 23, antenna 1.

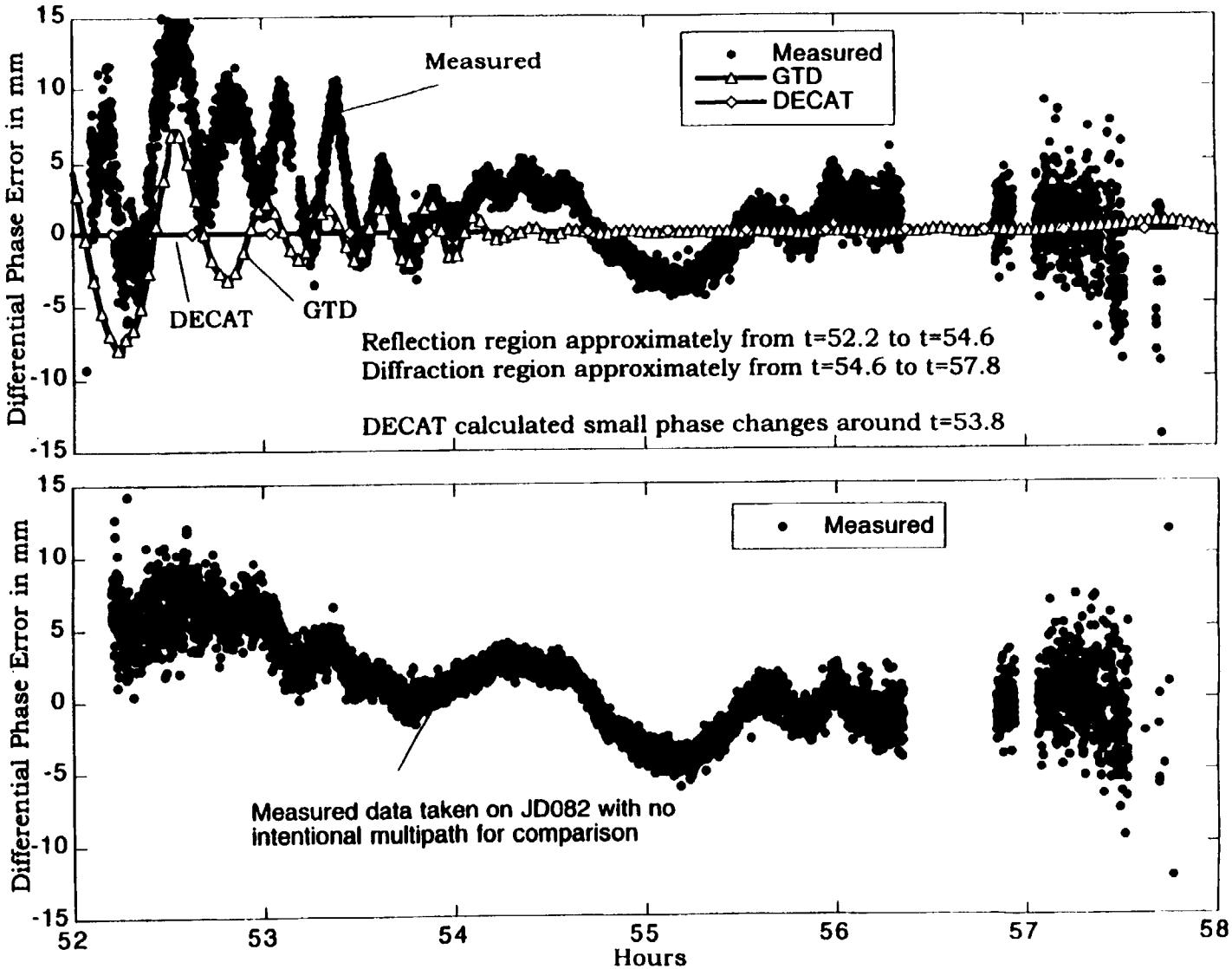

Figure 7.5.5 - Comparison of measured and predicted differential phase errors for 9-in.-diameter cylinder with choke ring antennas (JD079) - satellite 26, antenna 1.

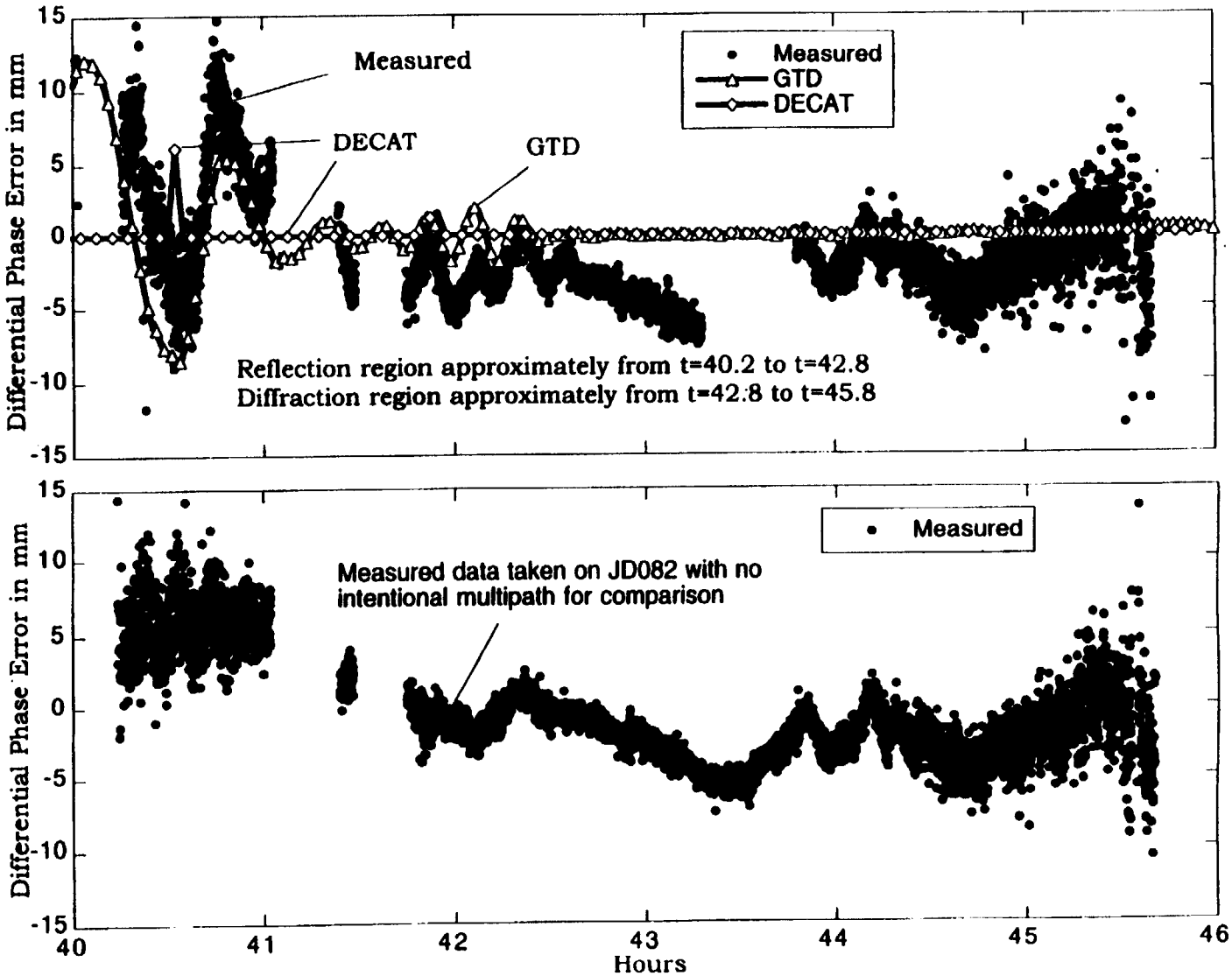

Figure 7.5.6 - Comparison of measured and predicted differential phase errors for 9-in.-diameter cylinder with choke ring antennas (JD079) - satellite 31, antenna 1.

7.6 Comparison of Field Data, GTD Data, and DECAT Data for JD075 With Box and Choke Ring Antennas

For JD075, the 40-in. by 15-in. by 28-in. box was placed on the South side of the antenna array on the ground plane as shown in Appendix A. The satellite tracks for JD075 are shown in Figure 7.6.1. Notice that the reflection region is very small and only satellite 26 passes through the reflection region at all. Therefore, as expected, DECAT did not match this data very well.

Figure 7.6.2 shows the comparison between the field data, GTD data, and DECAT data for satellite 16. Satellite 16's ground track passes through the blockage and diffraction regions. GTD and DECAT both seem to match the differential phase errors in magnitude but not in phase. However, the measured data taken with no intentional multipath producer is noisy in the lower elevation reflection region, making it difficult to see the multipath trace in the measured data.

Figure 7.6.3 shows the comparison data for satellite 17. Satellite 17's ground track passes through the blockage and diffraction regions. There is noticeable multipath in the measured data near GPS time 125 that neither GTD nor DECAT matches very well. Also, GTD calculates a more noticeable differential phase error trace in the blockage region than is evident in the measured data.

Figure 7.6.4 shows the comparison data for satellite 26. Satellite 26's ground track passes through the blockage, reflection, and diffraction regions. There are significant differential phase errors, about 40 mm, in the measured data in the blockage region and GTD matches it quite well in this case.

Figures 7.6.5 and 7.6.6 show similar results for satellites 27 and 31.

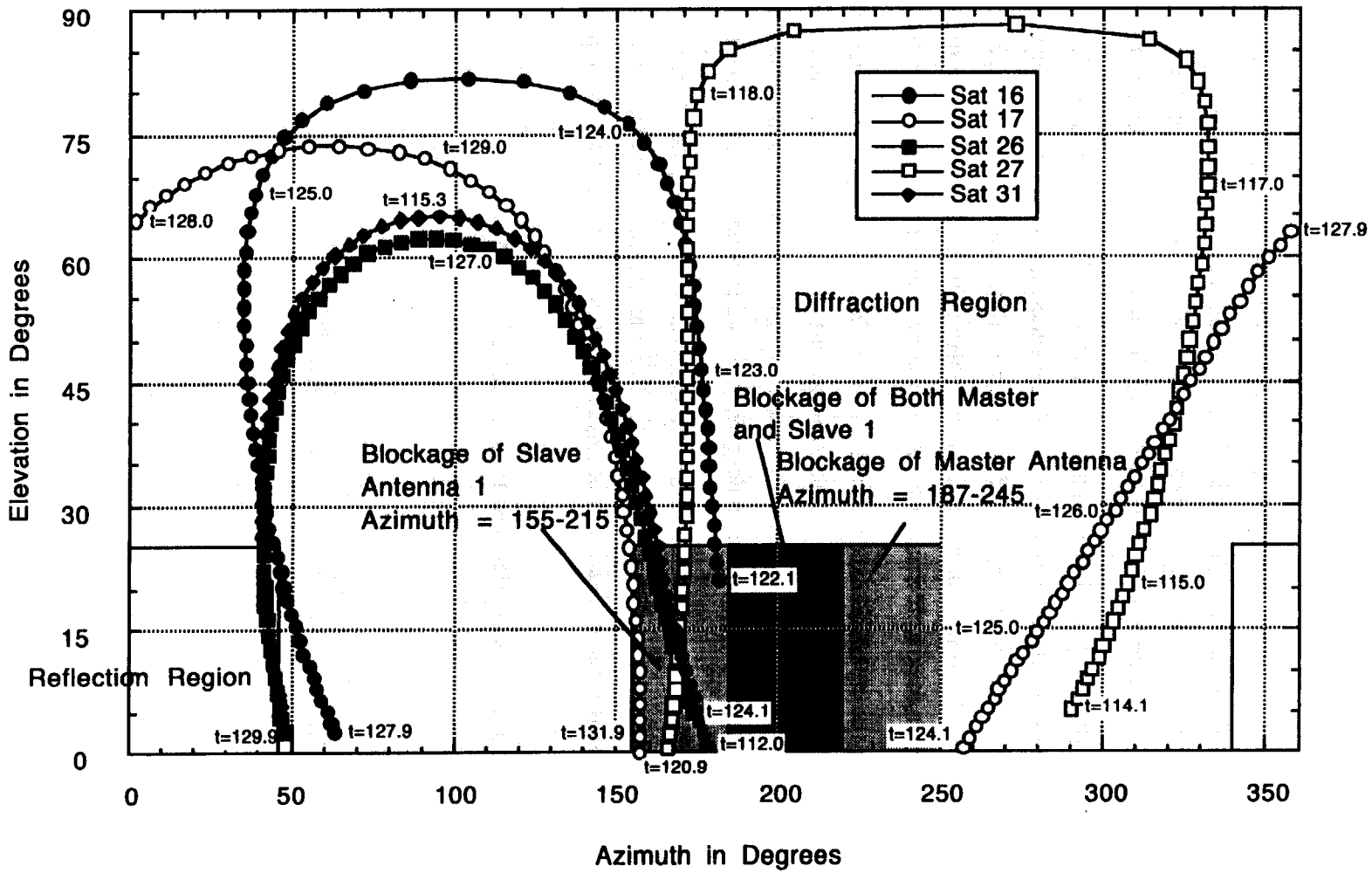

Figure 7.6.1 - Satellite tracks for JD075 with box and choke ring antennas.

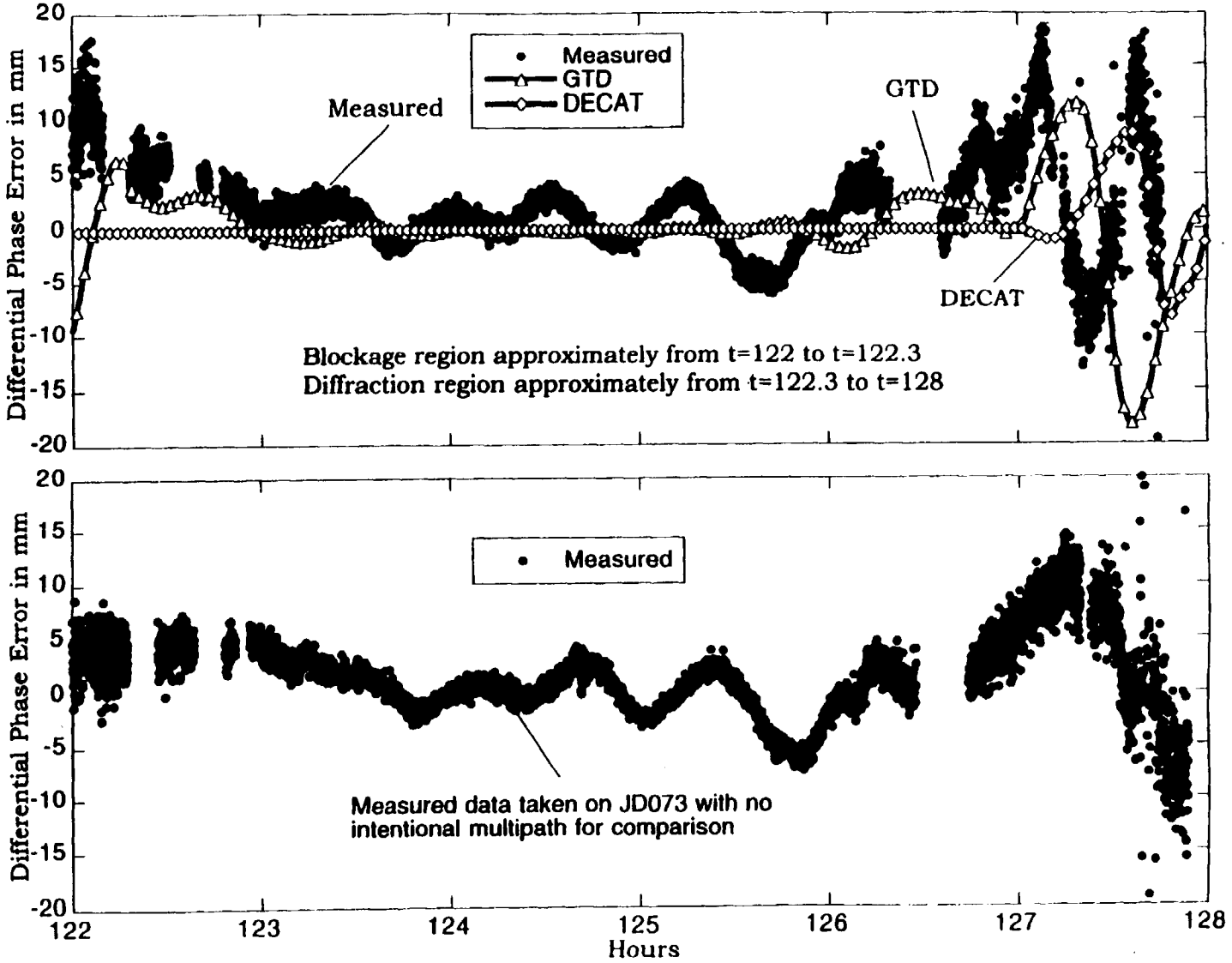

Figure 7.6.2 - Comparison of measured and predicted differential phase errors for box with choke ring antenna (JD075) - satellite 16, antenna 1.

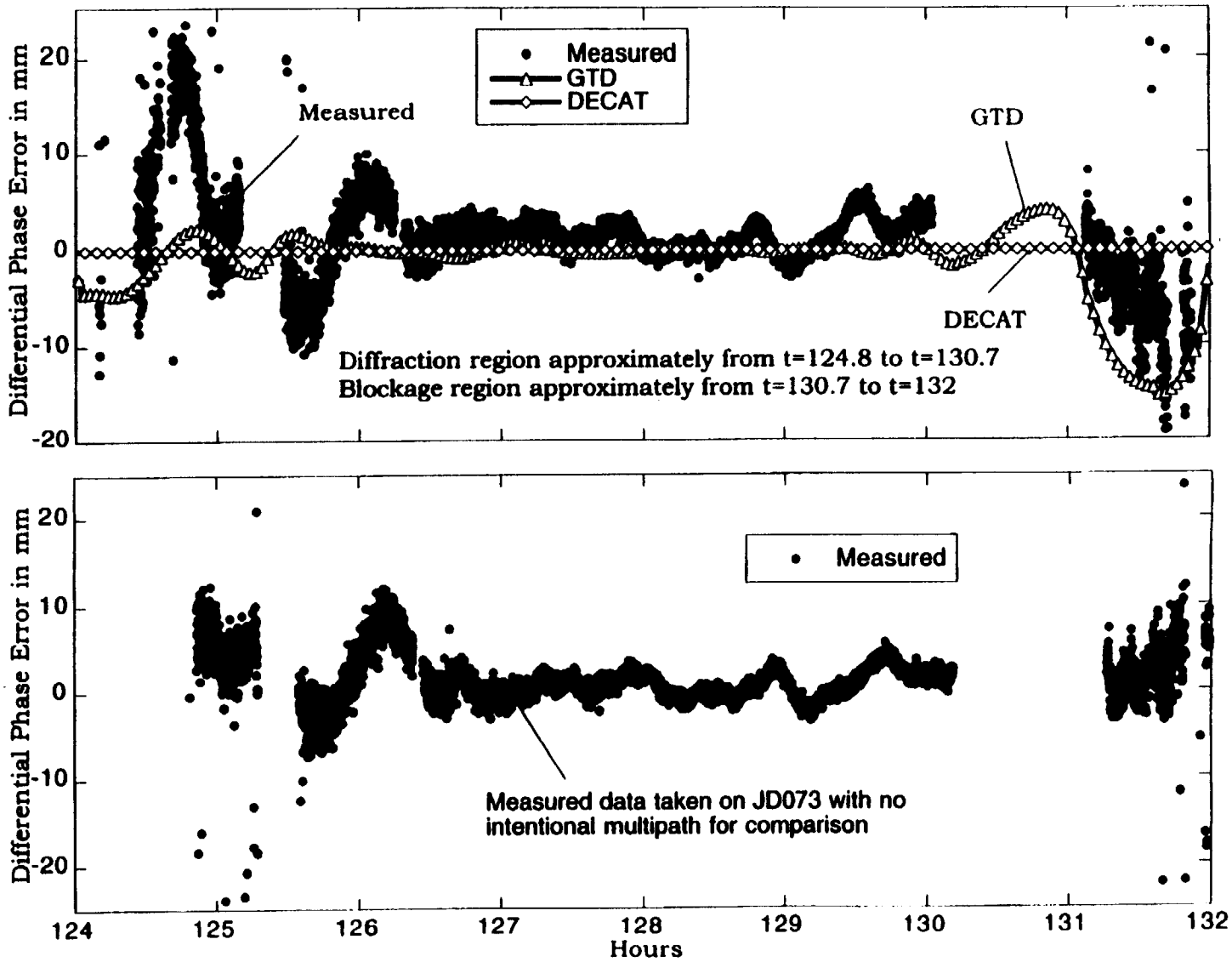

Figure 7.6.3 - Comparison of measured and predicted differential phase errors for box with choke ring antenna (JD075) - satellite 17, antenna 1

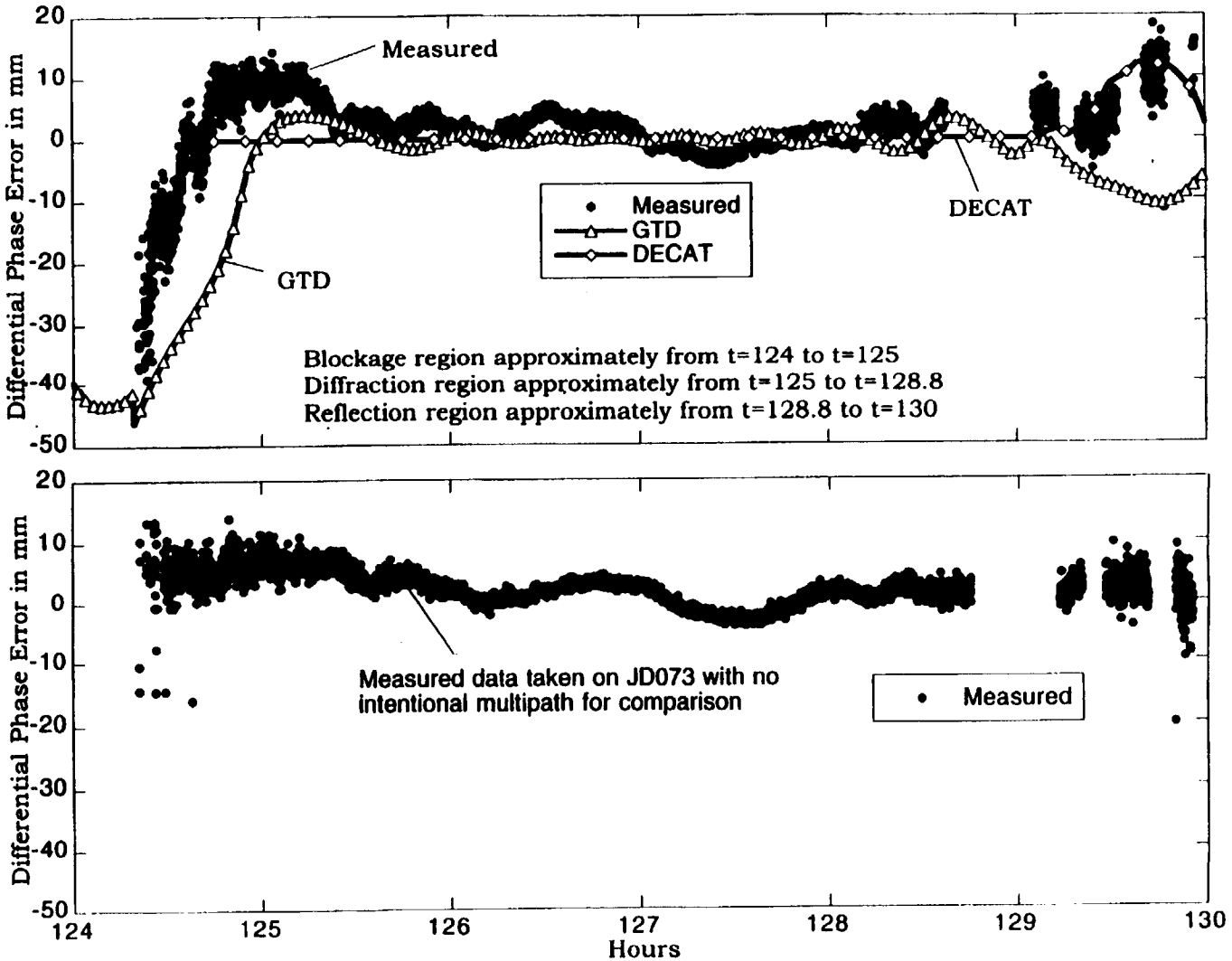

Figure 7.6.4 - Comparison of measured and predicted differential phase errors for box with choke ring antenna (JD075) - satellite 26, antenna 1.

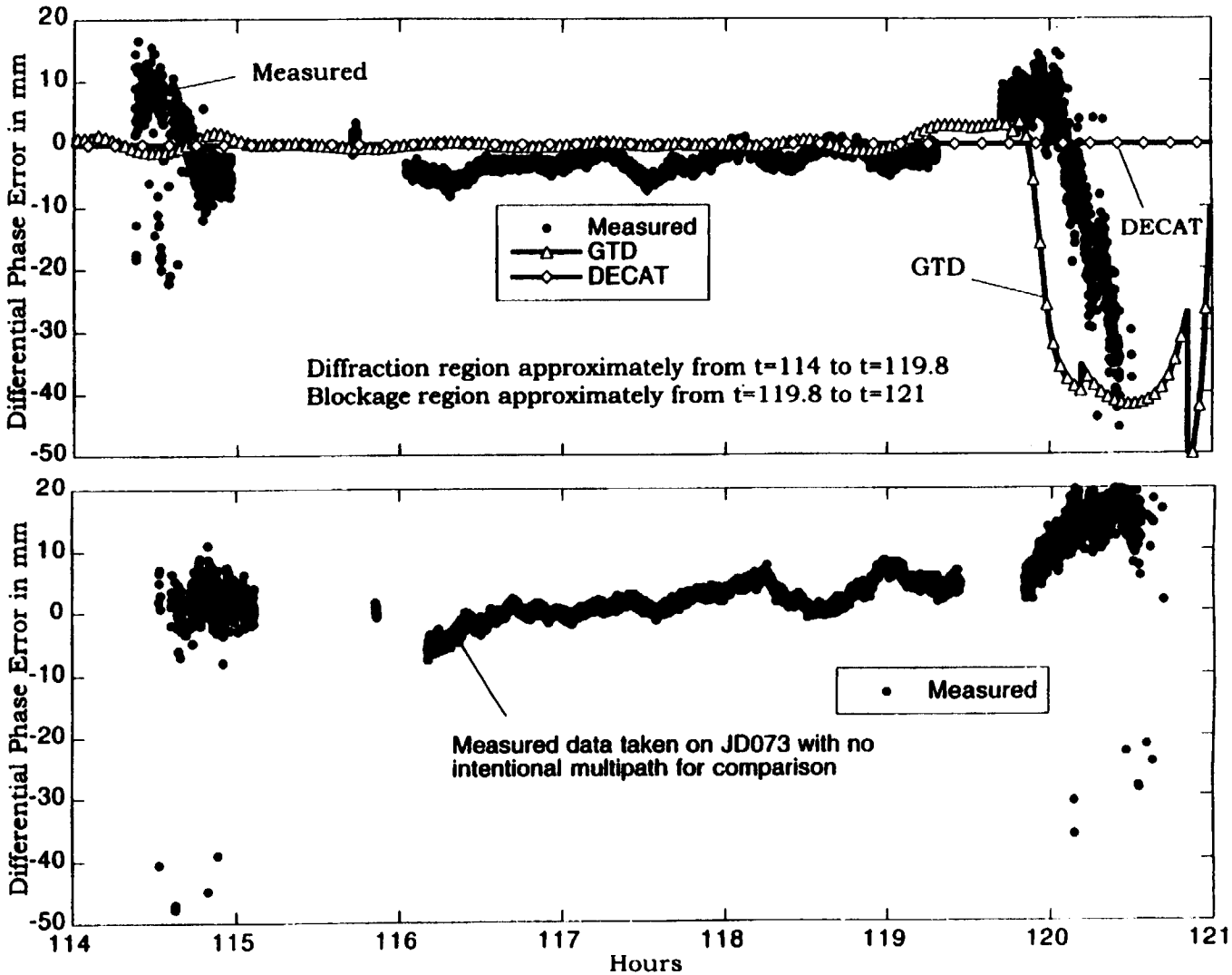

Figure 7.6.5 - Comparison of measured and predicted differential phase errors for box with choke ring antenna (JD075) - satellite 27, antenna 1.

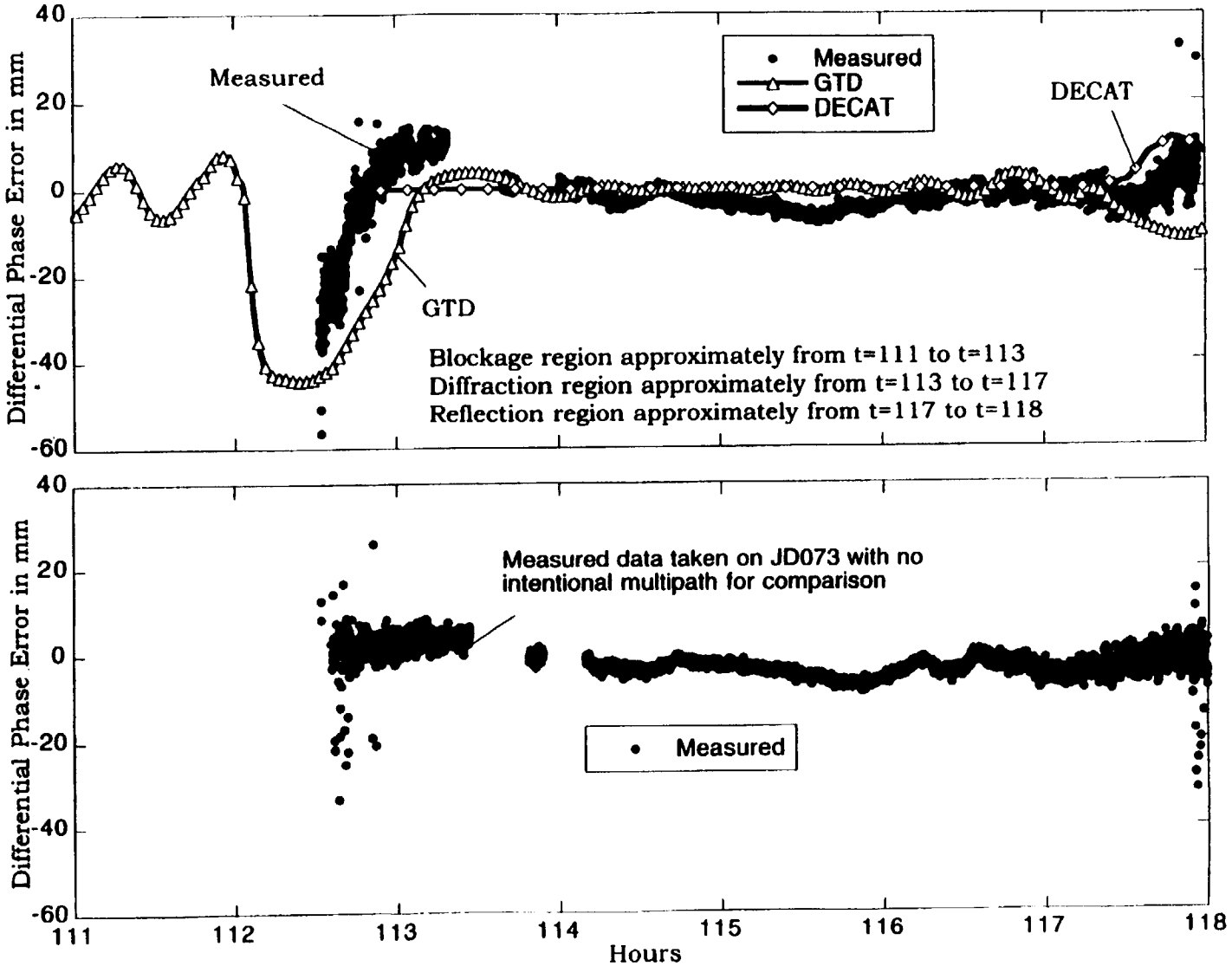

Figure 7.6.6 - Comparison of measured and predicted differential phase errors for box with choke ring antenna (JD075) - satellite 31, antenna 1.

8 Link Margin Calculations

A link margin calculation provides an end-to-end description of the signal power in a communications link by summing all the gains and losses that affect the signal between the transmitter and the receiver. The link margin also contains calculations of the power received at the input to the receiver, the noise received at the input to the receiver, the SNR ratio, and the difference between the received SNR and the required SNR. If the received SNR is higher than the required SNR, sufficient power is received at the receiver to meet performance specifications, and the margin is positive. However, if the received SNR is lower than the required SNR, insufficient power is received at the receiver to meet its performance specifications, and the margin is negative. Thus, the link margin can be used to predict system performance and where the link will degrade and fail to perform.

A link margin calculation has been performed for the GPS multipath field test. The following sections document the system parameters used in the link margin calculation, the calculation itself, a comparison with the measured SNR data, and conclusions that may be drawn about the ISS link margin calculations from these results.

8.1 Parameters

The signal power leaving the transmitting antenna is characterized by its effective isotropic radiated power (EIRP). This value has been back-calculated for the GPS L1 C/A code from the guaranteed received signal power in ICD-GPS-200 (Ref. 7), as illustrated in Table 8.1.1 (Ref. 8).

Table 8.1.1 - GPS L1 EIRP Calculation

Parameter	Value	Remarks
GPS minimum EIRP, dBW	27.0	Estimate to comply with L1 C/A Code minimum received power spec
Space loss, dB	-184.4	Maximum slant range, 5° elevation angle: 25283 km
		ICD-GPS-200, p. 11
		GPS L1 carrier frequency: 1575.42 MHz
		ICD-GPS-200, p. 10
Atmospheric attenuation,dB	-2.0	Atmospheric Attenuation Spec
		ICD-GPS-200, p. 42
Pointing loss, dB	0.0	14.3° off GPS antenna boresight
		13.8° for Earth limb plus 0.5° GPS pointing error
		ICD-GPS-200, p. 42
Polarization loss, dB	-3.6	Transmit Axial Ratio: R1 = 1.148 (1.2 dB)
		ICD-GPS-200, p. 14
		Estimated Linearly Polarized User Axial Ratio: R2 = 316 (50 dB)
		ICD-GPS-200, p. 42
Receive antenna gain, dB	3.0	Antenna Spec for Minimum Received Power
		ICD-GPS-200, p. 11
Minimum Received Power,dBW	-160.0	L1 C/A Code Minimum Received Power Spec
		ICD-GPS-200, Table 3-III, p. 13
		1 + 2 + 3 + 4 + 5 + 6

All the parameters in this calculation are specified in ICD-GPS-200 except for the axial ratio of the linearly polarized antenna. If the estimated axial ratio is too conservative (too high), the actual polarization loss would be less, and the required EIRP would be lower (e.g., if the axial ratio were 10 dB, the polarization loss would be -1.4 dB, and the required EIRP would be 25.6 dBW). However, the guaranteed received power is a minimum value; the actual received power would probably be higher than the guaranteed.

As a signal travels through space, it experiences a loss which depends upon the slant range between the transmitter and the receiver and the frequency of the signal, as

$$Ls=-92.442-20log(D*fc)$$

where

Ls is the space loss in dB

D is the slant range in km

fc is the carrier frequency in GHz.

The range is a function of the elevation angle of the GPS Space Vehicle (SV) relative to the receiver; Table 8.1.2 lists several elevation angles and the associated slant ranges and space losses.

Table 8.1.2 - Gains and Ranges Associated With Three Elevation Angles

Elevation Angle, degrees above horizon	80	60	40
Receive Antenna Gain, dB	6.8	5.0	0.9
Slant Range, km	20305	20894	22057
Space Loss, dB	-182.5	-182.8	-183.3

Since the GPS multipath field test antennas are located on the ground, they are within the main beamwidth of the GPS SV antennas. Since the field test antennas' boresights are pointed up, the GPS SVs are within their main beamwidth. With both antennas within the other's main beamwidth, the pointing loss can be assumed to be 0 dB.

The GPS SV antennas are assumed to be RHCP with an axial ratio of 1.2 dB; the GPS multipath field test antennas are assumed to be RHCP with an axial ratio of 3.0 dB. Assuming a worst-case mismatch of 90°, the formula

$$Lp=10\log\left\{0.5+\frac{2R_1R_2+0.5(1-R_1^2)(1-R_2^2)\cos 2\phi}{(1+R_1^2)(1+R_2^2)}\right\}$$

where

Lp is the polarization loss

$R1 = 10^{R1dB/20}$ is the transmitting antenna axial ratio

$R2 = 10^{R2dB/20}$ is the receiving antenna axial ratio

and ϕ is the mismatch

gives a polarization loss of 0.2 dB.

Figure 8.1.1 illustrates the worst-case envelope of the MicroPulse L1/L2 choke ring antenna pattern that was used to model the choke ring antennas.

The system configuration is illustrated in Figure 8.1.2. The antenna was connected to a Trimble preamplifier through two right angle connectors, which are assumed to have 0.2 dB of loss each. The preamplifier can be specified by its gain and noise figure. The preamplifier has a minimum gain of 42 dB, a typical gain of 46 dB, a typical noise figure of 2.8 dB, and a maximum noise figure of 3.2 dB. The typical values were used for both the gain and the noise figure. The preamplifier was connected to the receiver through two connectors and 14 feet of RG142 cable, which, combined, were assumed to have a 2.6 dB loss.

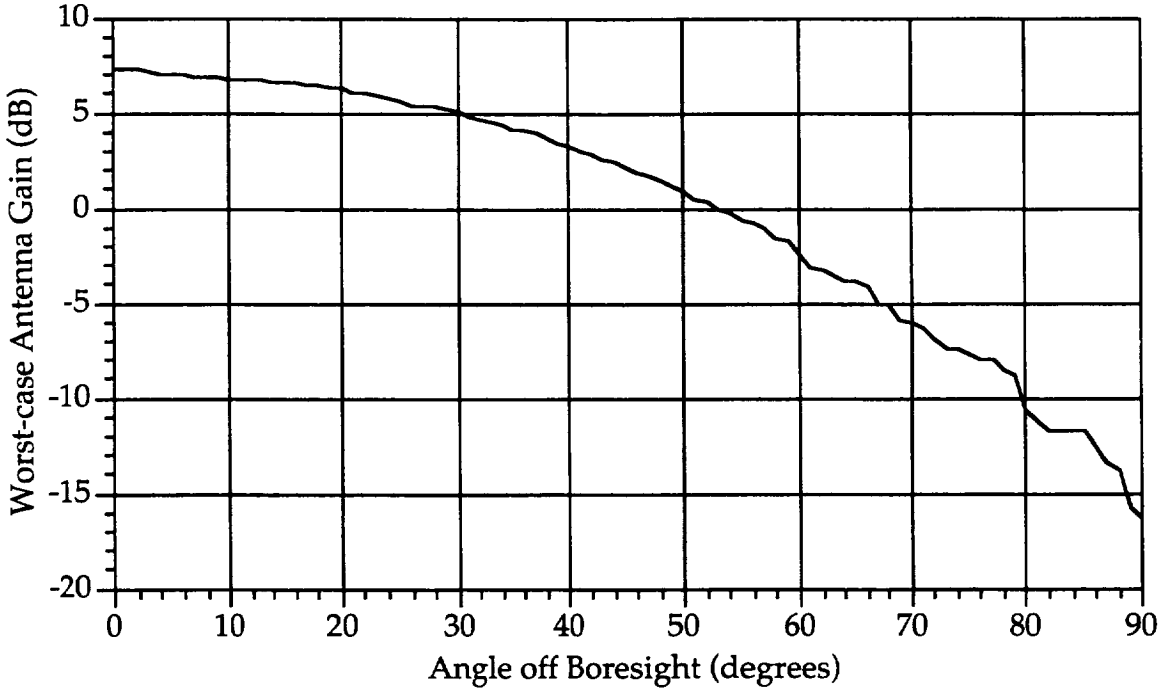

Figure 8.1.1 - Antenna gain vs. angle off boresight.

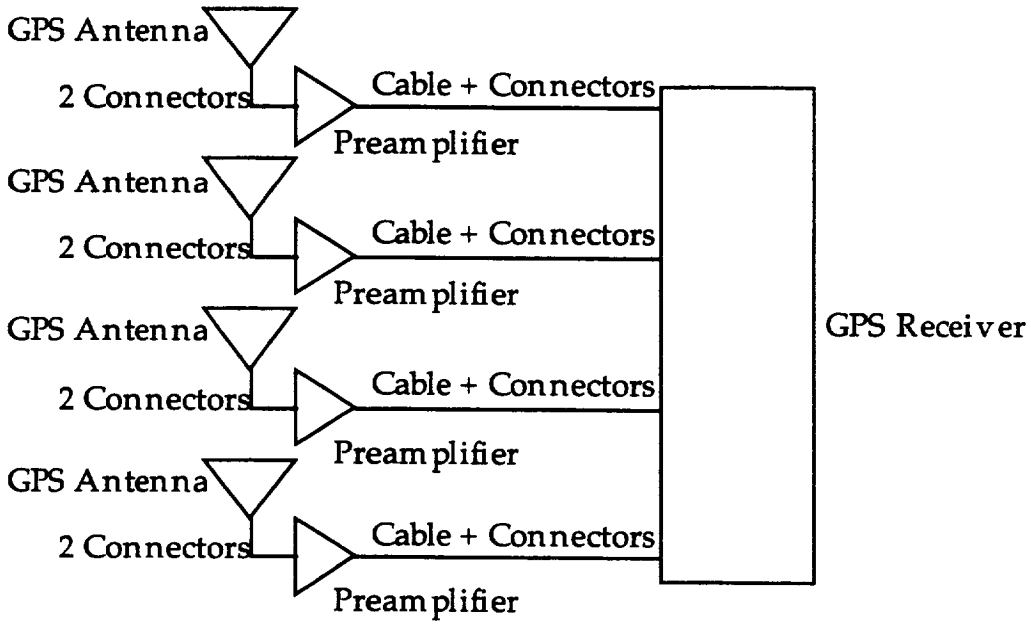

Figure 8.1.2 - System configuration

The receiver may be characterized by its noise figure and SNR threshold. Because the preamplifier has a large gain, the receiver noise figure is not a significant contributor to the system noise; a noise figure of 6 dB was assumed. The receiver SNR threshold for the Quadrex receiver was measured to be 4 antenna measurement units (AMUs) (Ref. 9). The SNR in AMUs may be converted to a C/No in dBHz using the following formula

$$C/No = 27 + 20\log_{10}(SNR[AMUs])$$

which gives a C/No threshold of 39 dBHz given a SNR of 4 AMUs.

8.2 Circuit Margin Compared to Measured Data

The GPS multipath field test link margin calculation is tabulated in Table 8.2.1 for three different elevation angles. The link margin ranges from 8.4 to 15 dB, which is more than enough power to close the link.

Table 8.2.1 - GPS Multipath Field Test Link Margin Calculation

Parameters	Values			Remarks
Elevation Angle, degrees above horizon	80.0	60.0	40.0	Vary Elevation Angle
Receive Antenna Gain, dB	6.8	5.0	0.9	Choke Ring Antenna - gain varies with angle
Slant Range, km	20305	20894	22057	Varies with elevation angle
Transmit EIRP, dBW	27.0	27.0	27.0	Derived GPS Spec
Space loss, dB	-182.5	-182.8	-183.3	Slant Range from (3)
				GPS L1 carrier freq: 1575.42 MHz
Transmit pointing loss differential, dB	0.0	0.0	0.0	
Polarization loss, dB (worst case)	-0.2	-0.2	-0.2	TRX axial ratio: R1=1.148 (1.2 dB)
				RCVR axial ratio: R2=1.413 (3.0 dB)
Receive antenna gain, dB	6.8	5.0	0.9	Choke Ring Antenna
Receive circuit gain, dB	43.0	43.0	43.0	Antenna to preamp Circuit Loss: 0.4 dB
				Preamp Gain: 46.0 dB
				Preamp to Receiver Circuit Loss: 2.6 dB
Total receive power (P_{rec}), dBW	-106.0	-108.0	-112.6	(4) + (5) + (6) + (7) + (8) + (9)
System noise temp, dBK	68.6	68.6	68.6	GPS receiver noise figure: 6.0 dB
				Preamplifier noise figure: 2.8 dB
				Composite noise figure: 3.2 dB
				Antenna noise temp: 50.0 °K
Receiver G/T, dB/K	-18.8	-20.6	-24.7	(8) + (9) - (11)
Boltzmann's Constant, dBW/°K-Hz	-228.6	-228.6	-228.6	1.38e-23 W/°K-Hz
Noise Spectral density (No), dBW/Hz	-160.0	-160.0	-160.0	(11) + (13)
C/No, dBHz	54.0	52.0	47.4	(10) - (14)
C/No Threshold, dBHz	39.0	39.0	39.0	Measured Quadrex SNR threshold
Link Margin, dB	15.0	13.0	8.4	(15) - (17)
Max Measured Received AMUs	26.0	27.0	17.0	
Max Measured Received C/No	55.3	55.6	51.6	AMUs from (18)
C/No Difference, dB	-1.3	-3.6	-4.2	(15) - (19)
Min Measured Received AMUs	20.5	19.0	12.5	Measured Data - JD073
Min Measured Received C/No	53.2	52.6	48.9	AMUs from (21)
C/No Difference, dB	0.8	-0.6	-1.6	(15) - (22)

The SNRs in AMUs from seven satellites (5, 6, 7, 16, 22, 24, and 27) for JD073 were correlated with the elevation angle for that satellite. All the data for three elevation angles (80°, 60°, and 40°) was collected for each satellite, and the maximum SNR and minimum SNR for each elevation angle for all the satellites were determined. The maximum and minimum measured SNR in AMUs for each elevation angle were converted to a C/No in dBHz, and the result was compared to the C/No calculated in the link margin. The link margin C/No ranged from 0.8 dB more to 1.6 dB less than the minimum measured C/No and from 1.3 to 4.2 dB less than the maximum measured C/No. Thus, the link margin SNR calculations were -0.8 to 4.2 dB more conservative than the measured values.

These link margins were performed using "typical" values for the components, and the results were -0.8 to 4.2 dB conservative as compared to the measured values. However, link margins are usually performed for a "worst case" scenario since, if the system has a positive margin in the worst case, it will have a positive margin for any case. Since the values used in the ISS GPS link margins are based on the same assumptions as the margins performed here, the margins for the ISS GPS subsystem should also be conservative.

9 Conclusions

It was demonstrated that the phase errors due to multipath in the precision GPS applications can be modeled and characterized using the GTD technique and characterized to a lesser fidelity using the DECAT technique. Both the GTD and DECAT calculations matched the data well for the flat plate in the reflection region. GTD matches the data well for the flat plate and box in the reflection, diffraction, and blockage regions well for the flat plate and the box. However, DECAT didn't match the data taken with the box very well because most of that data was in the diffraction region. Also, DECAT didn't match the cylinder data very well, because the cylinders produced a lot of diffractions and DECAT modeled the cylinders as a collection of polygons. GTD matched the data taken with the large cylinder very well, and the data taken with the 9-in. diameter fairly well. GTD matched the 9-in.-cylinder data better than expected since the theory behind GTD breaks down when the reflective object is about the size of a wavelength.

The multipath objects introduced more than 10 mm, and as high as 95 mm, of phase shift in the data. This level of phase shift can produce significant errors in the attitude determination solution. This level of multipath error has been observed in the GTD calculations of the ISS environment (Ref. 10), and analysis performed using the GTD data has shown that the ISS's attitude determination performance requirement will still be met (Ref. 11). It should also be noted that the field test configuration was meant to simulate typical ISS structures, such as flat plates, cylinders, and boxes, but the two environments are not identical. For example, the ISS does not have a

3-ft-diameter, 4-ft-tall cylinder within two feet of the GPS antennas, which was the case for the field test. Therefore, the phase errors observed in the field test are different from the ISS's.

It was also noted from the measured results when no multipath producer was present that there were significant phase errors in the low elevation regions. These phase errors were either due to antenna phase center deviation in that region, background multipath, or the GPS receiver. The authors do not suspect the phase errors are due to the background because the 12-ft by 12-ft ground plane should prevent most background signals from entering the antennas, and when the background environment was modeled in the GTD simulation, the phase errors were negligibly small. Therefore, the phase center variations at lower elevations are most likely due to antenna phase center deviation. This presents a challenging task for the GPS antenna design to provide better phase center stability to minimize this error.

10 Acknowledgments

The authors would like to acknowledge Don Eggers and Tom Goodwin, who constructed the field test objects and the table to support them. The authors would also like to acknowledge Jose Hernandez for making some of the drawings of the field test setup.

11 References

1. Bond, Victor, "Precessional, Nutational, and Earth Rotational Transformations Based on Standard Epoch of J2000," JSC-22535, 1987.

2. Bond, Victor, "The Transformation From WGS84 to J2000," JSC-24045, 1989.

3. Schupler, Bruce R., Roger L. Allshouse, and Thomas A. Clark, "Signal Characteristics of GPS User Antennas," NAVIGATION: Journal of the Institute of Navigation, Vol. 41, No. 3, pg. 277 - 295, Fall 1994.

4. Gomez, Susan F., "Field Test Comparison of Static Global Positioning System Attitude Determination Using Single and Double Difference Carrier Phase Measurements," NASA/JSC memo EG4-95-006, March 1995.

5. Marhefka, R. J., and J. W. Silvestro, "Near Zone - Basic Scattering Code User's Manual with Space Station Applications," NASA Contractor Report 181944, ElectroScience Laboratory, Ohio State University, December 1989.

6. Adkins, Antha A., "Dynamic Environment Communications Analysis Testbed (DECAT) Simulation of Multipath at International Space Station (ISS) Global Positioning System (GPS) Antennas - 9-28-94 19A Structure," SA&TS-95-089, June 1995.

7. Global Positioning System Interface Control Document (GPS ICD), ICD-GPS-200, revision B, November 1987.

8. Larsen, D. W., "International Space Station (ISS), United States On-Orbit Segment (USOS) Circuit Margin Data Book, April 1995 Revision," EV4-95-303, April 1995.

9. Cryan, Scott P., "GPS Engineering Test Summary Report: Results of a TANS Quadrex GPS Receiver Sensitivity Test," ETSR-95-001, January 1995.

10. Hwu, Shian, Ba Lu, and Robert Panneton, "Multipath Analysis for Space Station GPS Antennas: GPS Antennas Gain Degradation and Phase Shift Due to Station Structure Scattering Interference," EV3-94-14350, October 1994.

11. Corson, Roger, "Feasibility of a Concept for ISSA Attitude Determination Using GPS Interferometry," A96-J185-STN-M-RWC-950009, October 1995.

Appendix A - Drawings of Field Test Setup for Each Day

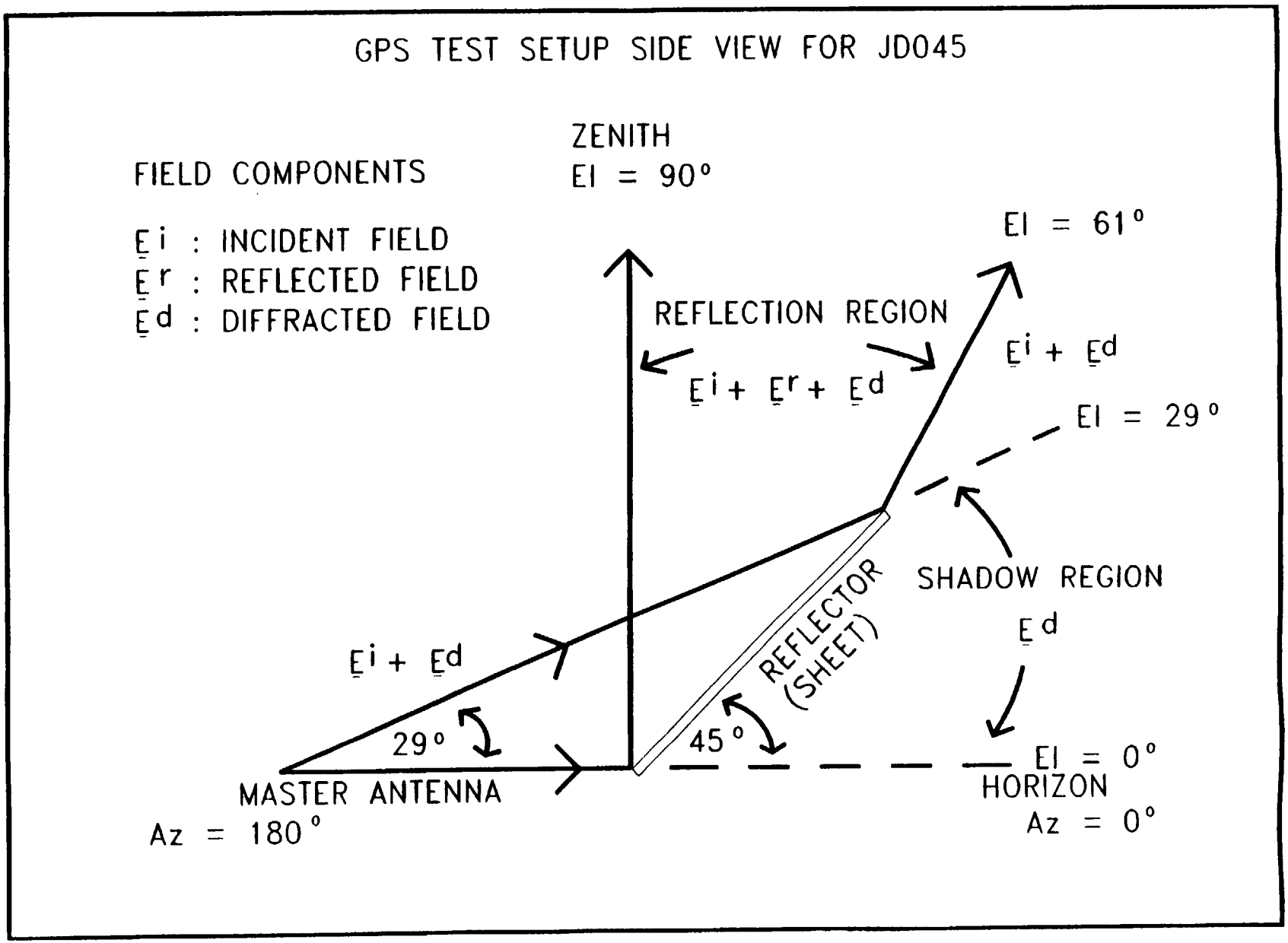
GPS TEST SETUP SIDE VIEW FOR JD045
FIELD COMPONENTS
Ei : INCIDENT FIELD
Er : REFLECTED FIELD
Ed : DIFFRACTED FIELD
ZENITH
El = 90°
El = 61°
REFLECTION REGION
Ei + Er + Ed
Ei + Ed
El = 29°
SHADOW REGION
Ed
REFLECTOR (SHEET)
Ei + Ed
29°
45°
El = 0°
HORIZON
Az = 0°
MASTER ANTENNA
Az = 180°

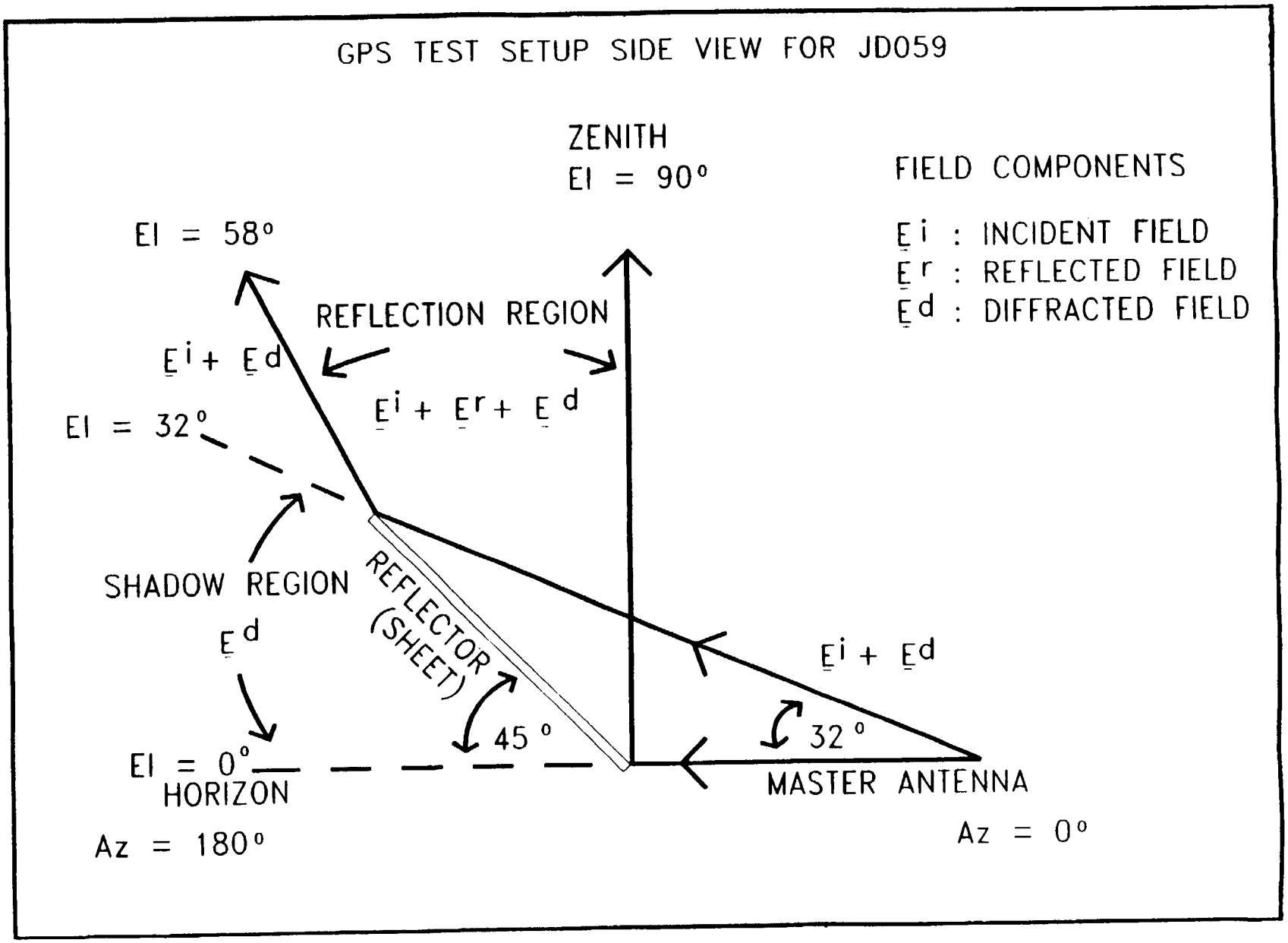
GPS TEST SETUP SIDE VIEW FOR JD059
ZENITH
El = 90°
El = 58°
FIELD COMPONENTS
Ei : INCIDENT FIELD
Er : REFLECTED FIELD
Ed : DIFFRACTED FIELD
REFLECTION REGION
Ei + Ed
Ei + Er + Ed
El = 32°
SHADOW REGION
Ed
REFLECTOR (SHEET)
Ei + Ed
45°
32°
El = 0°
HORIZON
MASTER ANTENNA
Az = 180°
Az = 0°

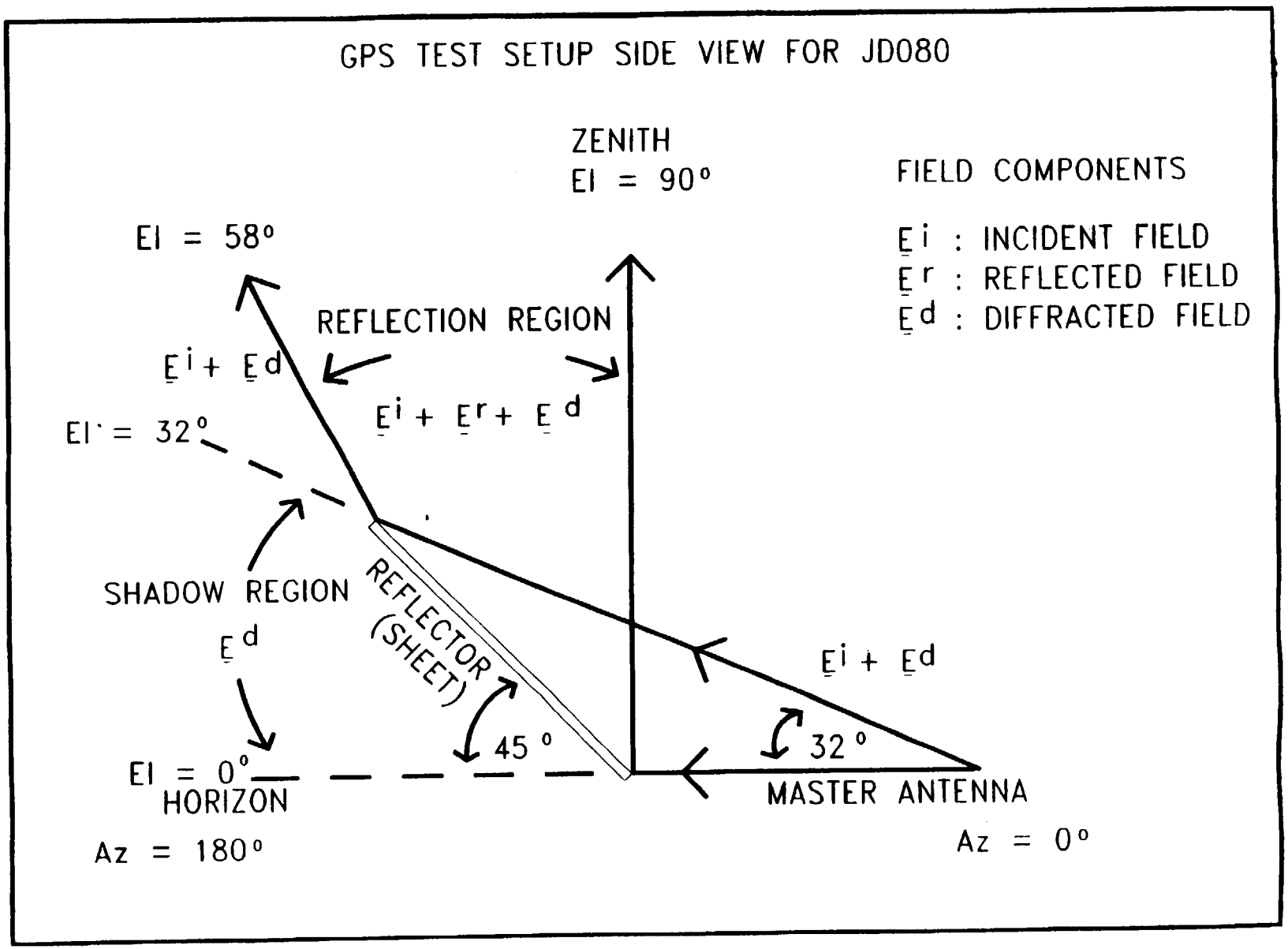
GPS TEST SETUP SIDE VIEW FOR JD080
ZENITH
El = 90°
FIELD COMPONENTS
Ei : INCIDENT FIELD
Er : REFLECTED FIELD
Ed : DIFFRACTED FIELD
El = 58°
REFLECTION REGION
Ei + Ed
Ei + Er + Ed
El = 32°
SHADOW REGION
Ed
REFLECTOR (SHEET)
Ei + Ed
45°
32°
El = 0°
HORIZON
MASTER ANTENNA
Az = 180°
Az = 0°

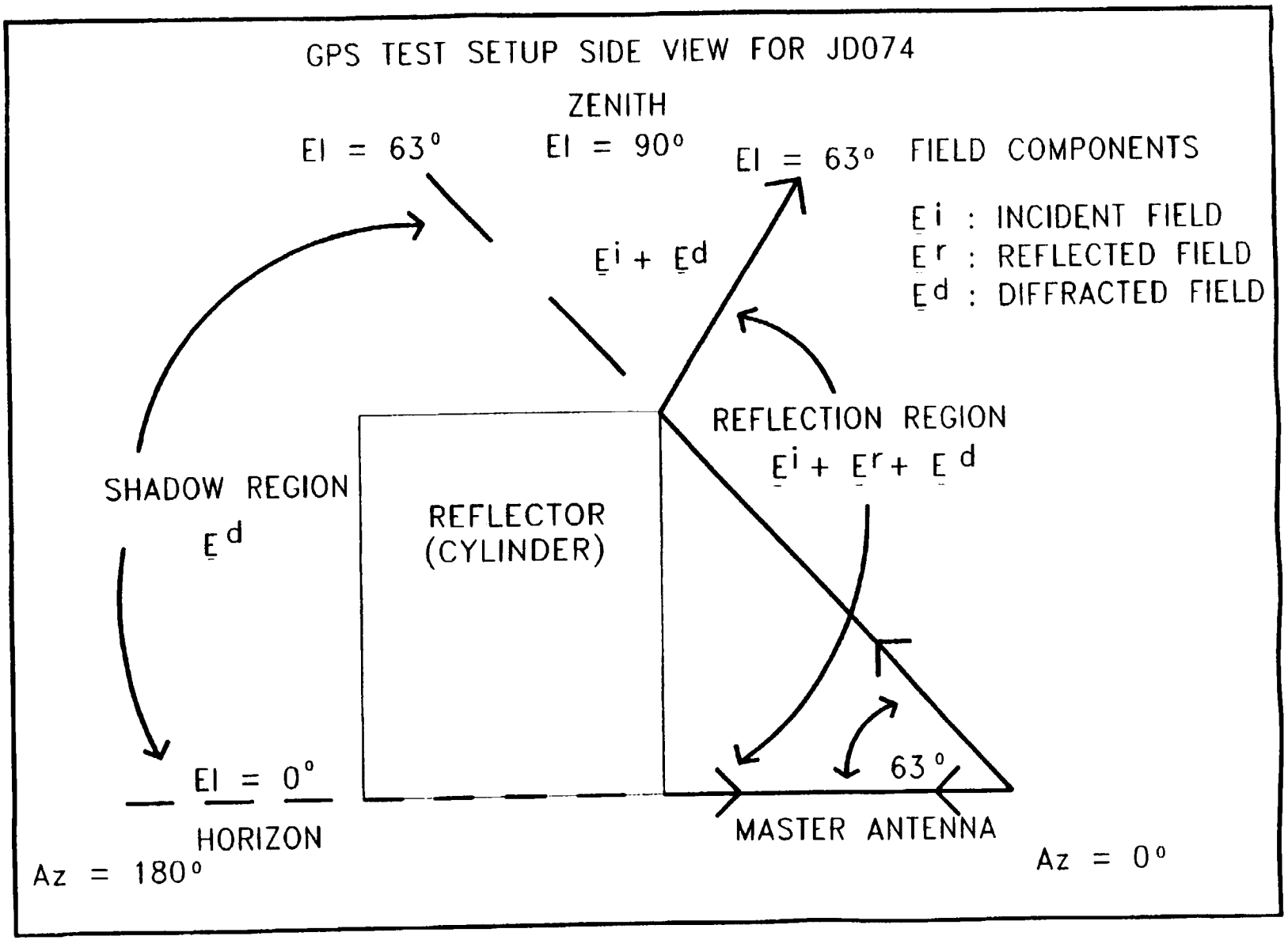
GPS TEST SETUP SIDE VIEW FOR JD074
ZENITH
EI = 63°
EI = 90°
EI = 63° FIELD COMPONENTS
Ei : INCIDENT FIELD
Er : REFLECTED FIELD
Ed : DIFFRACTED FIELD
Ei + Ed
REFLECTION REGION
Ei + Er + Ed
SHADOW REGION
Ed
REFLECTOR
(CYLINDER)
EI = 0°
HORIZON
63°
MASTER ANTENNA
Az = 180°
Az = 0°

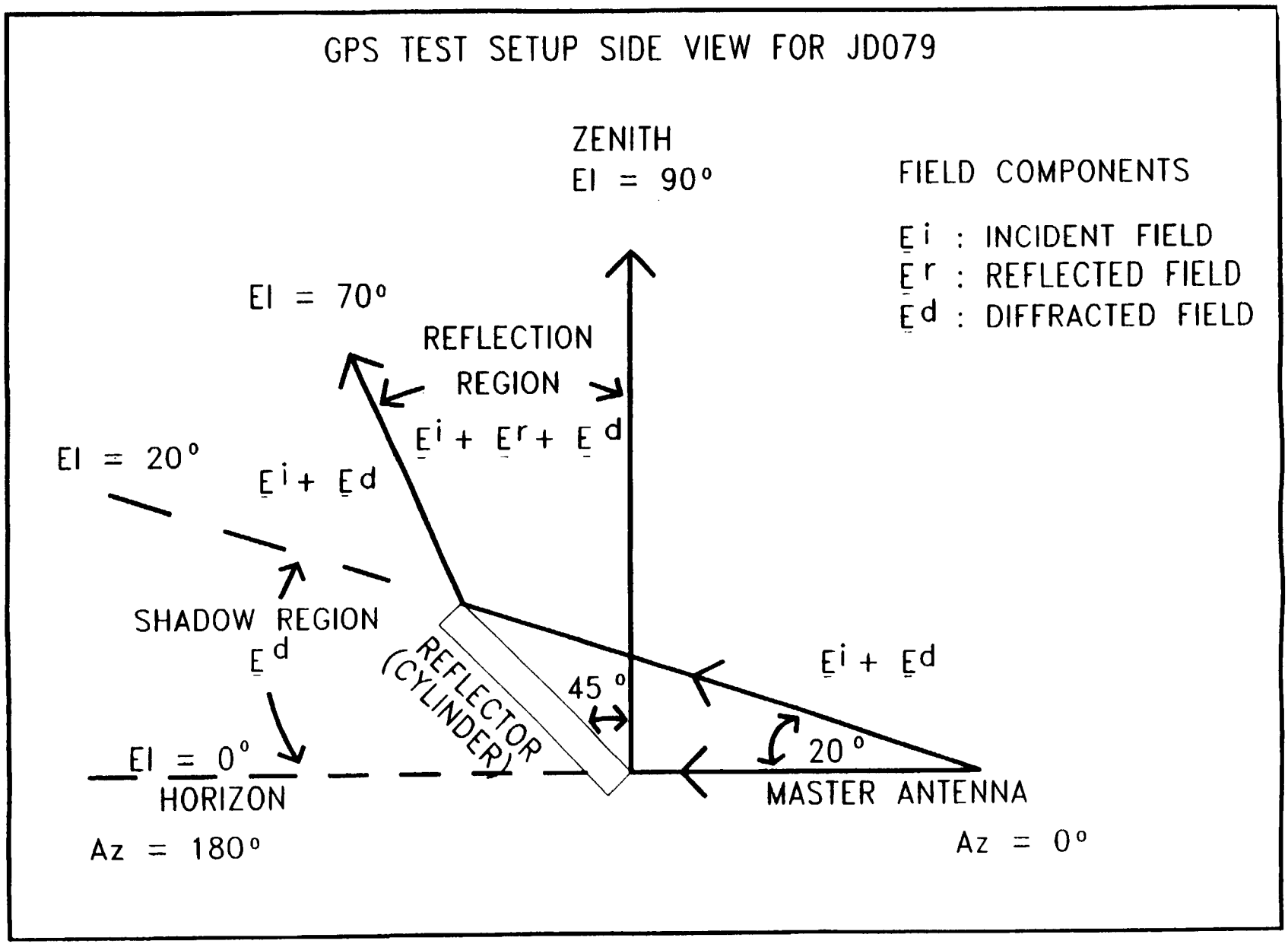
GPS TEST SETUP SIDE VIEW FOR JD079
ZENITH
El = 90°
FIELD COMPONENTS
Ei : INCIDENT FIELD
Er : REFLECTED FIELD
Ed : DIFFRACTED FIELD
El = 70°
REFLECTION
REGION
Ei + Er + Ed
El = 20°
Ei + Ed
SHADOW REGION
Ed
REFLECTOR
(CYLINDER)
45°
Ei + Ed
20°
El = 0°
HORIZON
MASTER ANTENNA
Az = 180°
Az = 0°

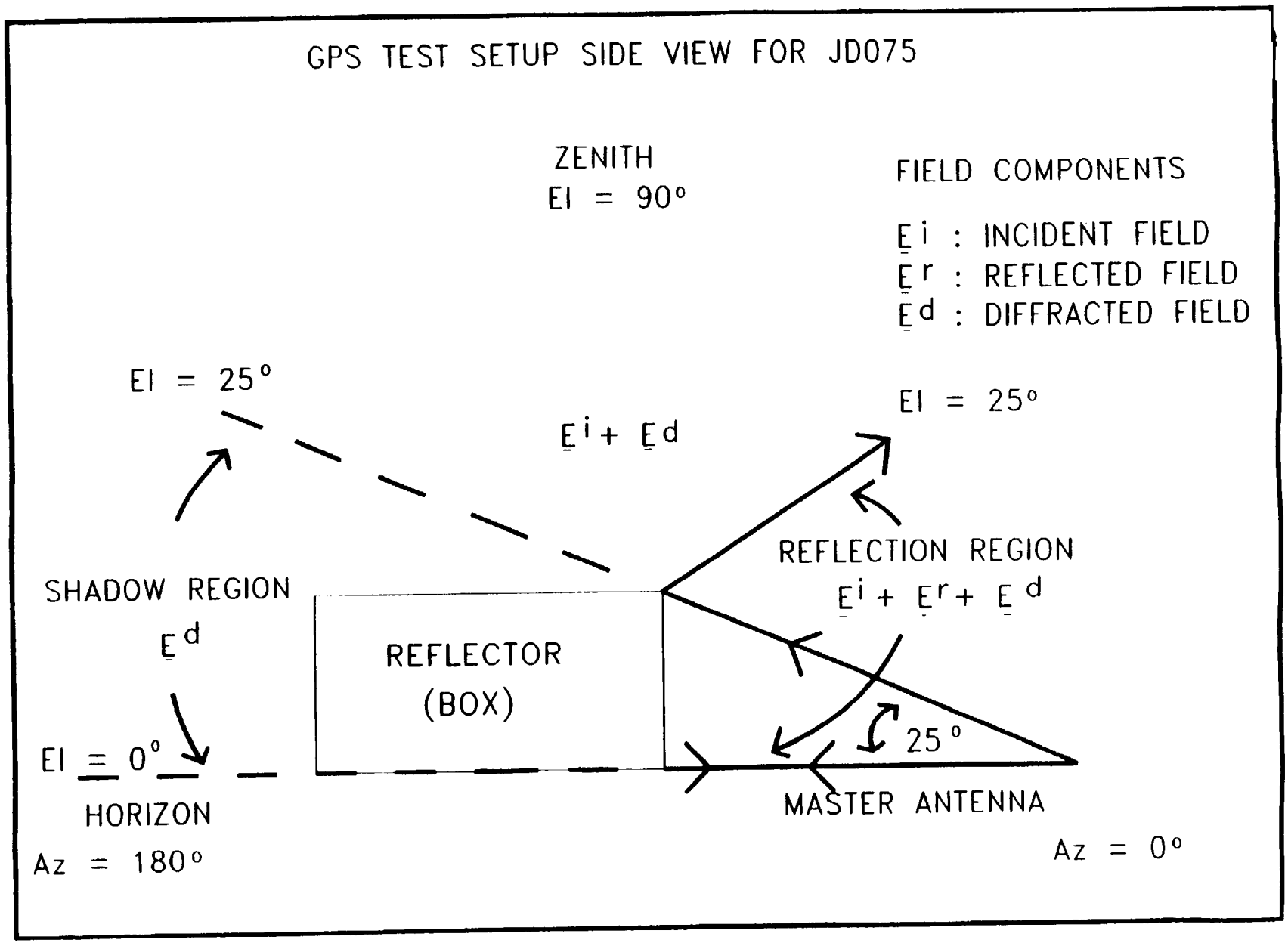
GPS TEST SETUP SIDE VIEW FOR JD075
ZENITH
El = 90°
FIELD COMPONENTS
Ei : INCIDENT FIELD
Er : REFLECTED FIELD
Ed : DIFFRACTED FIELD
El = 25°
Ei + Ed
El = 25°
REFLECTION REGION
Ei + Er + Ed
SHADOW REGION
Ed
REFLECTOR
(BOX)
25°
El = 0°
HORIZON
Az = 180°
MASTER ANTENNA
Az = 0°

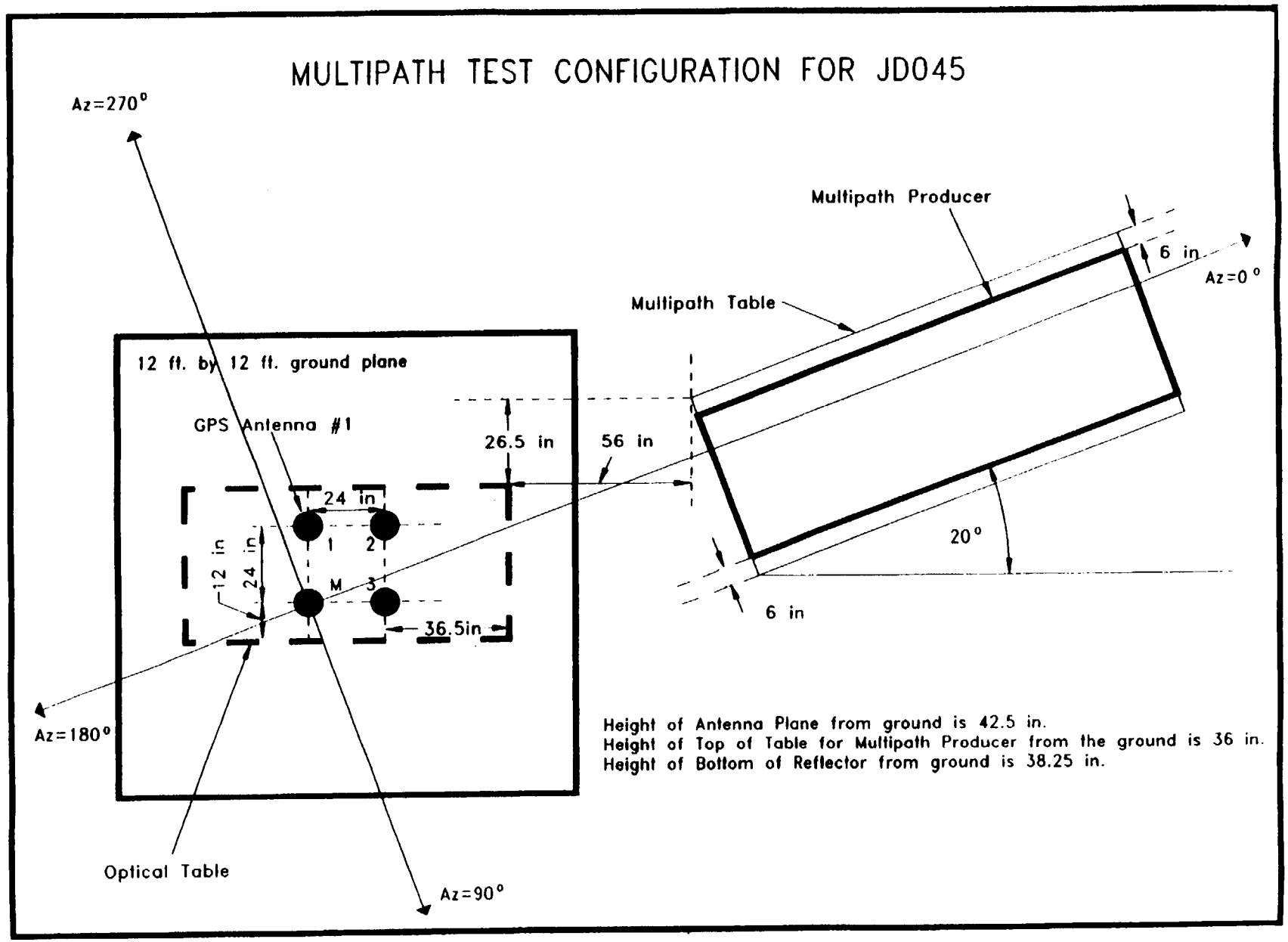
MULTIPATH TEST CONFIGURATION FOR JD045
Az=270°
Multipath Producer
6 in
Az=0°
Multipath Table
12 ft. by 12 ft. ground plane
GPS Antenna #1
26.5 in
56 in
24 in
1
2
M
3
12 in
24 in
36.5in
20°
6 in
Az=180°
Height of Antenna Plane from ground is 42.5 in.
Height of Top of Table for Multipath Producer from the ground is 36 in.
Height of Bottom of Reflector from ground is 38.25 in.
Optical Table
Az=90°

MULTIPATH TEST CONFIGURATION FOR JD059

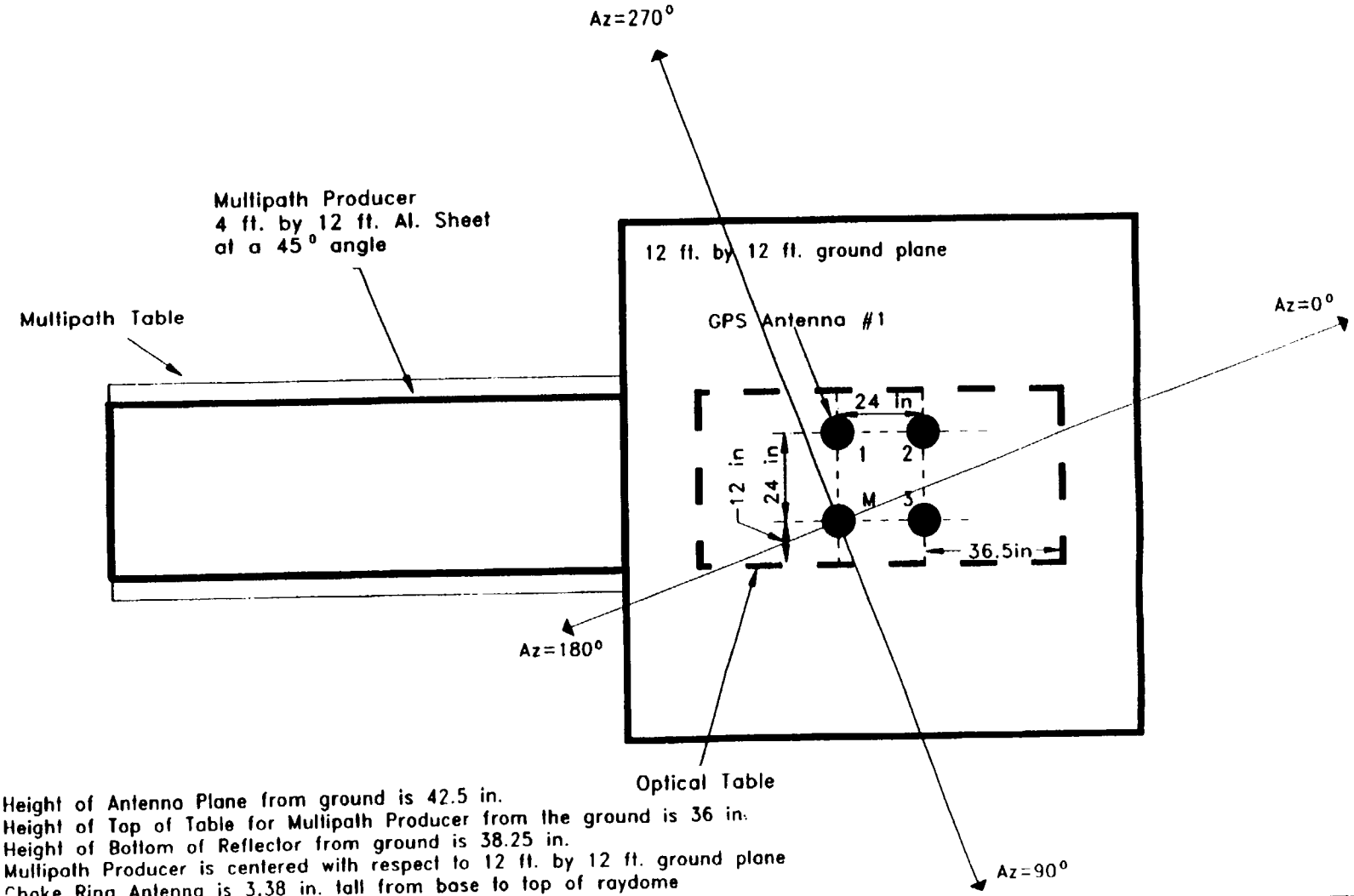

Height of Antenna Plane from ground is 42.5 in.
Height of Top of Table for Multipath Producer from the ground is 36 in.
Height of Bottom of Reflector from ground is 38.25 in.
Multipath Producer is centered with respect to 12 ft. by 12 ft. ground plane
Choke Ring Antenna is 3.38 in. tall from base to top of raydome

MULTIPATH TEST CONFIGURATION FOR JD080

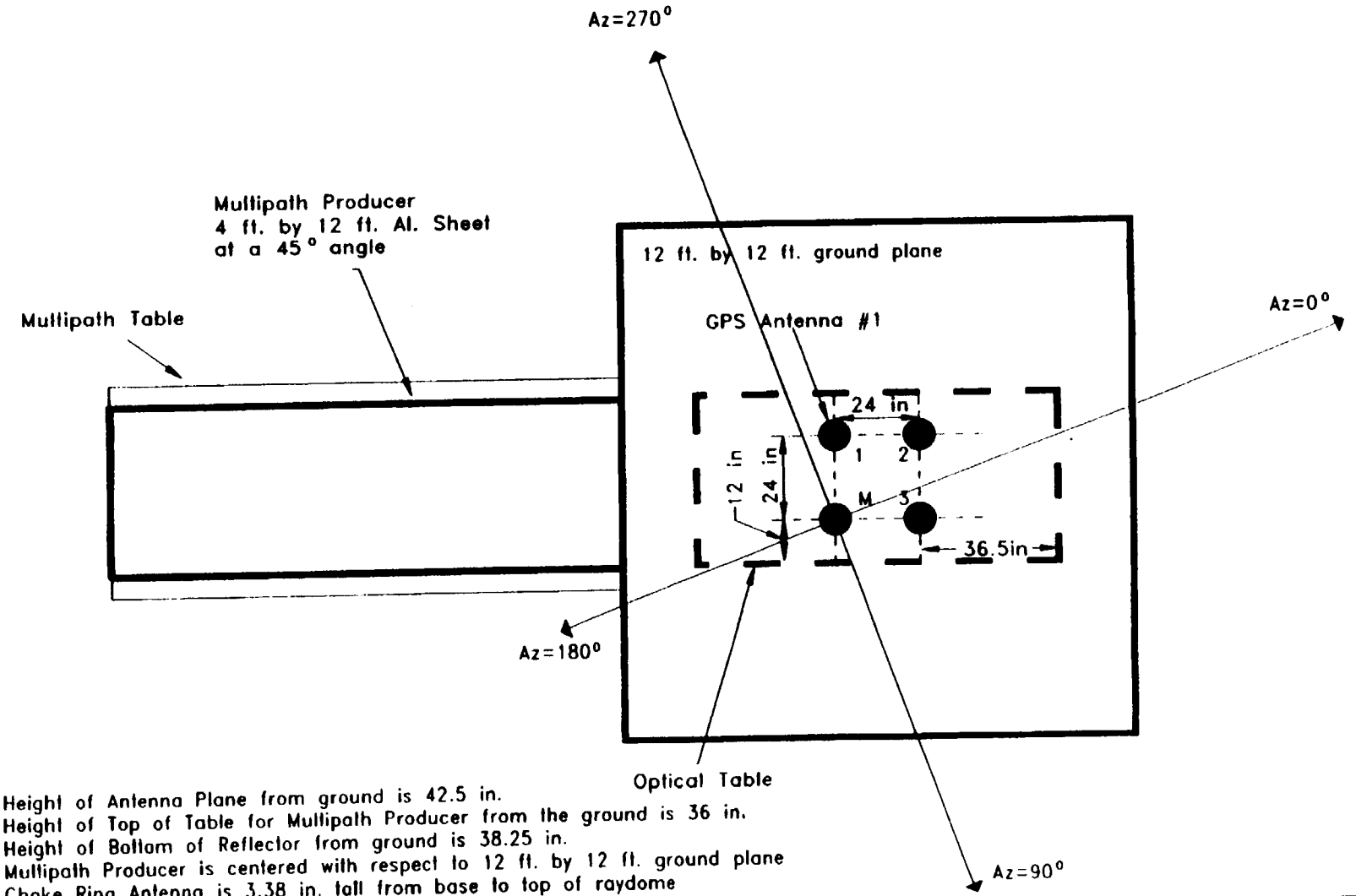

Height of Antenna Plane from ground is 42.5 in.
Height of Top of Table for Multipath Producer from the ground is 36 in.
Height of Bottom of Reflector from ground is 38.25 in.
Multipath Producer is centered with respect to 12 ft. by 12 ft. ground plane
Choke Ring Antenna is 3.38 in. tall from base to top of raydome

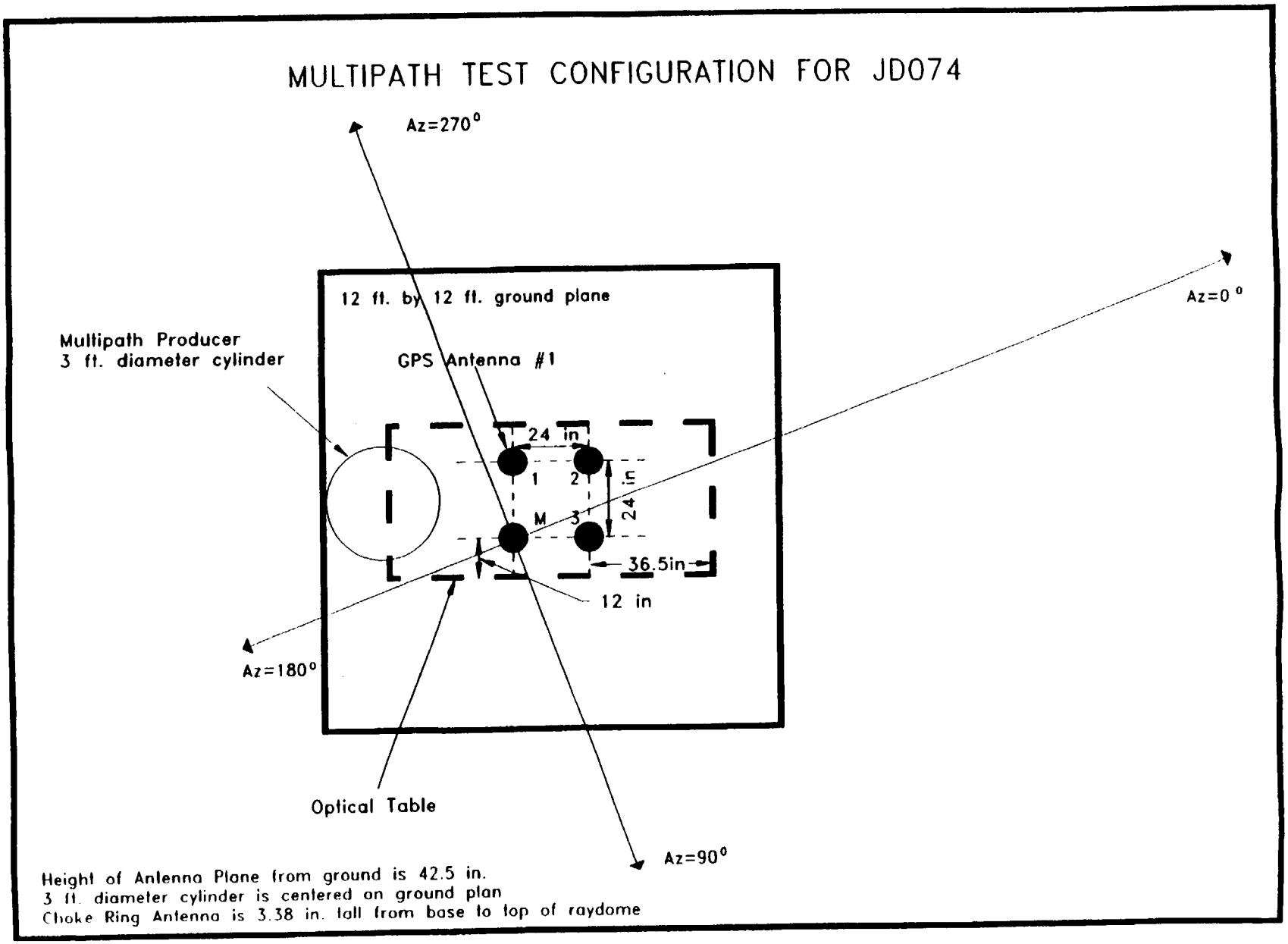
MULTIPATH TEST CONFIGURATION FOR JD074
Az=270°
12 ft. by 12 ft. ground plane
Az=0°
Mullipath Producer
3 ft. diameter cylinder
GPS Antenna #1
24 in
1
2
24 in
M
3
36.5in
12 in
Az=180°
Optical Table
Az=90°
Height of Antenna Plane from ground is 42.5 in.
3 ft. diameter cylinder is centered on ground plan
Choke Ring Antenna is 3.38 in. tall from base to top of raydome

MULTIPATH TEST CONFIGURATION FOR JD079

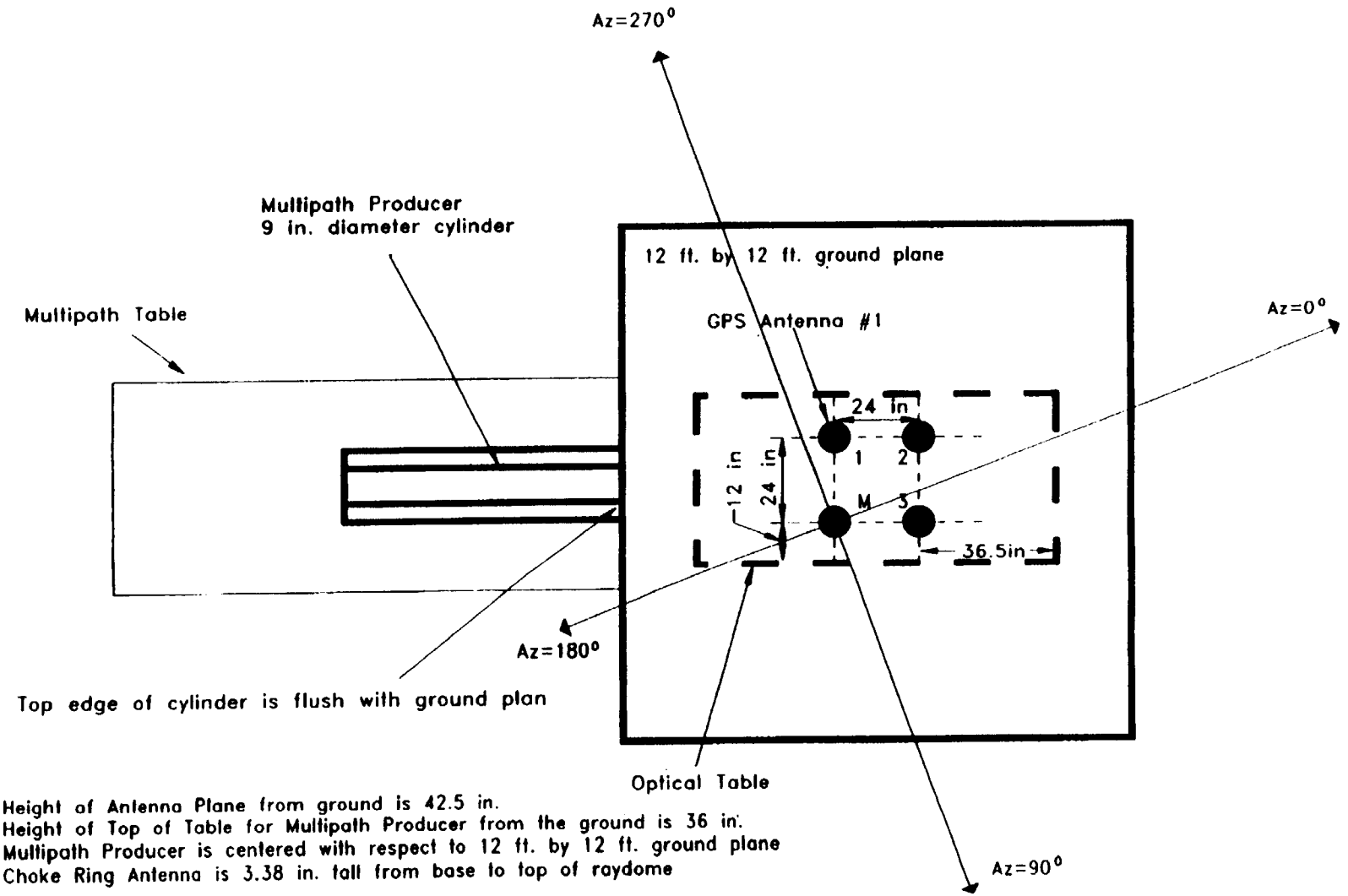

Height of Antenna Plane from ground is 42.5 in.
Height of Top of Table for Multipath Producer from the ground is 36 in.
Multipath Producer is centered with respect to 12 ft. by 12 ft. ground plane
Choke Ring Antenna is 3.38 in. tall from base to top of raydome

MULTIPATH TEST CONFIGURATION FOR JD075

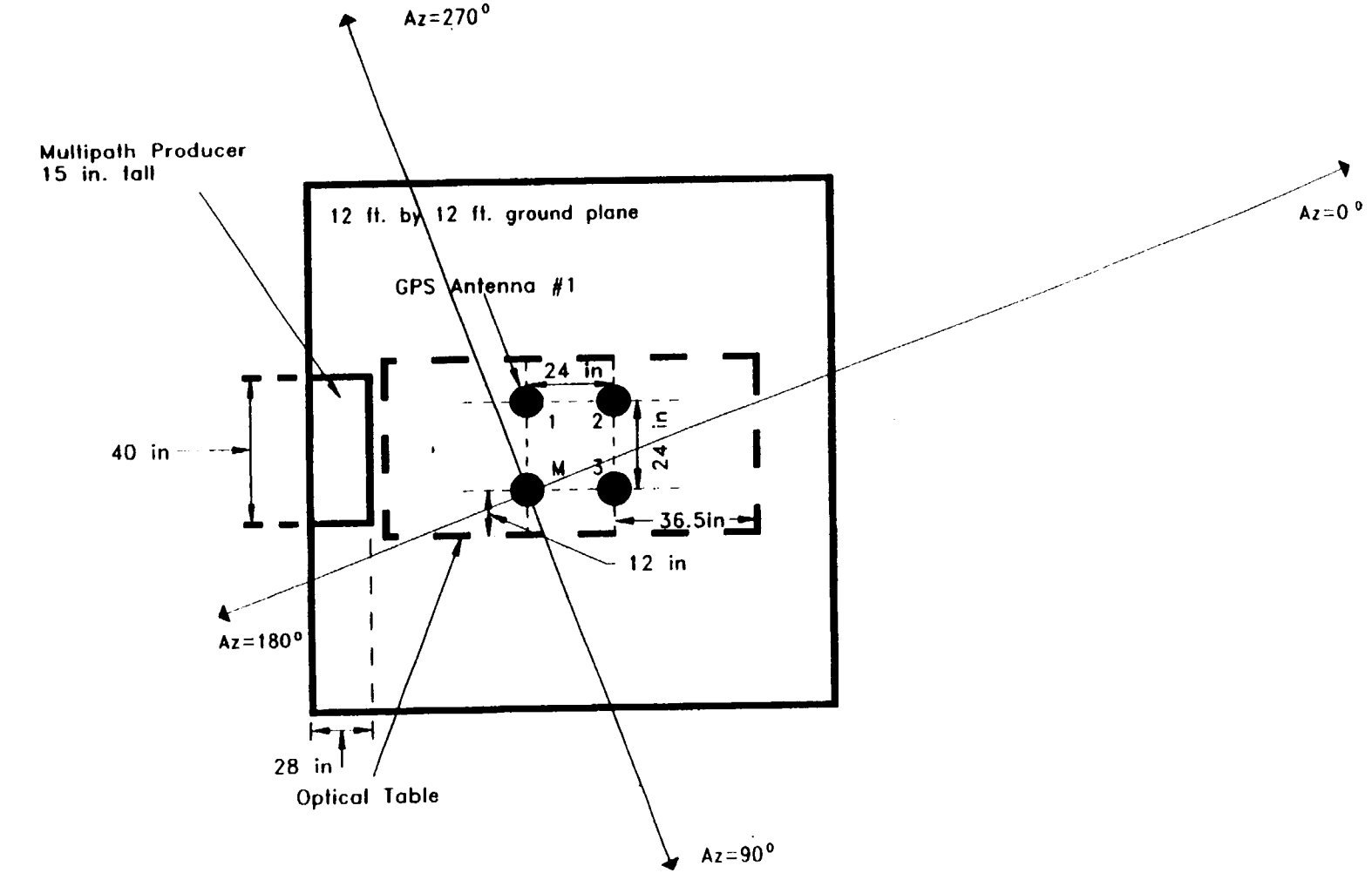

Height of Antenna Plane from ground is 42.5 in.
Choke Ring Antenna is 3.38 in. tall from base to top of raydome

Multipath Test Configuration

JD 045

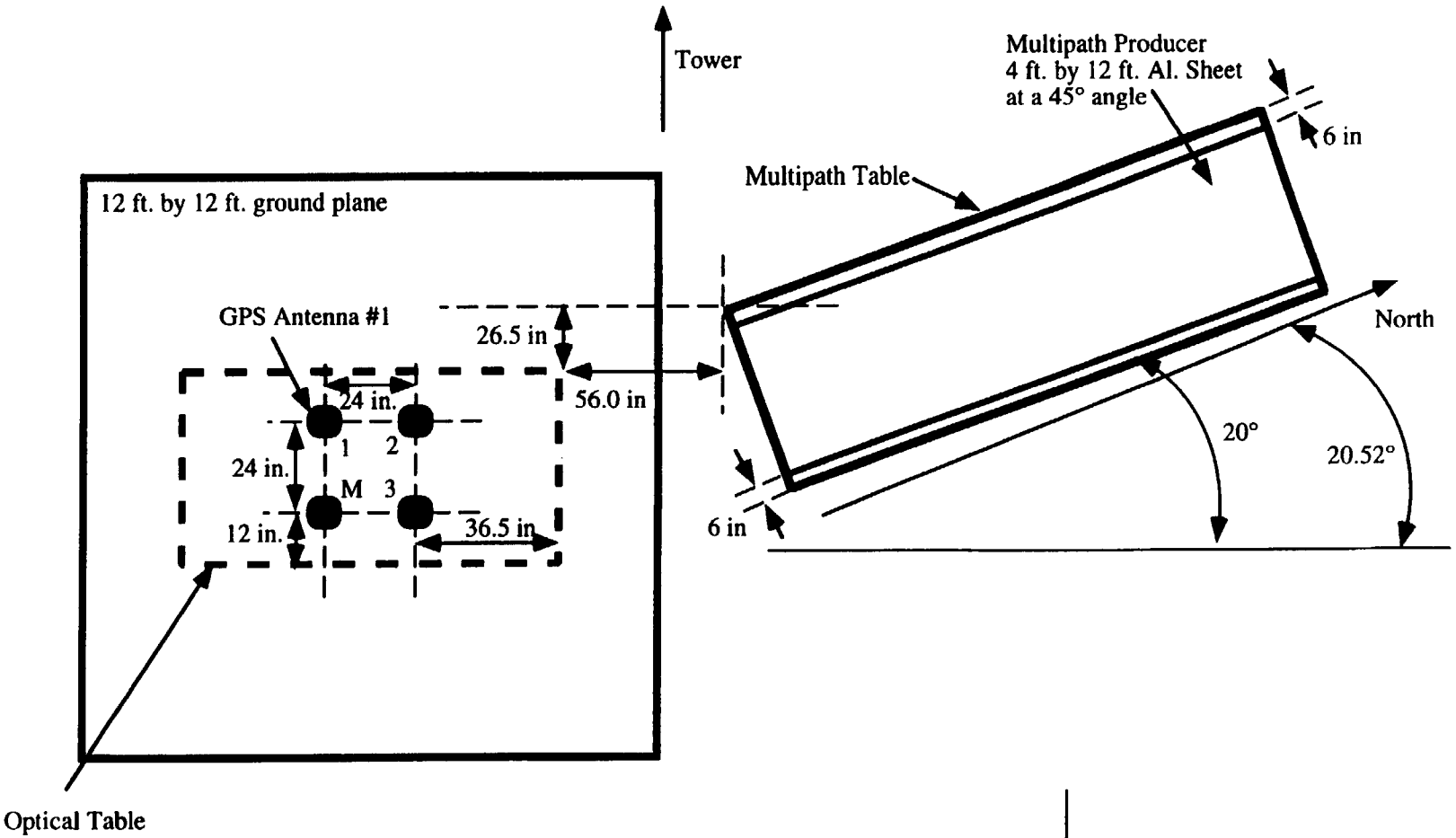

Height of Antenna Plane from ground is 42.5 in.
Height of Top of Table for Multipath Producer from the ground is 36 in.
Height of Bottom of Reflector from ground is 38.25 in.

Multipath Test Configuration

JD 052

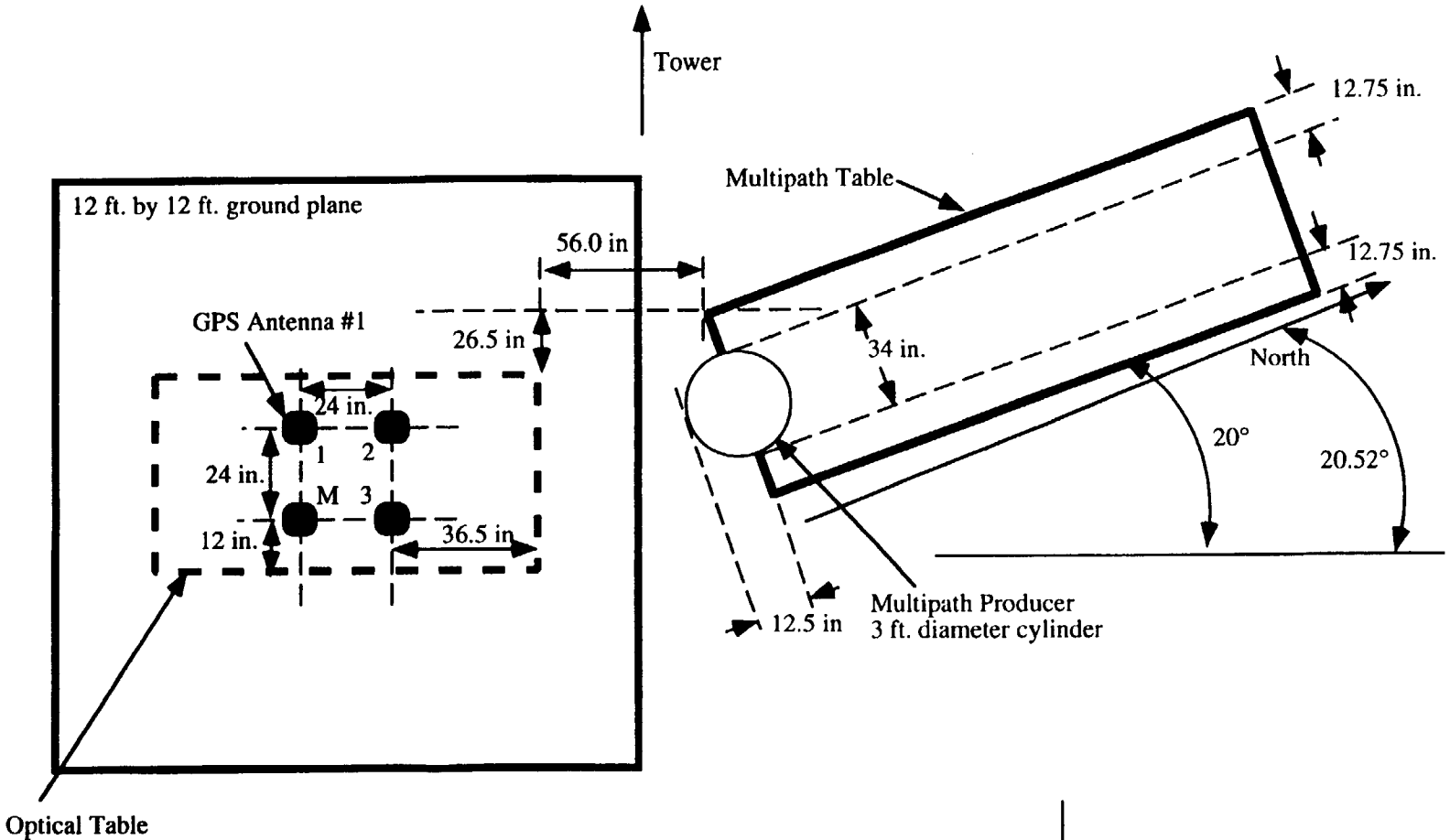

Height of Antenna Plane from ground is 42.5 in.
Height of Top of Table for Multipath Producer from the ground is 36 in.
Height of Bottom of Reflector from ground is 38.25 in.

Bldg. 14

Multipath Test Configuration

JD 054

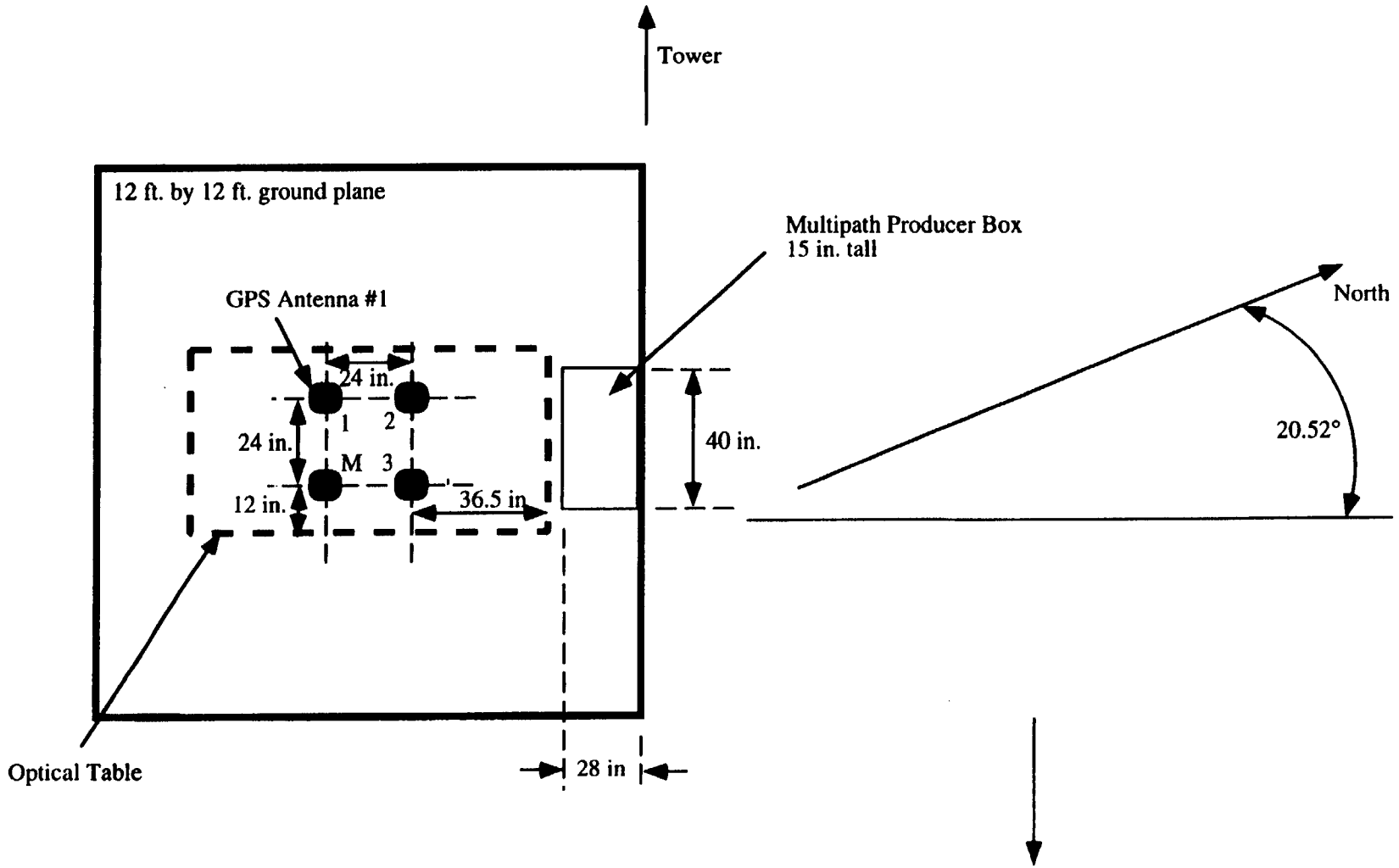

Height of Antenna Plane from ground is 42.5 in.

Multipath Test Configuration

JD 058

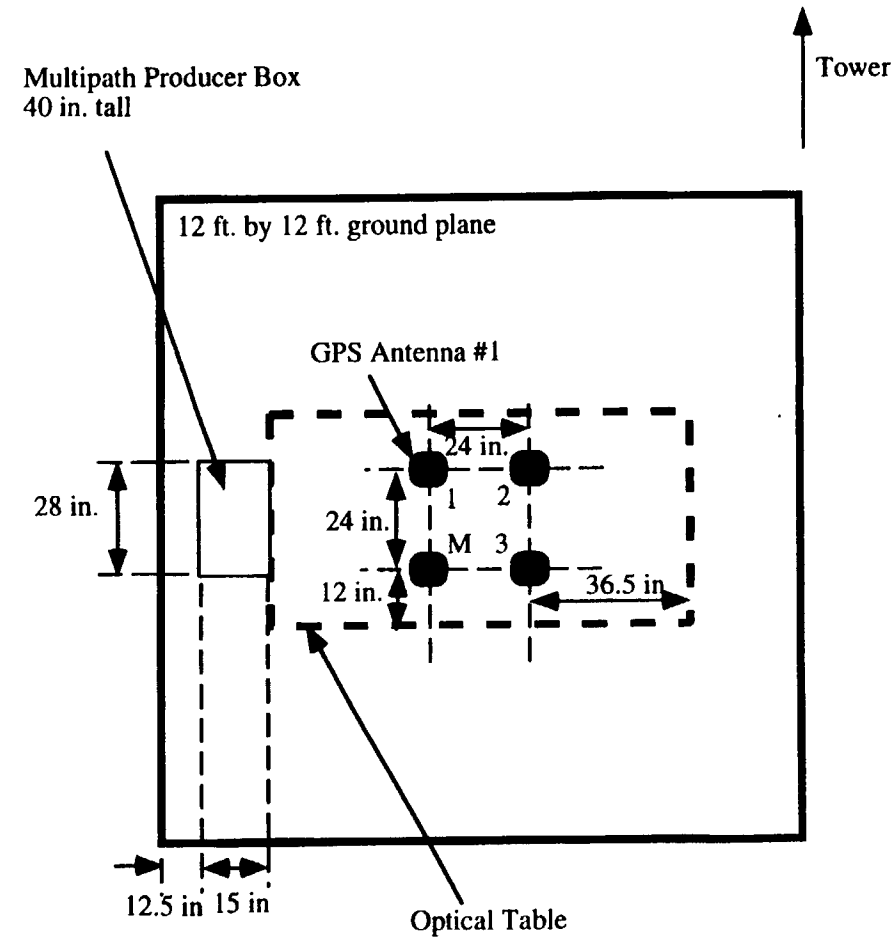

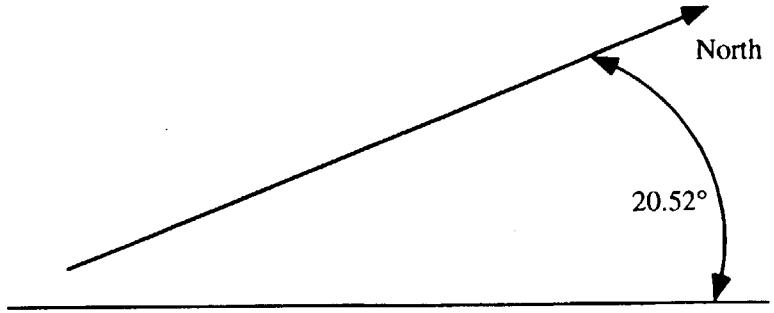

Height of Antenna Plane from ground is 42.5 in.

Bldg. 14

Multipath Test Configuration

JD 059

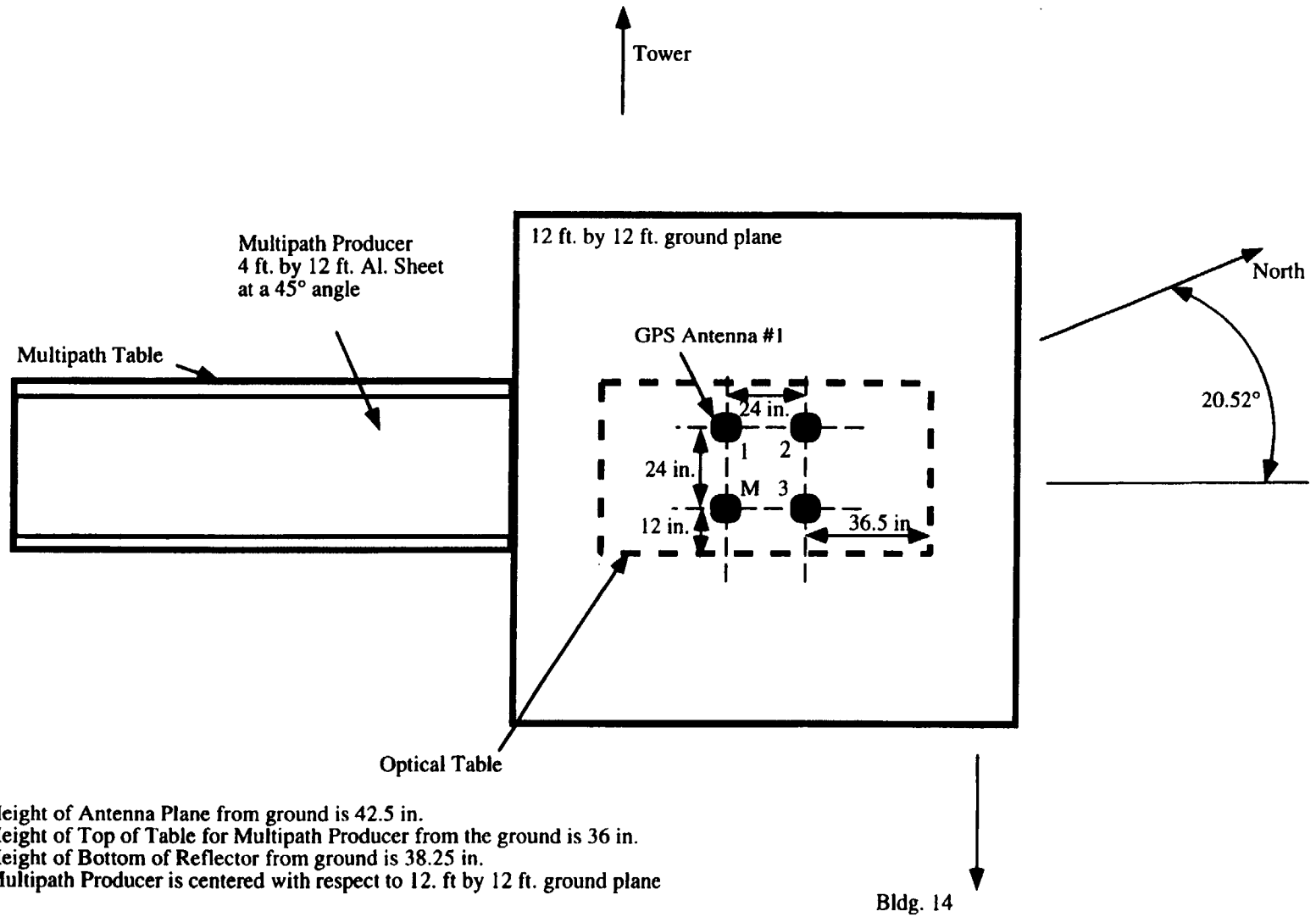

Height of Antenna Plane from ground is 42.5 in.
Height of Top of Table for Multipath Producer from the ground is 36 in.
Height of Bottom of Reflector from ground is 38.25 in.
Multipath Producer is centered with respect to 12. ft by 12 ft. ground plane

Multipath Test Configuration

JD 060

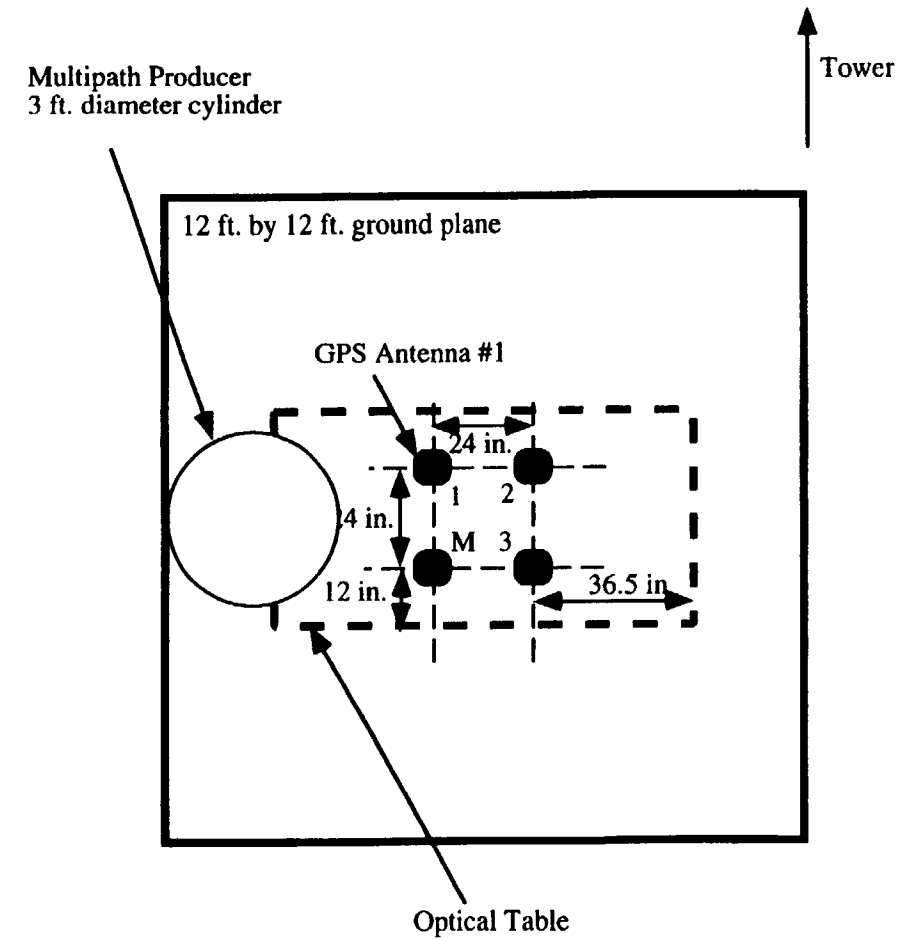

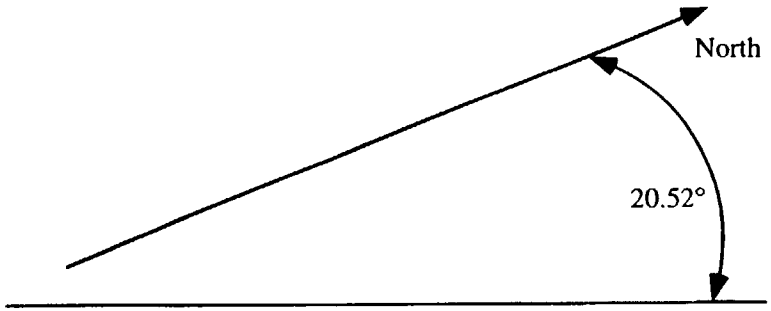

Height of Antenna Plane from ground is 42.5 in.
3 ft. diameter cylinder is centered on ground plan

Bldg. 14

Multipath Test Configuration

JD 061

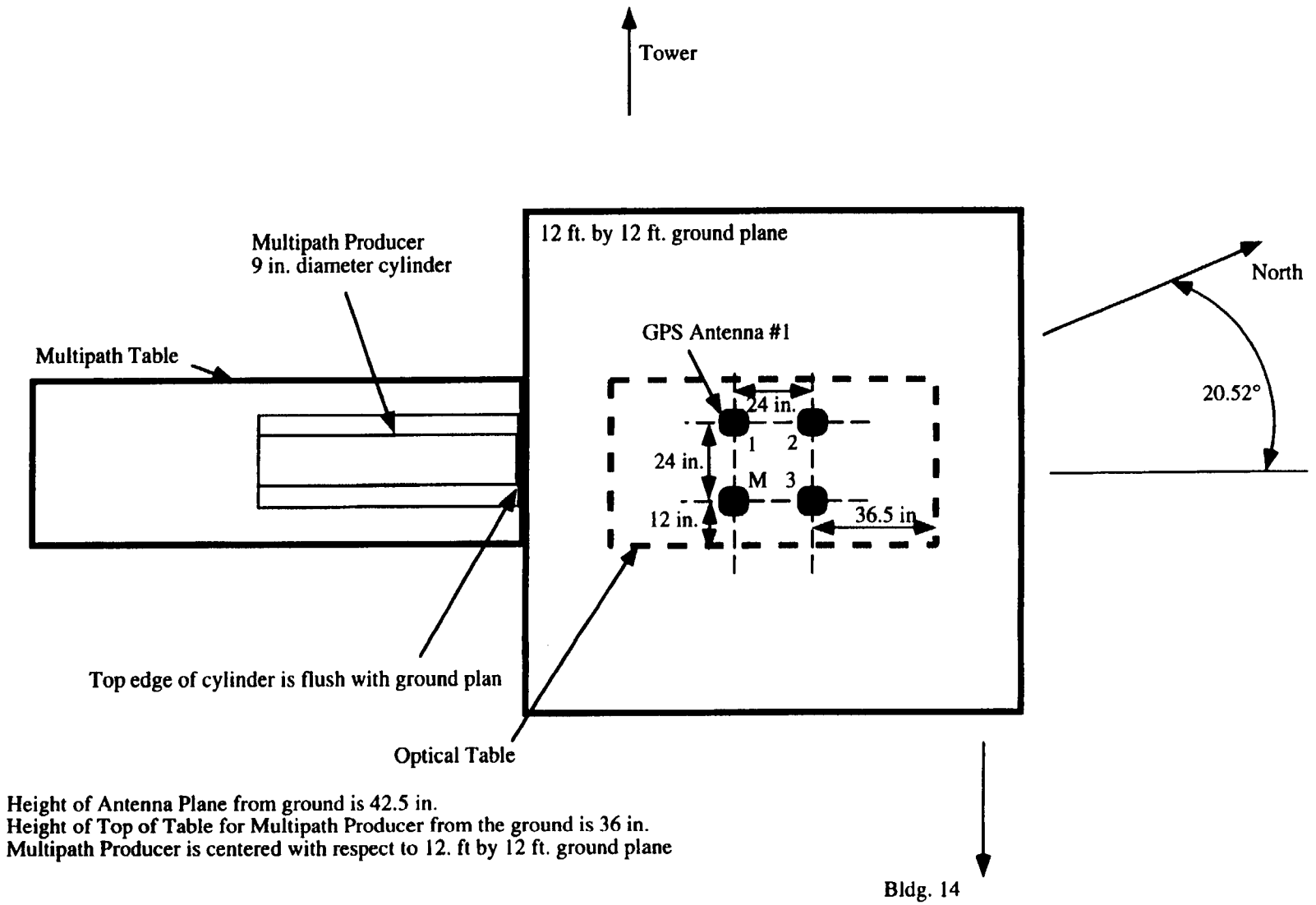

Height of Antenna Plane from ground is 42.5 in.
Height of Top of Table for Multipath Producer from the ground is 36 in.
Multipath Producer is centered with respect to 12. ft by 12 ft. ground plane

Multipath Test Configuration
JD 065

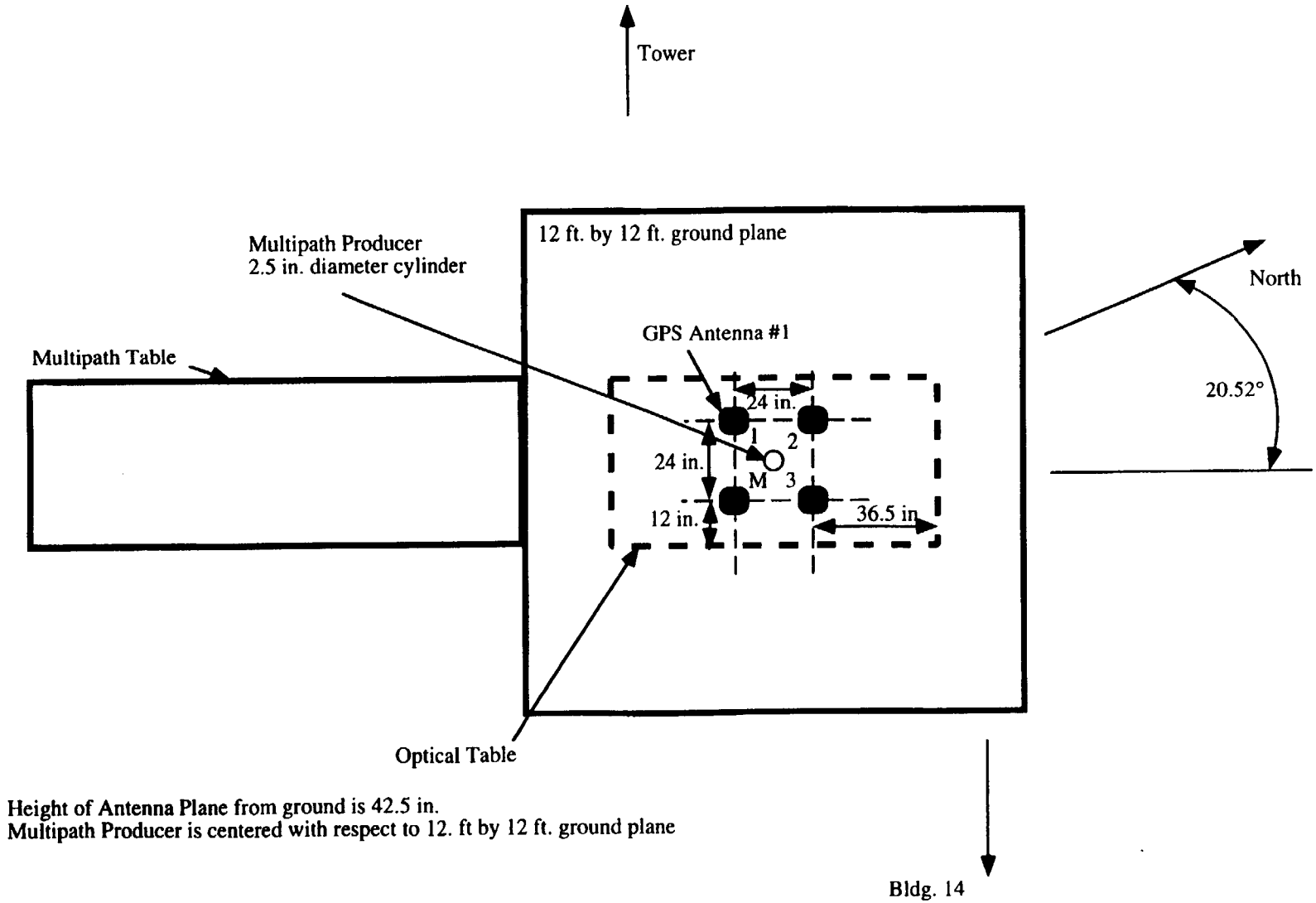

Height of Antenna Plane from ground is 42.5 in.
Multipath Producer is centered with respect to 12. ft by 12 ft. ground plane

Multipath Test Configuration

JD 074

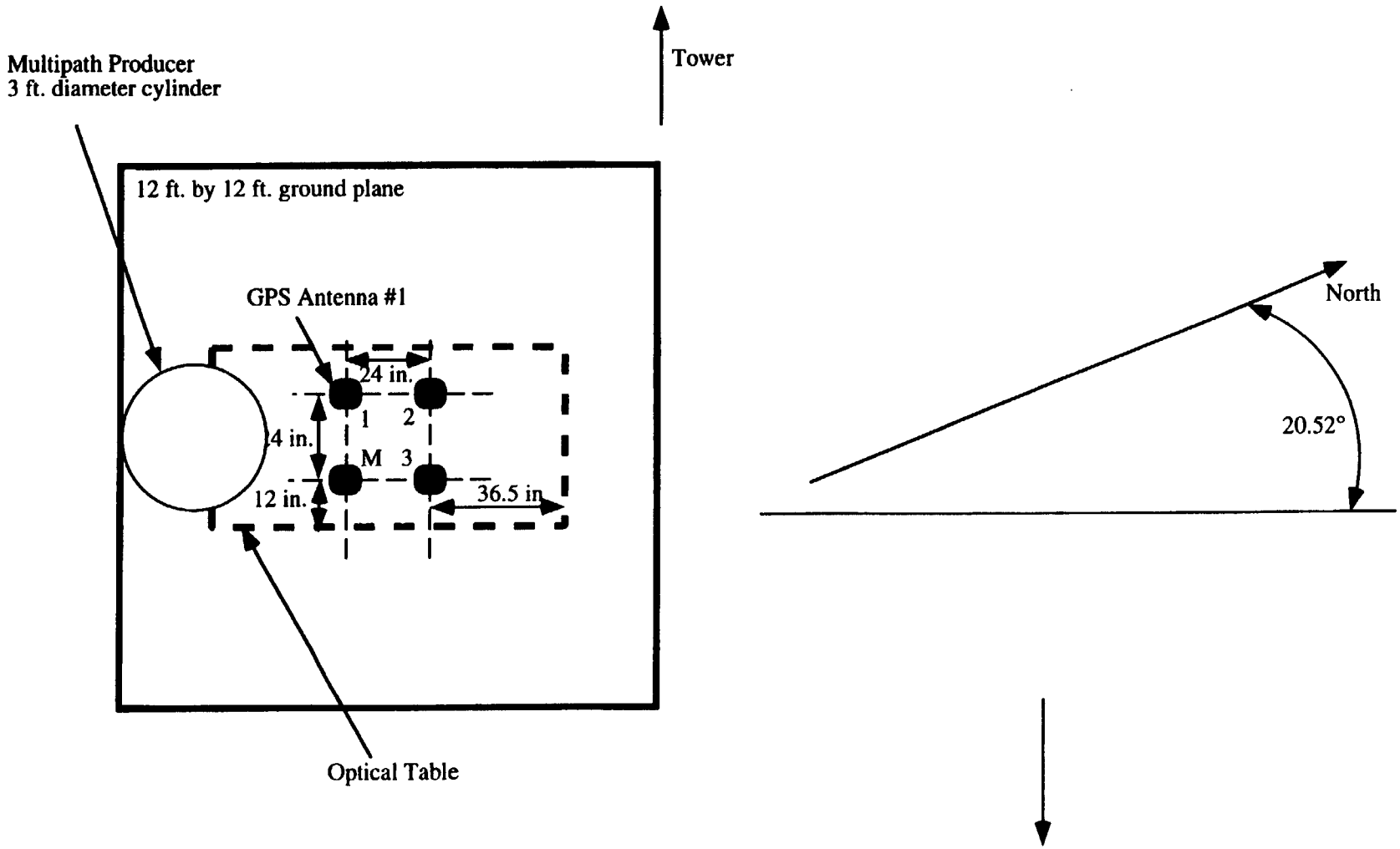

Height of Antenna Plane from ground is 42.5 in.
3 ft. diameter cylinder is centered on ground plan
Choke Ring Antenna is 3.38 in. tall from base to top of raydome

Multipath Test Configuration

JD 075

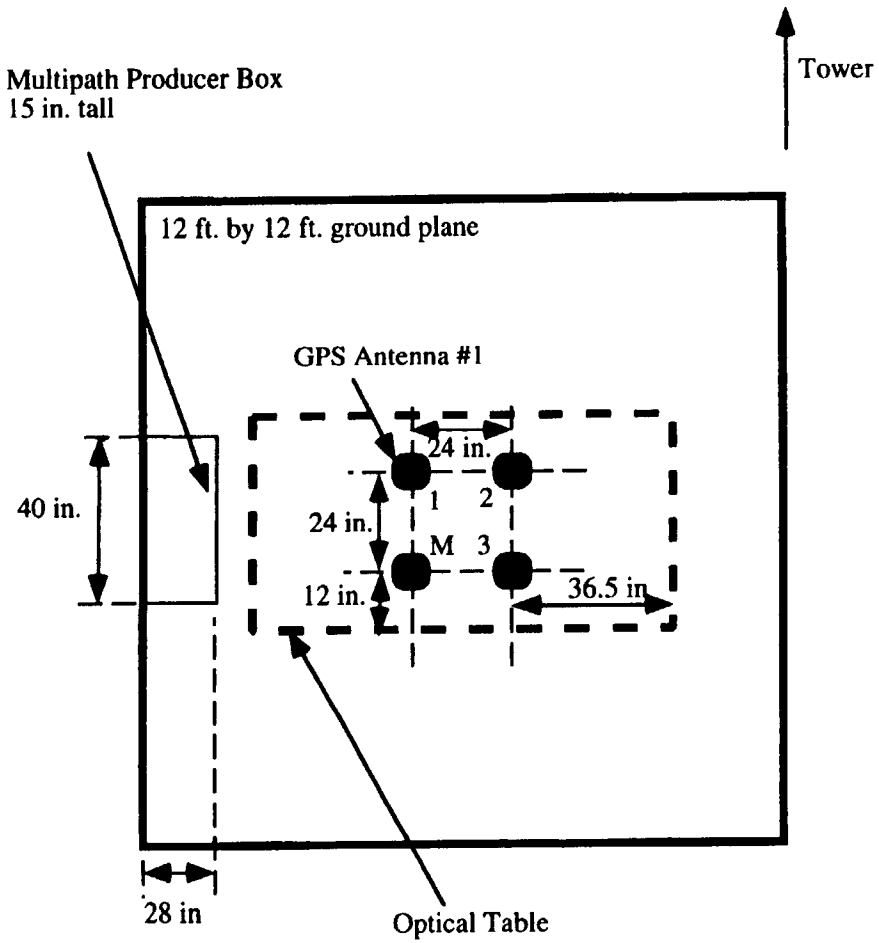

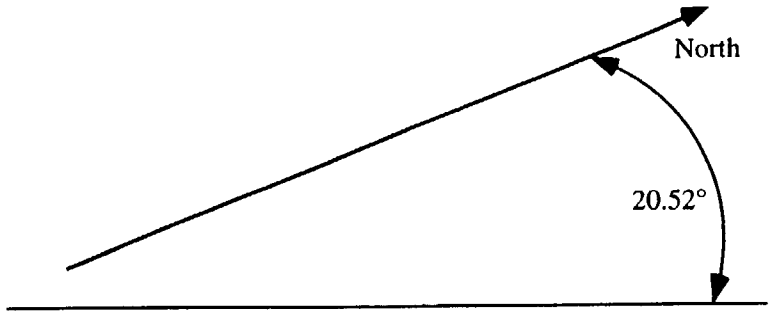

Height of Antenna Plane from ground is 42.5 in.
Choke Ring Antenna is 3.38 in. tall from base to top of raydome

Bldg. 14

Multipath Test Configuration

JD 079

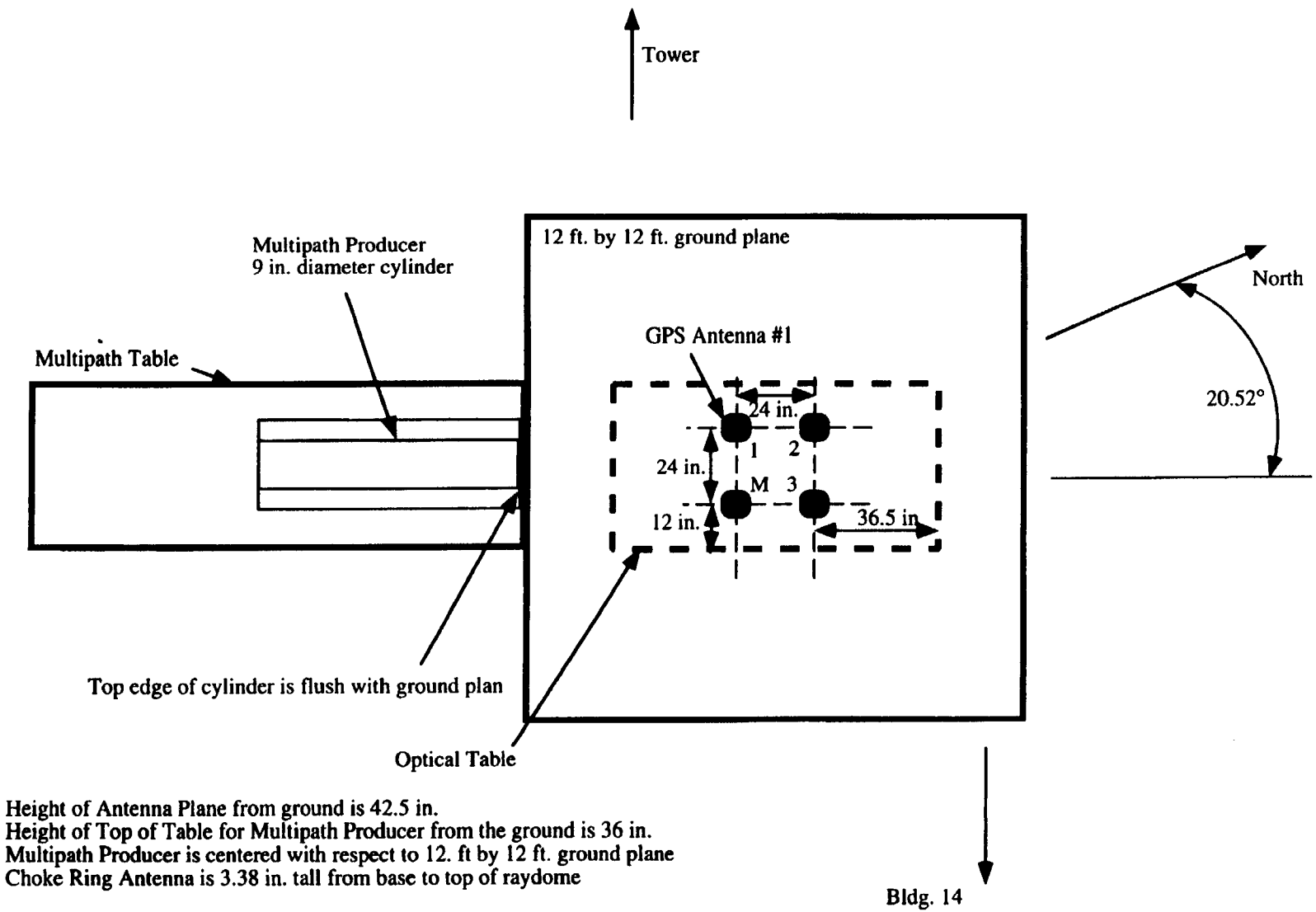

Height of Antenna Plane from ground is 42.5 in.
Height of Top of Table for Multipath Producer from the ground is 36 in.
Multipath Producer is centered with respect to 12. ft by 12 ft. ground plane
Choke Ring Antenna is 3.38 in. tall from base to top of raydome

Multipath Test Configuration

JD 080

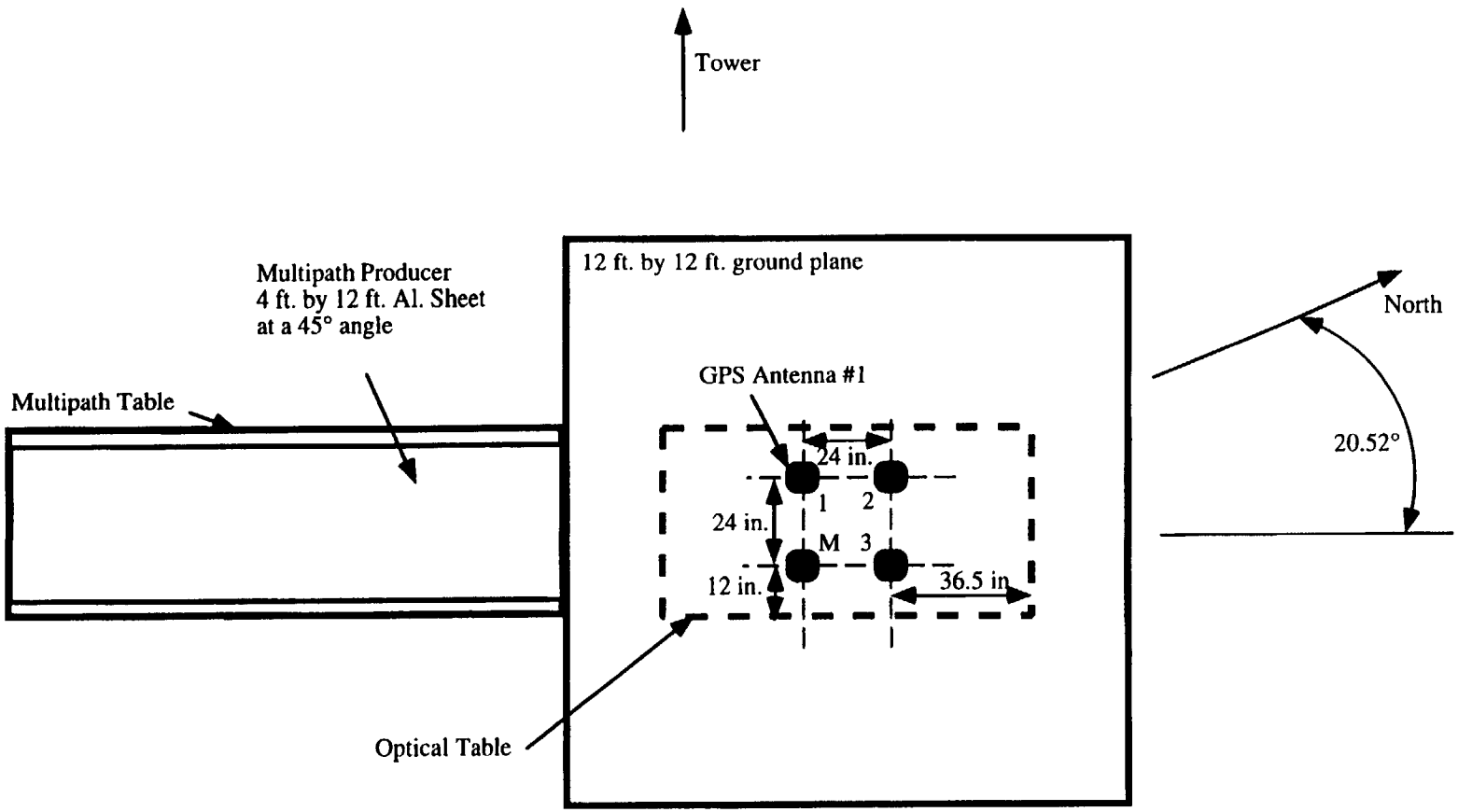

Height of Antenna Plane from ground is 42.5 in.
Height of Top of Table for Multipath Producer from the ground is 36 in.
Height of Bottom of Reflector from ground is 38.25 in.
Multipath Producer is centered with respect to 12. ft by 12 ft. ground plane
Choke Ring Antenna is 3.38 in. tall from base to top of raydome

Multipath Test Configuration

JD 081

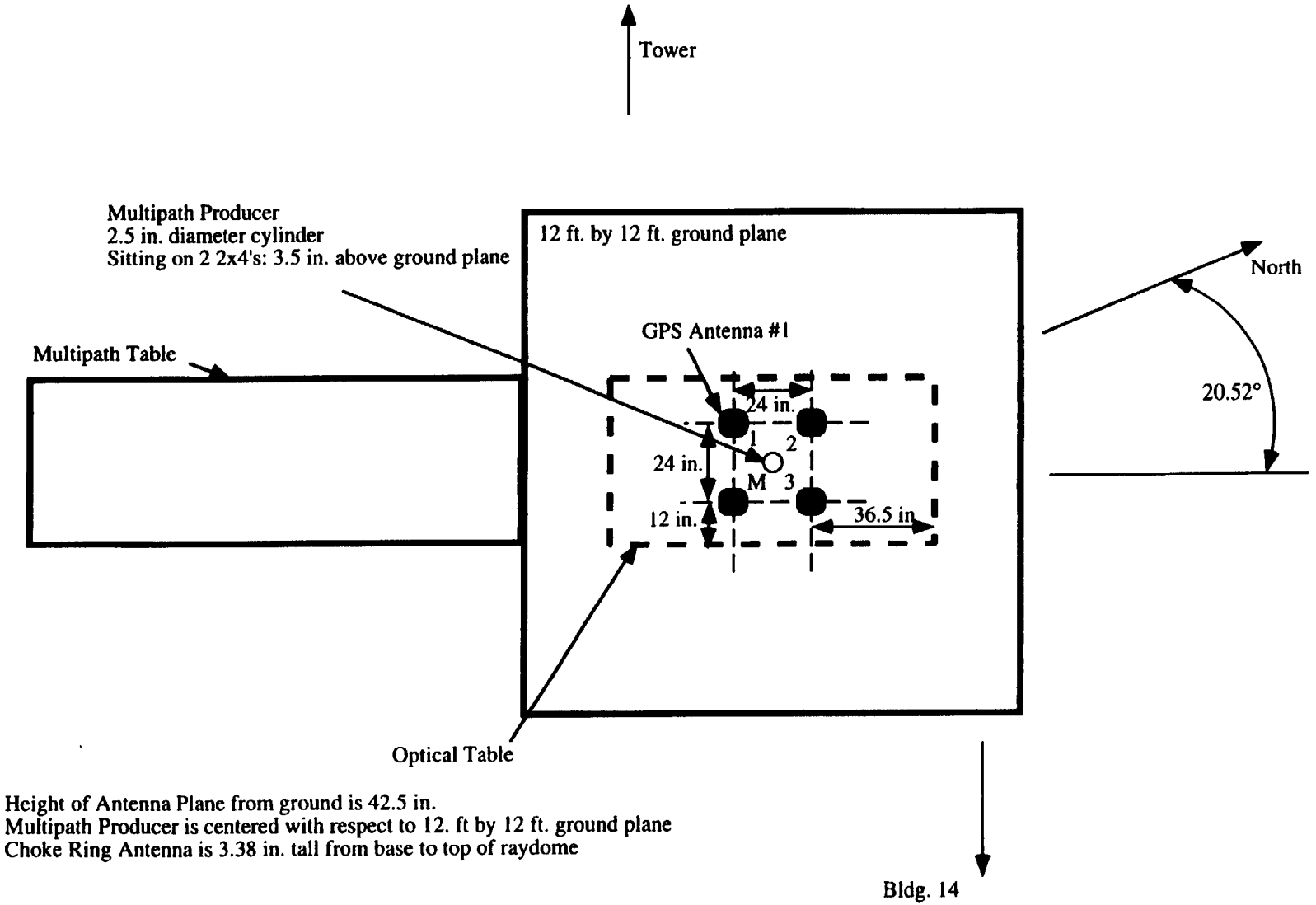

Height of Antenna Plane from ground is 42.5 in.
Multipath Producer is centered with respect to 12. ft by 12 ft. ground plane
Choke Ring Antenna is 3.38 in. tall from base to top of raydome

Multipath Test Setup on Bldg. 14 Antenna Range

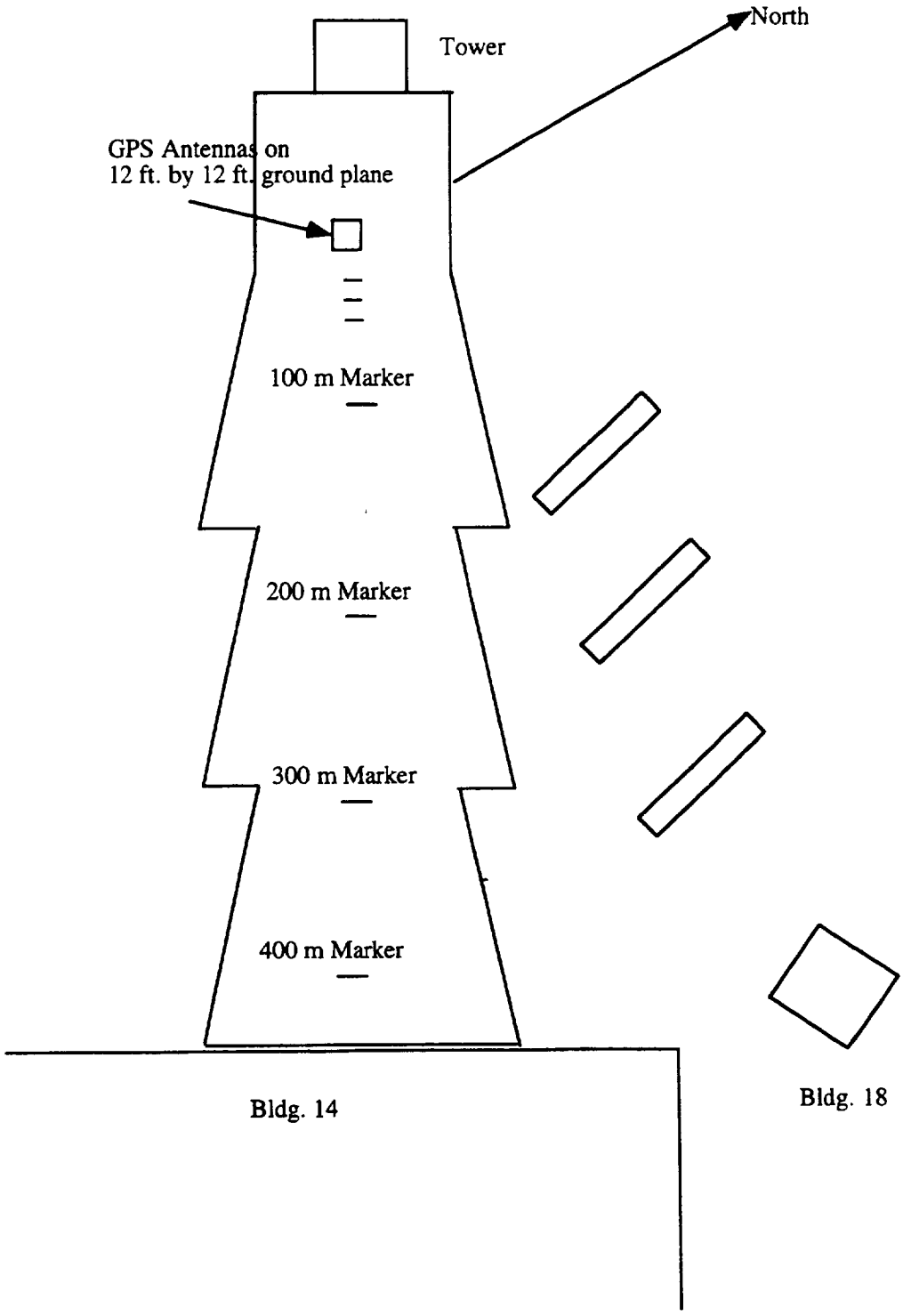

Appendix B - Information Needed to Calculate Reference Attitude

Table B-1 - Theodolite Readings to the North Star

Time of Sighting in UTC	Azimuth and Elevation Reading	
0:49:04	azimuth:	-20.42.10
	elevation:	30.10.26
0:54:45	azimuth:	-20:43:41
	elevation:	30:09:54
1:00:30	azimuth:	-20:44:57
	elevation:	30:09:03
1:04:15	azimuth:	-20:45:16
	elevation:	30:08:38
1:10:23	azimuth:	-20:46:13
	elevation:	30:07:37
1:17:30	azimuth:	-20:47:07
	elevation:	30:06:18

Building 14 Antenna Range Survey Marker Information

X = 493380.489 m
Y = -5530591.414 m
Z = 3127869.265 m

Lat 29:33:29.95046°
Lon 95:05:52.16901°

Ellipsoidal Alt -20.635 m
MSL Elevation 4.465 m

Appendix C -Recorded Weather Information for Each Day of Testing

Date day/month/ year	Time	Temp (°F)	Relative Humidity %	Pressure (in.)	Observations	PRN: Time - Time (UTC); status
09/02/95						
09/02/95	21:00	58.8	97.3	30.02	drizzle	17: 0820-0920; unusable
10/02/95	13:52	67.2	99.7	29.85	cloudy	
10/02/95	22:42	74.7	68.0	29.69	partly sunny	
13/02/95	14:23	45.0	73.5	30.11	Lt. rain	
14/02/95	14:34	53.6	101.7	30.01	fog	12: 2209-2325; unusable
14/02/95	22:25		101.6	29.87	fog	
15/02/95	14:06	66.9	101.1	29.81	fog	12:1901-1914;unusable
15/02/95	22:32	70.3	93.5	29.77	Lt. rain	
16/02/95	15:08	57.5	96.9	29.94	Cloudy	06:0348-0923; maintenance
16/02/95	22:43	63.1	79.4	29.98	Cloudy, Lt. rain	
17/02/95	14:00	49.4	90.9	30.25	Cloudy, rain	
17/02/95	22:54	56.8	65.3	30.22	Partly sunny	
18/02/95	17:36	61.2	40.6		Sunny	25:1505-1508;unusable
18/02/95						
19/02/95						12:0224-0238; unusable
19/02/95						
20/02/95						28:0915-1144; unusable
20/02/95						
21/02/95	15:22	65.1	34.4	30.24	Sunny	
21/02/95	22:47	73.8	25.5	30.16	Sunny	
22/02/95	14:20	58.9	73.2	30.16	Sunny	
22/02/95						
23/02/95	13:39	63.4	92.9	30.03	Partly cloudy	
23/02/95						
24/02/95	14:32	62.9	100.0	30.23	Cloudy, rain possible	
24/02/95	22:07	70.4	43.3	30.24	Sunny	
25/02/95						
25/02/95						
26/02/95						
26/02/95						
27/02/95	14:09	69.4	90.2	29.97	Partly cloudy	
27/02/95	22:39	71.8	81.3	29.88	Cloudy	
28/02/95	14:00	62.4	101.0	29.92	Lt. Rain	22:2241-2355; maintenance
28/02/95	22:46	62.6	84.9	29.94	CLOUDY!	
01/03/95	13:57	54.1	75.9	30.18	Cloudy	
01/03/95	22:00	56.3	70.4	30.21	Cloudy	
02/03/95	13:36	46.8	74.9	30.24	Cloudy	
02/03/95	22:26	48.3	81.8	30.19	Cloudy	

Date day/month/ year	Time	Temp (°F)	Relative Humidity %	Pressure (in.)	Observations	PRN: Time - Time (UTC); status
03/03/95	13:34	43.7	93.4	30.23	Cloudy	
03/03/95	22:42	48.5	81.9	30.17	Cloudy	
04/03/95						
04/03/95						
05/03/95						
05/03/95						
06/03/95	13:28	67.2	100.0	29.85	Foggy	
06/03/95	23:00	71.4	75.6	29.72	Cloudy	
07/03/95	14:57	60.1	94.5	29.81	Rain	28:begin at 0431; unusable
07/03/95	23:06	48.5	57.2	29.96	Partly sunny	
08/03/95	14:20	38.2	55.7	30.36	SUNNY!!!	28:ended at 0241; unusable
08/03/95					SUNNY!!!	
09/03/95	13:26	44.4	54.9	30.43	SUNNY!!!	
09/03/95	23:26	56.0	31.3	30.34	Overcast	
10/03/95	13:36	49.7	73.9	30.33	Overcast	
10/03/95						
11/03/95						
11/03/95						
12/03/95						
12/03/95						
13/03/95	14:32	59.7	94.0	29.95	RAIN	
13/03/95						
14/03/95	14:04	57.2	100.0	29.99	Fog	
14/03/95	22:32	69.4	55.7	29.88	Clouds in	
15/03/95	13:52	57.6	90.8	29.94	Overcast	
15/03/95	22:36	64.7	64.9	29.86	Partly sunny	
16/03/95	16:30	60.1	86.5	29.96	Cloudy	
16/03/95	22:45	67.2	54.9	29.92	Partly sunny	
17/03/95	14:06	62.1	88.5	30.05	SUNNY!	32:begin at 1636; unusable
17/03/95						
20/03/95	14:16	70.0	79.9	29.86	SUNNY	
20/03/95	22:12	77.6	58.7	29.79	Sunny	
21/03/95	16:00	71.2	82.8	29.92	Sunny	
21/03/95	22:52	79.5	51.3	29.83	SUNNY!	
22/03/95	13:52	69.2	88.2	29.79	SUNNY!	
22/03/95	22:44	78.7	60.4	29.74	SUNNY!	
23/03/95						
23/03/95						
24/03/95	13:53	71.6	87.7	29.78	Overcast	32:ended at 2012; unusable
24/03/95	Shut down					

REPORT DOCUMENTATION PAGE

Form Approved
OMB No. 0704-0188

1. AGENCY USE ONLY (Leave Blank)	2. REPORT DATE	3. REPORT TYPE AND DATES COVERED
	March 1996	NASA Technical Memorandum

4. TITLE AND SUBTITLE

Evaluation of Two Computational Techniques of Calculating Multipath Using Global Positioning System (GPS) Carrier Phase Measurements

5. FUNDING NUMBERS

6. AUTHOR(S)

Susan F. Gomez; Laura Hood; Robert J. Panneton; Penny E. Saunders; Antha Adkins*; Dr. Shian U. Hwu*; Ba P. Lu*

7. PERFORMING ORGANIZATION NAME(S) AND ADDRESS(ES)

Lyndon B. Johnson Space Center
Aeroscience and Flight Mechanics Division
Houston, Texas 77058

8. PERFORMING ORGANIZATION REPORT NUMBERS

S-804

9. SPONSORING/MONITORING AGENCY NAME(S) AND ADDRESS(ES)

National Aeronautics and Space Administration
Washington, D. C. 20546-0001

10. SPONSORING/MONITORING AGENCY REPORT NUMBER

TM-104816

11. SUPPLEMENTARY NOTES

*Lockheed Martin Engineering and Science Services, Houston, Texas

12a. DISTRIBUTION/AVAILABILITY STATEMENT

Unclassified/Unlimited
Available from the NASA Center for AeroSpace Information (CASI)
Attn: Accessioning Department
800 Elkridge Landing Road
Linthicum Heights, MD 21090-2934 Subject Category:

12b. DISTRIBUTION CODE

13. ABSTRACT *(Maximum 200 words)*

Two computational techniques are used to calculate differential phase errors on Global Positioning System (GPS) carrier wave phase measurements due to certain multipath-producing objects. The two computational techniques are a rigorous computation electromagnetics technique called Geometric Theory of Diffraction (GTD) and the other is a simple ray tracing method. The GTD technique has been used successfully to predict microwave propagation characteristics by taking into account the dominant multipath components due to reflections and diffractions from scattering structures. The ray tracing technique only solves for reflected signals. The results from the two techniques are compared to GPS differential carrier phase measurements taken on the ground using a GPS receiver in the presence of typical International Space Station (ISS) interference structures. The calculations produced using the GTD code compared to the measured results better than the ray tracing technique. The agreement was good, demonstrating that the phase errors due to multipath can be modeled and characterized using the GTD technique and characterized to a lesser fidelity using the DECAT technique. However, some discrepancies were observed. Most of the discrepancies occurred at lower elevations and were either due to phase center deviations of the antenna, the background multipath environment, or the receiver itself. Selected measured and predicted differential carrier phase error results are presented and compared. Results indicate that reflections and diffractions caused by the multipath producers, located near the GPS antennas, can produce phase shifts of greater than 10 mm, and as high as 95 mm. It should be noted that the field test configuration was meant to simulate typical ISS structures, but the two environments are not identical. The GTD and DECAT techniques have been used to calculate phase errors due to multipath o the ISS configuration to quantify the expected attitude determination errors.

14. SUBJECT TERMS

Global Positioning System, multipath, transmission, differential interferometry, diffraction, Geometrical Theory of Diffraction, carrier waves, signal reflection, ray tracing

15. NUMBER OF PAGES

130

16. PRICE CODE

17. SECURITY CLASSIFICATION OF REPORT	18. SECURITY CLASSIFICATION OF THIS PAGE	19. SECURITY CLASSIFICATION OF ABSTRACT	20. LIMITATION OF ABSTRACT
Unclassified	Unclassified	Unclassified	Unlimited